Technische Universität München

TUM School of Engineering and Design

A Finite-Element Transonic Potential Flow Solver with an Embedded Wake Approach for Aircraft Conceptual Design

Iñigo Pablo López Canalejo

Vollständiger Abdruck der von der TUM School of Engineering and Design zur Erlangung des akademischen Grades eines

Doktors der Ingenieurwissenschaften

genehmigten Dissertation.

Vorsitzender:

Priv.-Doz. Dr.-Ing. habil. Stefan Kollmannsberger

Prüfer der Dissertation:

1. Prof. Dr.-Ing. Kai-Uwe Bletzinger
2. Prof. Riccardo Rossi, Ph.D.
3. apl. Prof. Dr.-Ing. Christian W.M. Breitsamter

Die Dissertation wurde am 15.11.2021 bei der Technischen Universität München eingereicht und durch die TUM School of Engineering and Design am 14.04.2022 angenommen.

Schriftenreihe des Lehrstuhls für Statik TU München

Band 51

Iñigo Pablo López Canalejo

A Finite-Element Transonic Potential Flow Solver with an Embedded Wake Approach for Aircraft Conceptual Design

München 2021

Abstract

This dissertation presents a novel embedded wake approach for the solution of the full-potential equation using finite elements. The ultimate goal of this embedded approach is to effectively perform aircraft aeroelastic optimization at the early stages of aircraft design, taking transonic effects into account. Currently, this is not possible using standard full-potential solvers because they require modeling a gap in the mesh across the wake to support a jump in the potential. This additional requirement on the mesh generation process hinders the effective use of such solvers for aircraft aeroelastic optimization, where the wake's position may change due to the structural deformation and the geometry's evolutionary steps. Therefore, this dissertation aims to determine how to avoid modeling the wake in the mesh. To this end, a novel embedded wake approach for potential transonic solvers is proposed.

In the proposed approach, upper and lower wake surfaces are disconnected by enriching the space of the finite elements cut by the wake with additional degrees of freedom. Subsequently, the additional equations that stem from the discretization are used to apply the wake boundary conditions. Since the wake cuts the finite elements arbitrarily, the system of equations can potentially be ill-conditioned due to the so-called small-cut element problem. To ensure robustness and avoid large condition numbers, a full-integration technique is presented. Furthermore, shock waves are captured using an artificial compressibility method, which is used to stabilize the problem in supersonic flow regions preventing the Jacobian from becoming singular.

The proposed embedded wake approach is validated and verified on unstructured meshes in two and three dimensions. These verification studies show that the results accurately match the reference data. According to these results, an extra mesh refinement to capture the wake is not required, making the method's computational cost comparable to other full-potential solvers. Moreover, the wake's surface can be generated automatically by shedding it from the trailing edge in the freestream direction. This implicit representation of the wake within the domain saves modeling time and allows efficient aeroelastic optimization in practical applications. The solver is implemented in KRATOS Multiphysics and is available under a BSD license.

Zusammenfassung

In dieser Dissertation wird ein neuartiger Ansatz zur Lösung der vollen Potentialgleichung mit Finiten Elementen vorgestellt, in den die Wirbelschleppe im Netz eingebettet ist. Das Endziel dieses eingebetteten Ansatzes ist es, die aeroelastische Optimierung von Flugzeugen in den frühen Phasen des Flugzeugentwurfs unter Berücksichtigung der transsonischen Effekte effektiv durchzuführen. Derzeit ist dies mit Standard-Vollpotentiallöser nicht möglich, da diese die Modellierung eines Spalts im Netz erfordern, um einen Potentialsprung quer zur Wirbelschleppe zu ermöglichen. Diese zusätzliche Anforderung an den Netzgenerierungsprozess behindert den effektiven Einsatz solcher Löser für aeroelastische Optimierung, bei der sich die Position der Wirbelschleppe aufgrund der strukturellen Verformung und der Evolutionsschritte der Geometrie ändern kann. In dieser Dissertation wird daher untersucht, wie sich die Modellierung der Wirbelschleppe im Netz vermeiden lässt. Zu diesem Zweck wird ein neuartiger Ansatz für eingebettete Wirbelschleppen für transsonische Potentiallöser entwickelt.

Bei dem hier vorgestellen Ansatz werden obere und untere Wirbelschleppenflächen voneinander getrennt, indem der Ansatzraum der durch die Wirbelschleppe geschnittenen Finiten Elemente mit zusätzlichen Freiheitsgraden angereichert wird. Anschließend werden die zusätzlichen Gleichungen, die sich aus der Diskretisierung ergeben, zur Aufbringung der Wirbelschleppe-Randbedingungen verwendet. Da die Wirbelschleppe die Finiten Elemente willkürlich schneidet, kann das Gleichungssystem aufgrund des so genannten Klein-Geschnitten-Element-Problems schlecht konditioniert sein. Um Robustheit zu gewährleisten und große Konditionszahlen zu vermeiden, wird eine Vollintegrationstechnik vorgestellt. Darüber hinaus werden Stoßwellen mit einer künstlichen Kompressibilitätsmethode erfasst, die zur Stabilisierung des Problems in Überschallströmungsgebieten verwendet wird, um zu verhindern, dass die Jacobi-Matrix singulär wird.

Der entwickelte Ansatz für eingebettete Wirbelschleppen wird auf unstrukturierten Netzen in zwei und drei Dimensionen validiert und verifiziert. Diese Verifizierungsstudien zeigen, dass die Ergebnisse genau mit den Referenzdaten übereinstimmen. Entsprechend dieser Ergebnisse ist eine zusätzliche Netzverfeinerung zur Erfassung der Wirbelschleppe nicht erforderlich, sodass der Rechenaufwand der Methode mit dem anderer Vollpotentiallöser vergleichbar ist. Außerdem kann die Wirbelschleppe automatisch erzeugt werden, indem sie von der Hinterkante in Richtung der Freistromgeschwindigkeit abgeworfen wird. Diese implizite Darstellung der Wirbelschleppe innerhalb des Gebiets spart Modellierungszeit und ermöglicht eine effiziente aeroelastische Optimierung in praktischen Anwendungen. Der Löser ist in KRATOS Multiphysics implementiert und ist unter einer BSD-Lizenz verfügbar.

Acknowledgments

This thesis would not have been possible without the support of my mentors and my colleagues. First and foremost, I would like to thank my advisor Professor Kai-Uwe Bletzinger for giving me the opportunity to do research at his Chair and for providing me with all the necessary support to carry out this investigation. I also wish to thank Professor Roland Wüchner for his guidance and for putting me in touch with our industrial partners. In addition, I would like to thank Professor Riccardo Rossi and Professor Christian Breitsamter for reviewing this dissertation and Dr. Stefan Kollmannsberger for charing the examiner committee. Special thanks to Professor Riccardo Rossi for introducing me to the Kratos team and for his original ideas. His numerical intuition and programming skills provided me with the tools I needed to develop this method.

I would also like to gratefully acknowledge the work and support of my colleagues at the Chair, at CIMNE, at the Chair of Aerodynamics, and at Airbus. This thesis is the result of our fruitful collaboration. I would like to especially thank: Marc Nuñez for our technical discussions and for reviewing this work, Dr. Julie Piquee for sharing invaluable knowledge in aerodynamics, Philipp Bucher for reviewing and helping improve the implementation, Dr. Altug Emiroglu for sharing his ideas and compilation skills, Dr. Andreas Apostolatos for our lengthy discussions, and Máté Péntek for reviewing this thesis. I also want to thank Dr. Michael Andre, Dr. Jordi Cotela, Dr. Rubén Zorrilla, Aditya Ghantasala, and Suneth Warnakulasuriya for mentoring me during this period. I am very grateful for Tobias Teschemacher's contagious good spirit and positive attitude.

This work started during my time at Airbus Defence and Space. I would like to thank my supervisors Dr. Fernass Daoud and Stepan Rechtik, for helping me shape the topic of this thesis. In addition, I am very grateful to my colleagues: Alessandro Gastaldi, Daniel Nussbächer, Dr. Sebastian Deinert, Dr. Alexander Hormann, Ögmundur Petersson, and Reinhold Maier, for their insights in the practical aspects of multidisciplinary aircraft optimization.

I thank my family for their support and encouragement. I am very grateful for the education and the opportunities my parents have given to me. Thanks to them I could come to Germany to complete my studies.

Finally, I would like to thank Nina for her selfless support. She has always been there for me during the last six years, listening to my problems and providing invaluable advice.

Iñigo Pablo López Canalejo
Technische Universität München
November 9, 2021

Contents

Abstract iii

Zusammenfassung iv

Acknowledgments v

List of Symbols xi

1 Introduction 1
- 1.1 Motivation 1
- 1.2 Developments in numerical potential transonic flow solvers 4
- 1.3 Outline 8

2 Fundamentals of Potential Flow 11
- 2.1 Navier-Stokes equations 11
  - 2.1.1 Initial and boundary conditions 12
  - 2.1.2 Non-dimensionalization 13
- 2.2 High Reynolds number flow 16
  - 2.2.1 Isentropic flow 17
  - 2.2.2 Steady compressible Bernoulli equation 18
  - 2.2.3 Irrotational flow 18
- 2.3 Full-potential equation 19
  - 2.3.1 Classification of the full-potential equation 19
  - 2.3.2 Boundary conditions 21
- 2.4 Aerodynamic loads 24
  - 2.4.1 Near-field analysis 24
  - 2.4.2 Far-field analysis 25
  - 2.4.3 Wake potential jump analysis 26

3 An Embedded Wake Approach for Potential Transonic Solvers **29**
3.1 Strong form, domain, and boundary conditions 29
3.2 Finite element discretization 31
3.3 Artificial compressibility 33
3.3.1 The switching function 34
3.4 Limit velocity in isentropic flow 35
3.5 Embedded wake approach 37
3.5.1 Wake boundary conditions in two dimensions . . . 39
3.5.2 Wake boundary conditions in three dimensions . . 39
3.5.3 Treatment of the nodes lying on the wake 41
3.5.4 Treatment of the trailing edge nodes 41
3.5.5 Treatment of small-cut elements 42
3.6 Implementation in KRATOS Multi-Physics 43
3.6.1 Kratos structure 44
3.6.2 Potential flow application 45

4 Validation, Verification and Numerical Studies **47**
4.1 Incompressible flow around NACA 0012 airfoil 48
4.1.1 Mesh refinement study of the reference solution . . 49
4.1.2 Mesh refinement study 50
4.1.3 Pressure coefficient distribution verification 55
4.1.4 Domain size study 55
4.1.5 Validation with wind tunnel data 59
4.2 Verification of the compressible subsonic and transonic elemental sensitivities 62
4.3 Compressible subsonic flow around NACA 0012 airfoil 63
4.3.1 Mesh refinement study 63
4.3.2 Pressure coefficient distribution verification 64
4.3.3 Newton Raphson's method convergence 69
4.4 Transonic flow around NACA 0012 airfoil 72
4.4.1 Mesh refinement study 72
4.4.2 Pressure coefficient distribution verification 75
4.4.3 Newton Raphson's method convergence 77
4.5 Transonic flow around Korn supercritical airfoil 77
4.5.1 Pressure coefficient distribution verification 78
4.6 Drag divergence study 80
4.6.1 Critical Mach number verification 83
4.6.2 Multi-fidelity analysis study 84
4.7 3D rectangular wing with NACA 0012 airfoil section in incompressible flow 87
4.7.1 Pressure coefficient distribution verification 88
4.7.2 Potential jump distribution verification 88
4.8 3D ONERA M6 wing transonic validation case 90
4.8.1 Wing's geometry and mesh 90
4.8.2 Pressure coefficient validation and verification . . 93

4.8.3 Aerodynamic loads verification 98
4.8.4 Performance comparison 99
4.8.5 Wake potential jump condition and wingtip vortex 100
4.9 NASA Common Research Model transonic validation and verification case 102
4.9.1 Model description 102
4.9.2 Mesh refinement study 106
4.9.3 Pressure coefficient validation and verification . . 108
4.9.4 Aerodynamic loads validation and verification . . . 112
4.9.5 Potential jump across embedded wakes 113
4.9.6 Contour plots and wingtip vortices 116
4.9.7 Nacelle-pylon effect 116

5 Conclusions **125**
5.1 Summary 125
5.2 Outlook 134

A Helmholtz Vorticity Transport Equation **137**

B Transonic Full-potential Solver Sensitivities **139**
B.1 Residual 139
B.2 Upwind density 139
B.3 Density 140
B.4 Upwinding factor 141
B.5 Mach number squared 141
B.6 Velocity squared 141
B.7 Velocity vector 142

C Verification of the Embedded Wake Approach for Incompressible Flow **143**

Bibliography **163**

List of Symbols

Fluid magnitudes and other quantities

$\boldsymbol{u}, u$	Velocity vector and magnitude
ϕ	Velocity potential
$\Delta\phi$	Potential jump across the wake
α	Angle of attack
ρ	Density
p	Pressure
T	Temperature
a	Local speed of sound
$\boldsymbol{\omega}$	Vorticity
e	Specific internal energy
s	Specific entropy
h	Specific enthalpy
$\bar{\bar{\boldsymbol{\tau}}}$	Viscous stress tensor
μ	Dynamic viscosity
k	Thermal conductivity
Q	Thermal heating rate due to radiation or combustion
$\boldsymbol{f}$	Body forces
g	Gravity
λ	Molecular mean free path
$\boldsymbol{x}$	Position vector (x, y, z)

t	Time
f	Frequency
q	Mass flow

Dimensionless numbers

M	Mach number
Re	Reynolds number
St	Strouhal number
Fr	Froude number
Pr	Prandtl number
Kn	Knudsen number

Geometric parameters

c	Airfoil chord (characteristic length)
$\overline{c}$	Mean aerodynamic chord
t	Airfoil thickness
b	Wingspan
η	Dimensionless spanwise location ($= y/b$)
A_{ref}	Reference wing area
Λ	Aspect ratio
λ	Taper ratio
φ_{25}	Sweep angle
$\mathrm{d}S$	Differential area

Air constants for aerodynamic flows

γ	Ratio of specific heats ($= 1.4$)
c_p	Specific heat capacity at constant pressure ($= 1.005$ kJ/kgK)
c_v	Specific heat capacity at constant volume ($= 0.718$ kJ/kgK)
R_g	Specific gas constant ($= 287$ J/kgK)

Subscripts and superscripts

$(\,)_0$	Initial conditions
$(\,)_o$	Stagnation (total) quantity
$(\,)_\infty$	Far field (or freestream) conditions

$(\,)_{\mathrm{u}}$	Upper wake
$(\,)_{\mathrm{l}}$	Lower wake
$(\,)_D$	Dirichlet
$(\,)_N$	Neumann
$(\,)_W$	Wake
$(\,)_{\mathrm{up}}$	Upstream's element quantity
$(\,)^*$	Critical value
$(\,)'$	Dimensionless magnitude

Aerodynamic loads and coefficients

$\mathbf{F}$	Force vector
L	Lift
Y	Sideforce
D	Drag
C_L	Lift coefficient
C_D	Drag coefficient
C_{Dpr}	Pressure drag coefficient
C_{Dsf}	Skin-friction drag coefficient
C_m	Pitching moment coefficient
c_l	2D airfoil lift coefficient
c_d	2D airfoil drag coefficient
c_m	2D airfoil pitching moment coefficient
δ_{c_l}	2D airfoil lift coefficient relative error
δ_{c_m}	2D airfoil pitching moment coefficient relative error
C_p	Pressure coefficient
$C_{p\mathrm{min}}$	Minimum pressure coefficient
$(C_{p\mathrm{min}})_{\mathrm{inc}}$	Minimum pressure coefficient in incompressible flow

Finite element method

N	Shape functions
R^i	Residual vector
J^{ij}	Jacobian matrix
Ω	Domain
Γ	Boundary
h	Minimum element size

L	Domain size
k	Newton Raphson iteration
$\hat{\boldsymbol{n}}$	Normal unit vector
ϕ_{u}^{i}	Upper wake elements velocity potential degrees of freedom
ϕ_{l}^{i}	Lower wake elements velocity potential degrees of freedom
ϕ_{aux}^{i}	Auxiliary velocity potential degrees of freedom
Π	Wake boundary conditions residual energy functional

Artificial compressibility method

$\tilde{\rho}$	Upwind density
μ_s	Switching function
μ	Upwinding factor
μ_{c}	User-defined upwinding factor constant
M_{crit}	User-defined critical Mach number

List of abbreviations

CFD	Computational Fluid Dynamics
FPE	Full-Potential Equation
FPS	Full-Potential Solver
FEM	Finite-Element Method
FVM	Finite-Volume Method
2D	Two Dimensions
3D	Three Dimensions
CAD	Computer-Aided Design
STL	Standard Triangle Language or Standard Tessellation Language
OpenMP	Open Multi-Processing
WTD	Wind Tunnel Data
CPU	Central Processing Unit
RANS	Reynolds-Averaged Navier-Stokes
CRM	NASA Common Research Model
DPW	Drag Prediction Workshop
AIAA	American Institute of Aeronautics and Astronautics
NTF	National Transonic Facility

Chapter 1

Introduction

1.1 Motivation

Despite the increase of computational power and the advances in high-fidelity methods in the last decades, potential linear solvers, typically panel or vortex lattice solvers, are still widely used in the industry for aircraft aeroelastic optimization at the early stages of design. In these design stages, many configurations have to be explored, ensuring the structural integrity for a large number of flight conditions. Therefore, the required number of fluid evaluations scales with the number of configurations, the number of optimization steps, and the number of aeroelastic iterations needed in each optimization step. This yields a number that ranges from a couple of hundreds to a couple of thousands of fluid evaluations. Fast solvers are thus still required for practical applications [1]. However, commercial aircraft are typically designed to fly at transonic speeds, and potential linear solvers fail to capture the nonlinear transonic flow behavior. Full-potential solvers offer an appealing trade-off, allowing to obtain fast solutions while enlarging the range of application to capture nonlinear transonic effects.

Nevertheless, standard full-potential solvers require modeling a gap in the mesh to support a jump in the potential across the wake. This requires adapting the model to the wake's topology imposing additional requirements on the mesh-generation process. The wake model also hinders the effective use of such solvers for aeroelastic optimization, where the wake's position may change due to the structural response and the geometry's evolutionary steps.

The wake-fitted mesh approach is illustrated in Figure 1.1, which shows a two-dimensional finite element mesh behind an airfoil. The wake is the straight-line shed from the trailing edge in the direction of the freestream velocity. Finite elements are not connected across the wake to support a jump in the potential.

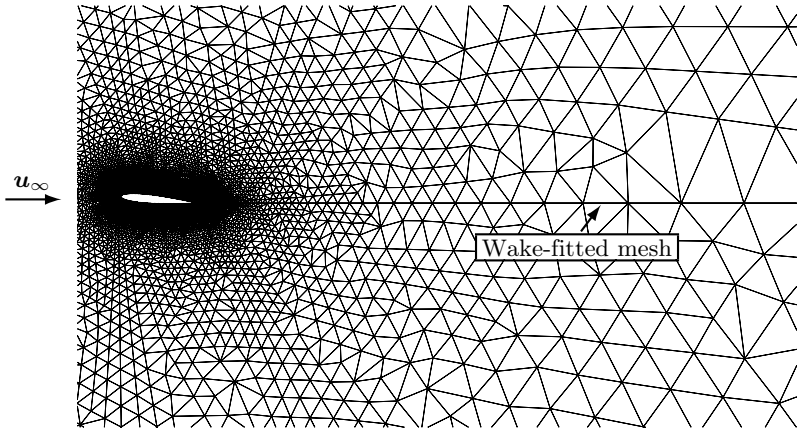

Figure 1.1: Standard full-potential solvers using unstructured meshes require modeling the wake as a gap in the mesh to support a jump in the potential.

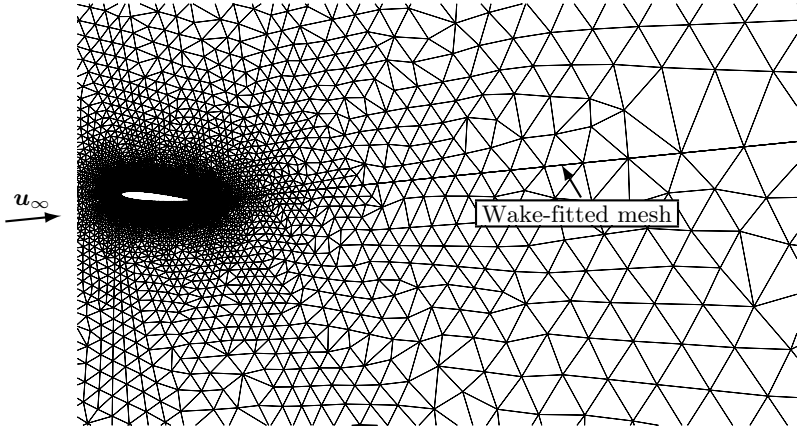

Figure 1.2: Changing the angle of attack involves moving the mesh.

Elements containing a node at the wake line are thus only attached to one side of the wake. Hence, wake nodes are present twice. Figure 1.2 shows that changing the angle of attack modifies the wake's position, which involves moving the mesh. Moving the wake can be performed in two dimensions (2D), but it becomes rather cumbersome and sometimes even impossible in three dimensions (3D) without regenerating the mesh. To illustrate this, Figure 1.3 shows a 3D aircraft model within a prismatic domain, and the trailing wakes for two different angles of attack. The zoomed-in area shows that the two wakes cut the fuselage at two different positions. Therefore, two different models and meshes are required to define the different cuts in the fuselage in this case.

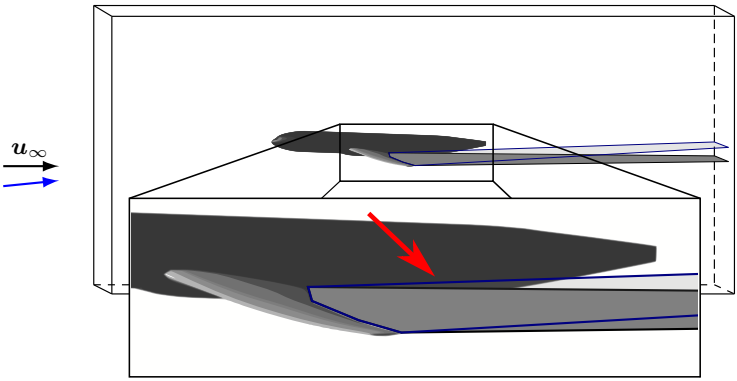

Figure 1.3: The new wake (marked in blue) defines a different cut in the fuselage compared to the original wake (marked in black). This requires regenerating the model.

In this work, an embedded wake approach using the finite-element method (FEM) on unstructured meshes is proposed to enable the effective use of full-potential solvers in the context of aircraft aeroelastic optimization. The advantage of using an embedded wake approach is twofold. On the one hand, this approach avoids having to explicitly create the wake surface in the computer-aided design (CAD) model and to fit the mesh to the wake. This greatly simplifies and speeds up the preprocessing stage. On the other hand, embedding the wake allows automatically capturing its position in each aeroelastic iteration without moving or regenerating the mesh. The proposed embedded wake approach is illustrated in Figure 1.4, where the wake's position has been added and is indicated in a dashed blue line for visualization purposes. Note that the wake is no longer explicitly modeled within the mesh.

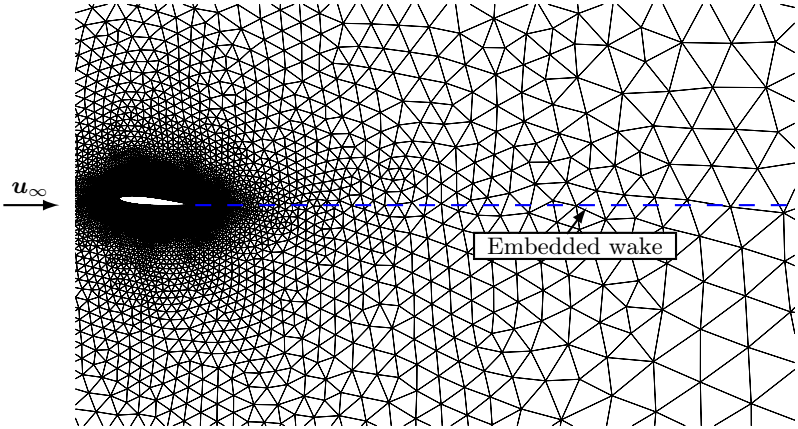

Figure 1.4: Proposed embedded wake approach.

1.2 Developments in numerical potential transonic flow solvers

This section provides a brief review of the development of full-potential methods. A thorough survey was published by Stein [2, 3] and by Holst [4]. Mason has also published a lecture giving an overview on this matter [5].

The solution of transonic flow problems is very challenging due to the mixed elliptic hyperbolic nature of the underlying governing equation and the appearance of shock waves within the domain. A breakthrough in the development of numerical methods for the solution of potential transonic flows was made by Murman and Cole in 1970 [6]. Murman and Cole developed a mixed finite difference method to solve the nonlinear transonic small disturbance potential equation in 2D. Their method used different formulas in the elliptic and hyperbolic regions to account for the different local domains of dependence and capture shock waves during the numerical solution naturally.

Jameson made the following significant contribution in 1974, who was at the time working for Grumman. Jameson attended Murman's presentation of his method at the AIAA Aerospace Sciences Meeting in New York City in January of 1970 and extended it to solve the full-potential equation (FPE) in three dimensions. His method added an auxiliary Cartesian coordinate system locally aligned with the flow to achieve the required rotation of the upwind differencing at any point [7]. This full-potential solver (FPS) was implemented in FLO22. In this thesis, a later version of this solver, namely FLO36, is used to verify the proposed approach.

In order to treat arbitrary complex geometries, Jameson and Caughey published a finite volume approach in 1977 using an artificial viscosity in the supersonic flow regions [8]. This artificial viscosity method was then simplified and reformulated by Hafez, South, and Murman in 1978 and applied to the full-potential equation in conservation form [9]. The new method modified the density and was thus labeled the artificial compressibility method. Still, the density modification was equivalent to an artificial viscosity. About the same time, Eberle developed a FEM for the solution of transonic flow past airfoils, which also used an artificial viscosity method [10].

The superposition principle cannot be applied to solve the FPE because it is nonlinear. Therefore, singularity methods such as Vortex Lattice or Panel methods cannot be used to solve the FPE. Instead, a grid method is required. As any other computational fluid dynamics (CFD) technique, the transonic full potential methods can be categorized into two groups according to the flow domain discretization approach:

- Structured grids
- Unstructured grids

On the one hand, in structured grids, nodes have the same number of elements around them. On the other hand, unstructured grids are characterized by having irregular connectivity. Figure 1.5 shows examples of structured and unstructured grids both for triangular and quadrilateral meshes in 2D. Moreover, structured quadrilateral grids can be Cartesian or curvilinear depending on whether the grid lines are always parallel to the coordinate axes or not. Although historically structured quadrilateral grids are preferred, unstructured grids have become more common due to their ability to handle complex geometries. The discretization approaches can be further categorized depending on how the body is captured in the grid:

- Body-fitted grid
- Embedded grid
- Hybrid grid
- Chimera grids (also called overset grids)

The body-fitted grid explicitly represents the body's boundaries, whereas, in embedded grids, the boundaries are implicitly captured. Traditionally body-fitted grids were used, but recently the use of embedded grids is becoming more popular because they simplify the meshing process even further and allow for moving boundaries during the simulation. Hybrid grids combine both former approaches. Another alternative are chimera grids in which separate body-fitted meshes are generated about selected features of a complex geometry. A

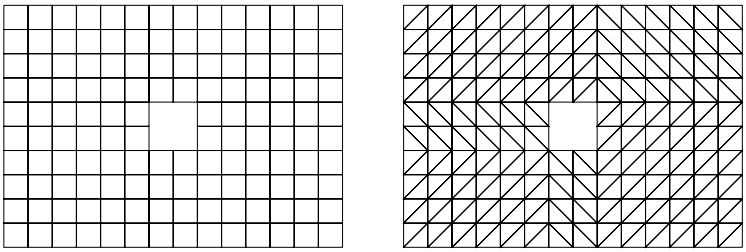

(a) Structured grids.

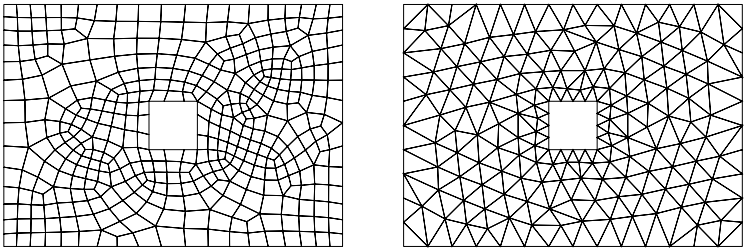

(b) Unstructured grids.

Figure 1.5: Examples of body-fitted grids.

background (typically structured) mesh is then employed to connect the near field meshes to the freestream using an interpolation scheme.

The most popular grid approaches to solve the flow about complex geometries using transonic full-potential methods are: chimera grids, patched zonal grids, unstructured Cartesian grids, and unstructured body-fitted grids. While for the chimera and patched zonal grid approaches, the solver is typically a finite-difference or finite-volume method, for unstructured grids, it is usually a finite-volume or finite-element method.

Examples of early chimera grid approaches used to solve the FPE for transonic flow are presented in Atta [11] for 2D airfoils, Le [12] for wing/body combinations and Atta and Vadyak [13] for wing/nacelle geometries. Further developments were presented by Holst [14–16] for three-dimensional wing/-body/nacelle configurations, and by Bangalore et al. [17] and by Moulton et al. [18] for hybrid rotorcraft applications.

To mesh complex geometries using structured body-fitted grids, the domain is typically divided into different zones or blocks. These blocks are meshed

separately and joined together at the interface. Developments for solving the FPE using these so-called zonal or block structured grid approaches have been published by Ecer and Spyropoulos [19] for wing/body configurations, by Epstein et al. [20] for full aircraft applications, by Sankar et al. [21] for three-dimensional Navier-Stokes/Full-Potential coupled analysis, by Berkman et al. [22] for rotor flows, and by Nishida and Drela [23]. The latter coupled a FPS with a boundary layer solver using finite elements and used it to analyze the flow about the wing of a Boeing 747.

Cartesian unstructured grid techniques employ meshes with quadrilateral or cubic volumes/elements that are then refined in regions of high solution gradients. The intersection of the mesh with the body's surface requires additional handling by the method (which typically is of FEM type). The biggest drawback of the Cartesian unstructured grid approach is that extra refinement is needed in the case of solution gradients at 45° with respect to the mesh. The most famous and successful Cartesian unstructured grid approach is perhaps the one used in the TRANAIR code. TRANAIR uses a FEM discretization procedure. The method is rigorously described in Rubbert et al. [24], Young et al. [25], and Bieterman et al. [26]. Examples of the solution of complex aerodynamic applications using TRANAIR have been reported by Cenko and Piranian [27] to predict the flow field about the F-18E aircraft, by Ridlon et al. [28] for coupled aeroelastic analysis, by SenGupta et al. [29] for the unsteady aerodynamic and flutter characteristics analysis of an aeroelastic model in transonic flow, by Madson [30] to analyze the transonic flow about the F-16A with under-wing fuel tanks, by Goodsell et al. [31] to validate TRANAIR with experimental data using a generic fighter geometry, by Chen et al. [32] for engine/airframe integration applications, by Madson [33] for sonic boom predictions, and by Jou et al. [34] for aerodynamic design optimization.

Finally, the unstructured body-fitted grid approach typically uses triangles (in 2D) or tetrahedra (in 3D) to discretize the domain (see Figures 1.1, 1.2 and 1.4). A significant advantage of this unstructured approach compared to structured approaches is its flexibility to handle complex configurations relatively easily. With this approach, the volume mesh generation difficulties are simplified for complex geometries. Furthermore, since the mesh conforms with the body's boundary, the boundary conditions are accurately applied. The unstructured grid approach has been used in many full aircraft configuration applications, which is the reason why it is the selected approach in this work. Early examples of unstructured mesh FEM approaches using in full-potential flow solvers are presented in Ecer and Akay [35] and Glowinski et al. [36]. The artificial compressibility method employed by Eberle was also used by Deconinck and Hirsch [37, 38], and by Akay and Ecer [39]. Based on the work of Nishida and Drela, Eller presented in 2012 a high-order finite-element method for the solution of the FPE [40]. With his method, Eller successfully computed the flow about the DLR F4 wing/body configuration. However, in his conclusions, Eller states: "At the time of writing, there is limited support

for the automatic generation of unstructured meshes with embedded wake surfaces. Including embedded wakes is a necessary prerequisite for the effective use of the method presented here''.

Based on Eller's work and conclusions, the present work proposes an unstructured grid approach for the solution of the FPE for transonic flow using FEM in which the wake is implicitly represented in the mesh. The proposed method can be used to initialize the flow field and speed up the convergence of higher fidelity solvers.

1.3 Outline

This thesis is organized into five chapters. After the introduction presented in Chapter 1, Chapter 2 provides an overview of the assumptions that allow modeling flows using the FPE. The main purpose of this chapter is to show that high Reynolds numbers characterize typical aerodynamic flows. This allows simplifying the Navier-Stokes equations under the assumption that the body is streamlined and flying at small angles of attack with attached boundary layers. To this end, the first part of the chapter starts by introducing the Navier-Stokes equations and using dimensional analysis to compare the relative importance of their different terms. The second part of the chapter shows that without heat addition due to combustion, high Reynolds number flows can be assumed to be isentropic and irrotational. Thus, the velocity can be written in terms of a potential gradient. Finally, the chapter's last part introduces the FPE together with its mixed type nature and the necessary boundary conditions.

The proposed embedded wake approach is described in Chapter 3. The first two sections review the FPE strong form and the boundary conditions. Then, a standard Galerkin approach is used to discretize the equation, and an artificial compressibility method is presented to stabilize the problem in supersonic flow regions preventing the Jacobian from becoming singular and allowing to capture shock waves. Next, a remedy is described to avoid having ill-defined expressions in areas of high flow curvature. This problem is related to the limit velocity in isentropic flow.

Furthermore, the proposed embedded wake approach is presented in Section 3.5 and the method used to apply the wake boundary conditions is described. Using an embedded wake approach requires specific care, especially when dealing with small-cut elements that yield ill-conditioned systems. In this section, the cause leading to large condition numbers is analyzed, and the solution developed in this work is presented. Finally, the implementation in KRATOS Multiphysics is briefly described.

Chapter 4 presents the validation and verification of the proposed embedded wake approach together with some numerical studies. In total, five models have been investigated: the NACA 0012 airfoil in all flow regimes (incompressible, compressible subsonic, and compressible transonic), the Korn supercritical

airfoil in transonic flow, a rectangular wing in incompressible flow, and Onera M6 wing and NASA NASA Common Research Model (CRM) in transonic flow. To evaluate the proposed approach, lift, drag, pitching moment, and pressure coefficients are compared with reference data from other codes and wind tunnel tests. Finally, the main conclusions and outlook are summarized in Chapter 5.

Throughout the thesis, the following footnotes are used to reference the original publications and to mark literal transposition. [a] [b] [c] [d]

[a] The following chapter/section/paragraph is based on [41]. The main scientific research as well as the textual elaboration of the publication were performed by the author of this work.

[b] The following chapter/section/paragraph is based on [42]. The main scientific research as well as the textual elaboration of the publication were performed by the author of this work.

[c] The following chapter/section/paragraph is based on [43]. The main scientific research as well as the textual elaboration of the publication were performed by the author of this work.

[d] The following chapter/section/paragraph is based on [44]. The main scientific research as well as the textual elaboration of the publication were co-authored by the author of this work.

Chapter 2

Fundamentals of Potential Flow

This chapter aims to review the assumptions that allow simplifying the Navier-Stokes equations to the full-potential equation. These assumptions determine the range of application of the proposed potential solver. To this end, Section 2.1 starts introducing the Navier-Stokes equations, and dimensional analysis is used to compare the relative importance of their different terms. It also shows that typical aerodynamic flows have high Reynolds numbers. Section 2.2 explains how the high Reynolds number property allows neglecting the viscous terms outside of boundary layers, wakes, and shock waves. In the absence of heat addition due to radiation or combustion, this permits assuming that the flow is isentropic. Moreover, it is shown that these same conditions are enough to assume that the flow is irrotational, which means that the velocity vector can be expressed as the gradient of a scalar potential value. Section 2.3 introduces the full-potential equation, its mixed type nature, and the necessary boundary conditions for closure. Finally, Section 2.4 introduces the three main approaches to compute the aerodynamic loads acting on a body.

2.1 Navier-Stokes equations

In most aerodynamic applications regarding aircraft design, the geometry representative length scale c (e.g., the wing's chord) is much larger than the air's molecular mean free path λ, as measured by the Knudsen number:

$$Kn = \frac{\lambda}{c} \ll 1 \tag{2.1}$$

Under this condition, air can be regarded as a continuum fluid, and it can be described at every point in space and time with the following magnitudes: velocity $\boldsymbol{u}$, density ρ, pressure p, temperature T, and specific internal energy e. The air's motion is governed by the Navier Stokes equations, which in Cartesian coordinates can be written as:

$$\frac{\partial \rho}{\partial t} + \nabla \cdot (\rho \boldsymbol{u}) = 0 \tag{2.2}$$

$$\rho \frac{\partial \boldsymbol{u}}{\partial t} + \rho \boldsymbol{u} \cdot \nabla \boldsymbol{u} = -\nabla p + \nabla \cdot \bar{\bar{\boldsymbol{\tau}}} + \rho \boldsymbol{f} \tag{2.3}$$

$$\rho \frac{\partial e}{\partial t} + \rho \boldsymbol{u} \cdot \nabla e = -p \nabla \cdot \boldsymbol{u} + \nabla \cdot (k \nabla T) + \bar{\bar{\boldsymbol{\tau}}} : \nabla \boldsymbol{u} + Q \tag{2.4}$$

where t represents time, $\bar{\bar{\boldsymbol{\tau}}}$ the viscous stress tensor, $\boldsymbol{f}$ the body forces, k the thermal conductivity, and Q the thermal heating rate due to radiation or combustion. In the following, adiabatic flow is considered ($Q = 0$). For Newtonian isotropic fluids, the viscous stress tensor is typically written as:

$$\bar{\bar{\boldsymbol{\tau}}} = \mu \left[\nabla \boldsymbol{u} + (\nabla \boldsymbol{u})^T - \frac{2}{3} \nabla \cdot \boldsymbol{u} \right] \tag{2.5}$$

where μ is the dynamic viscosity.

The Navier Stokes equations express the conservation laws of mass (Eq. (2.2)), momentum (Eq. (2.3)), and energy (Eq. (2.4)). They are a set of 5 coupled differential equations with 7 unknowns ($\boldsymbol{u}$, ρ, p, T, and e). Thus, an additional 2 equations are necessary for closure (7 equations for 7 unknowns). Over a wide range of temperatures and pressures, air can be considered an ideal gas. Thus, it can be described by 2 equations of state: the ideal gas law and Joule's second law. The ideal gas law reads:

$$p = \rho R_g T \tag{2.6}$$

where R_g is the specific gas constant. Moreover, Joule's second law states that the internal energy of an ideal gas depends only on its temperature. For external aerodynamic flows, air behaves as a calorically perfect gas, so Joule's second law can be written as:

$$e = e_{\text{ref}} + c_v T \tag{2.7}$$

where e_{ref} is a reference value, and c_v is the specific heat at constant volume.

2.1.1 Initial and boundary conditions

In addition to the above equations, appropriate initial and boundary conditions have to be specified. Note that in the Navier Stokes appear first derivatives

of velocity, density and specific internal energy with respect to time. Hence, the initial distribution of these variables has to be given:

$$\boldsymbol{u} = \boldsymbol{u}_0(\boldsymbol{x}), \quad \rho = \rho_0(\boldsymbol{x}) \quad \text{and} \quad T = T_0(\boldsymbol{x}) \quad \text{in} \quad t = 0 \tag{2.8}$$

Alternatively, the initial distribution of two variables other than ρ and T can be given, since all of the thermodynamic variables of an homogeneous fluid can be obtained as a function of another two using the state equations.

The number of boundary conditions necessary to define a problem is determined by the highest order of the spatial derivatives that appear in the governing equations. In the Navier Stokes equations, the terms that contain higher spatial derivatives are the viscous term in the momentum equation and the heat conduction term in the energy equation. The former contains second-order derivatives of the velocity, and the latter contains second-order derivatives of the temperature. There are many types of possible boundary conditions depending on the type of flows under consideration. In general, the boundary conditions are combinations of the two following types:

1. When the fluid extends to infinity, the far-field (or freestream) conditions of the velocity and two thermodynamic variables have to be given:

$$\boldsymbol{u} \to \boldsymbol{u}_\infty, \quad \rho \to \rho_\infty, \quad T \to T_\infty \tag{2.9}$$

2. When the fluid is limited by a solid or by another fluid, local thermodynamic equilibrium between both phases requires continuity of velocity and temperature across the boundary:

$$\boldsymbol{u} = \boldsymbol{u}_i(\boldsymbol{x}, t) \quad \text{and} \quad T = T_i(\boldsymbol{x}, t) \quad \text{at the interface between phases.} \tag{2.10}$$

2.1.2 Non-dimensionalization

It is convenient to write the Navier Stokes equations in dimensionless form to compare the orders of magnitude of the different terms. Using the freestream conditions, a reference length scale c, a reference time scale t_{ref}, and the gravity g as representative magnitudes, the following dimensionless variables and gradient operator can be defined:

$$\begin{aligned} &\boldsymbol{u}' = \frac{\boldsymbol{u}}{u_\infty}, \quad \rho' = \frac{\rho}{\rho_\infty}, \quad p' = \frac{p}{p_\infty}, \quad \mu' = \frac{\mu}{\mu_\infty}, \qquad \boldsymbol{f}' = \frac{\boldsymbol{f}}{g}, \\ &e' = \frac{e}{e_\infty}, \quad T' = \frac{T}{T_\infty}, \quad k' = \frac{k}{k_\infty}, \quad t' = \frac{t}{t_{\text{ref}}}, \quad \nabla'(\,) = c\nabla(\,) \end{aligned} \tag{2.11}$$

Substituting Eq. (2.11) in the Navier Stokes equations (Eqs. (2.2) to (2.4)) yields:

$$St\frac{\partial \rho'}{\partial t'} + \nabla' \cdot (\rho' \boldsymbol{u}') = 0 \tag{2.12}$$

$$St\rho'\frac{\partial \boldsymbol{u}'}{\partial t'} + \rho' \boldsymbol{u}' \cdot \nabla' \boldsymbol{u}' = -\frac{1}{M_\infty^2 \gamma}\nabla' p' + \frac{1}{Re}\nabla' \cdot \bar{\bar{\boldsymbol{\tau}}}' + \frac{1}{Fr}\rho' \boldsymbol{f}' \tag{2.13}$$

$$St\rho'\frac{\partial e'}{\partial t'} + \rho' \boldsymbol{u}' \cdot \nabla e' = -(\gamma - 1)p'\nabla' \cdot \boldsymbol{u}' + \frac{\gamma}{RePr}\nabla' \cdot (k'\nabla' T') + \frac{M_\infty^2 \gamma(\gamma - 1)}{Re}\bar{\bar{\boldsymbol{\tau}}}' : \nabla \boldsymbol{u}' \tag{2.14}$$

where St, M, γ, Re, Fr, and Pr are dimensionless numbers introduced in the following.

Strouhal number

The Strouhal number St (also called reduced frequency) is a dimensionless quantity that compares the unsteady terms with the convective terms in Eqs. (2.12) to (2.14). It is defined as:

$$St = \frac{\text{unsteady term}}{\text{convective term}} = \frac{1/t_{\text{ref}}}{u_\infty / c} = \frac{c}{u_\infty t_{\text{ref}}} \tag{2.15}$$

Note that in this definition a reference frequency f_{ref} can be used instead of the reference time $f_{\text{ref}} = 1/t_{\text{ref}}$. The Strouhal number can also be interpreted as the ratio between the residence time $t_{\text{r}} = c/u_\infty$ and the reference time t_{ref}:

$$St = \frac{\text{residence time}}{\text{reference time}} = \frac{t_{\text{r}}}{t_{\text{ref}}} = \frac{c/u_\infty}{t_{\text{ref}}} = \frac{c}{u_\infty t_{\text{ref}}} \tag{2.16}$$

The residence time is the time that takes a fluid particle, moving at the freestream velocity u_∞, to travel across a region of length c. Note that both definitions are equivalent. In this work steady state flows are considered (i.e. $St \ll 1$) and so, the unsteady terms in Eqs. (2.12) to (2.14) are neglected.

Reynolds number

The Reynolds number Re is a dimensionless quantity that compares the convective terms and the viscous terms in Eqs. (2.13) and (2.14). It is defined as:

$$Re = \frac{\text{convective term}}{\text{viscous term}} = \frac{\rho_\infty u_\infty c}{\mu_\infty} \tag{2.17}$$

For typical aerodynamic applications, outside of boundary layers, wakes, and shock waves, the reference values have the following orders of magnitude:

$$\rho_\infty \sim 1\,\mathrm{kg/m^3}, \quad u_\infty \sim 10^2\mathrm{m/s}, \quad c \sim 1\,\mathrm{m}, \quad \mu_\infty \sim 10^{-5}\mathrm{Ns/m^2} \tag{2.18}$$

which yields:

$$Re \sim \frac{1\,\mathrm{kg/m^3} \cdot 10^2\mathrm{m/s} \cdot 1\,\mathrm{m}}{10^{-5}\mathrm{Ns/m^2}} = 10^7 \gg 1 \tag{2.19}$$

Mach number

The Mach number M is a dimensionless quantity defined as the ratio between the local velocity and the local speed of sound:

$$M = \frac{u}{a} \tag{2.20}$$

where the local speed of sound a is given by [45]:

$$a^2 = \left.\frac{\partial p}{\partial \rho}\right|_{s=\mathrm{const}} \tag{2.21}$$

The Mach number measures the compressibility of the fluid. Table 2.1 shows that flight can be classified in different categories according to the Mach number.

Regime	**Mach number**
Incompressible	< 0.3
Subsonic	$0.3 - 0.7$
Transonic	$0.7 - 1.2$
Supersonic	$1.2 - 5.0$
Hypersonic	$5.0 - 10.0$
High-hypersonic	$10.0 - 25.0$
Re-entry speeds	> 25.0

Table 2.1: Flight categories.

In this work, the incompressible, the subsonic, and the low transonic $(0.7-0.9)$ flight regimes are considered.

Ratio of specific heats

The ratio of specific heats γ is defined as:

$$\gamma = \frac{c_p}{c_v} \tag{2.22}$$

where c_p and c_v are the specific heat capacities at constant pressure and volume respectively. For air γ is:

$$\gamma = \frac{c_p}{c_v} = \frac{1.005\,\mathrm{kJ/kgK}}{0.718\,\mathrm{kJ/kgK}} = 1.4 \tag{2.23}$$

Froude number

The Froude number Fr measures the relative importance of the gravity forces with respect to the convective term:

$$Fr = \frac{\text{convective term}}{\text{gravity term}} = \frac{u_\infty^2}{gc} \tag{2.24}$$

For typical aerodynamic flows $g \sim 10\,\mathrm{m^2/s}$, which results in the following Froude number's order of magnitude:

$$Fr \sim \frac{10^4 \mathrm{m/s}}{10\,\mathrm{m^2/s} \cdot 1\,\mathrm{m}} = 10^3 \gg 1 \tag{2.25}$$

so the body forces term can be neglected in Eq. (2.13).

Prandtl number

The Prandtl number Pr compares the momentum diffusivity to the thermal diffusivity:

$$\mathrm{Pr} = \frac{\text{momentum diffusivity}}{\text{thermal diffusivity}} = \frac{c_p \mu_\infty}{k_\infty} \tag{2.26}$$

For air the Prandtl number is $\mathrm{Pr} = 0.72$.

2.2 High Reynolds number flow

As shown in Section 2.1, for typical aerodynamic applications, the Reynolds number outside boundary layers, wakes, and shock waves is very large ($Re \gg 1$). Therefore, the viscous and heat convection terms in the momentum and

energy Navier Stokes equations (Eqs. (2.13) and (2.14)) are typically neglected. The Navier Stokes equations can be then simplified to:

$$\frac{\partial \rho}{\partial t} + \nabla \cdot (\rho \boldsymbol{u}) = 0 \tag{2.27}$$

$$\rho \frac{\partial \boldsymbol{u}}{\partial t} + \rho \boldsymbol{u} \cdot \nabla \boldsymbol{u} = -\nabla p \tag{2.28}$$

$$\rho \frac{\partial e}{\partial t} + \rho \boldsymbol{u} \cdot \nabla e = -p \nabla \cdot \boldsymbol{u} \tag{2.29}$$

where adiabatic flow ($Q = 0$) and negligible body forces ($Fr \gg 1$) are assumed. Eqs. (2.27) to (2.29) are a simplified version of Euler equations. Figure 2.1 illustrates the different flow regions outside streamlined bodies with attached boundary layers flying at large Reynolds numbers. Under these conditions, boundary layers, wakes, and shock waves are so thin that they are typically modeled as discontinuities (lines in 2D or surfaces in 3D). Across these discontinuities, the fluid magnitudes and their derivatives can present finite jumps.

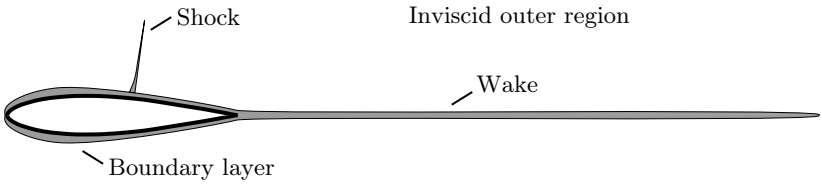

Figure 2.1: Inviscid and viscous flow regions. For large Reynolds numbers viscous and heat convection effects only remain in the boundary layer, the wake, and the shock waves.

2.2.1 Isentropic flow

Euler's energy equation (Eq. (2.29)) can be written in terms of the specific entropy s as:

$$\frac{\partial s}{\partial t} + \boldsymbol{u} \cdot \nabla s = 0 \qquad \rightarrow \qquad s = \text{constant} \tag{2.30}$$

which means that inviscid adiabatic flows are isentropic. The following relation holds between pressure and density for isentropic calorically perfect gases:

$$\frac{p}{\rho^{\gamma}} = \text{constant} \tag{2.31}$$

2.2.2 Steady compressible Bernoulli equation

Projecting Euler's momentum equation (Eq. (2.28)) along the streamlines and assuming steady flow (i.e. $St \ll 1$) yields:

$$\frac{1}{2}\frac{\partial u^2}{\partial l} + \frac{1}{\rho}\frac{\partial p}{\partial l} = 0 \tag{2.32}$$

which can be integrated using the isentropic relation Eq. (2.31) to obtain the compressible Bernoulli equation:

$$\frac{1}{2}u^2 + \frac{a_\infty^2}{\gamma - 1}\left(\frac{p}{p_\infty}\right)^{\frac{\gamma-1}{\gamma}} = \text{constant} \tag{2.33}$$

Using the freestream conditions to evaluate the integration constant results in:

$$\frac{p}{p_\infty} = \left[1 + \frac{\gamma - 1}{2}M_\infty^2\left(1 - \frac{u^2}{u_\infty^2}\right)\right]^{\frac{\gamma}{\gamma-1}} \tag{2.34}$$

2.2.3 Irrotational flow

Vorticity is defined as:

$$\boldsymbol{\omega} = \nabla \times \boldsymbol{u} \tag{2.35}$$

Irrotationality ($\boldsymbol{\omega} = 0$) allows greatly simplifying the flow modeling. It is thus important to study the behavior of vorticity to determine under which conditions the flow is irrotational. The change of vorticity is governed by Helmholtz vorticity transport equation:

$$\frac{D}{Dt}\left(\frac{\boldsymbol{\omega}}{\rho}\right) = \frac{\boldsymbol{\omega}}{\rho}\cdot\nabla\boldsymbol{u} + \frac{\nabla\rho\times\nabla p}{\rho^3} + \frac{1}{\rho}\nabla\times\left(\frac{\nabla\bar{\bar{\boldsymbol{\tau}}}}{\rho}\right) \tag{2.36}$$

which can be derived by taking the curl of the momentum equation (Eq. (2.3)) as shown in Appendix A. Substituting Eq. (2.11) in Eq. (2.36) yields the dimensionless form of Helmholtz vorticity transport equation:

$$St\frac{\partial\left(\frac{\boldsymbol{\omega}'}{\rho'}\right)}{\partial t'} + \boldsymbol{u}'\cdot\nabla'\left(\frac{\boldsymbol{\omega}'}{\rho'}\right) = \frac{\boldsymbol{\omega}'}{\rho'}\cdot\nabla'\boldsymbol{u}' + \frac{1}{M_\infty^2\gamma}\frac{\nabla'\rho'\times\nabla'p'}{{\rho'}^3} + \frac{1}{Re}\frac{1}{\rho'}\nabla'\times\left(\frac{\nabla'\bar{\bar{\boldsymbol{\tau}}}'}{\rho'}\right) \tag{2.37}$$

Note that for high Reynolds numbers the viscous term can be neglected. For isentropic flow the gradients of pressure and density are parallel and thus the baroclinic term $\nabla\rho \times \nabla p$ vanishes. Moreover, if the flow upstream aerodynamic bodies is uniform, the vorticity is initially zero ($\boldsymbol{\omega}_\infty = 0$) and the term $\boldsymbol{\omega} \cdot \nabla \boldsymbol{u}$ also vanishes. Thus, for high Reynolds numbers Helmholtz vorticity transport equation (Eq. (2.36)) can be simplified to:

$$\frac{D}{Dt}\left(\frac{\boldsymbol{\omega}}{\rho}\right) = 0 \qquad \rightarrow \qquad \boldsymbol{\omega} = 0 \tag{2.38}$$

The physical meaning of Eq. (2.38) is that for high Reynolds numbers, the vorticity that is created at the body's boundary is convected along with the flow at a much faster rate than it is diffused out across the flow. Thus, the vorticity remains confined in the boundary layer and the wake if the boundary layer is attached. Eq. (2.38) states that under the assumption of initial zero vorticity ($\boldsymbol{\omega}_\infty = 0$), isentropic flows are also irrotational $\boldsymbol{\omega} = 0$. If the flow is irrotational, it can be shown that by definition, the velocity is the gradient of a velocity potential ϕ:

$$\boldsymbol{u} = \boldsymbol{u}_\infty + \nabla\phi \tag{2.39}$$

2.3 Full-potential equation

In the previous sections it is shown that typical aerodynamic flows can be assumed to be steady, irrotational and isentropic. This allows reducing the five coupled Navier Stokes equations (Eqs. (2.2) to (2.4)) to a single scalar partial differential equation, namely the full-potential equation. The full-potential equation is derived from the continuity equation (Eqs. (2.2) and (2.27)), and can be written as:

$$\nabla \cdot (\rho(\boldsymbol{u}_\infty + \nabla\phi)) = 0 \tag{2.40}$$

where the following density expression can be derived from the compressible Bernoulli equation (Eq. (2.34)) and the isentropic relation for calorically perfect gases (Eq. (2.31)):

$$\rho = \rho_\infty \left[1 + \frac{\gamma - 1}{2} M_\infty^2 \left(1 - \frac{u^2}{u_\infty^2}\right)\right]^{\frac{1}{\gamma - 1}} \tag{2.41}$$

2.3.1 Classification of the full-potential equation

To classify the full-potential equation, consider first the standard form of second-order partial differential equations, which is:

$$A\frac{\partial^2 f}{\partial x^2} + B\frac{\partial^2 f}{\partial xy} + C\frac{\partial^2 f}{\partial y^2} = F \tag{2.42}$$

where f is the sought function, and A, B, C and F are functions of x, y, f, $\partial f/\partial x$, and $\partial f/\partial y$. Eq. (2.42) can be classified by considering the corresponding characteristic equation:

$$A\left(\frac{dy}{dx}\right)^2 - B\left(\frac{dy}{dx}\right) + C = 0 \tag{2.43}$$

where the two characteristic directions associated with Eq. (2.42) can be determined using the quadratic formula:

$$\left(\frac{dy}{dx}\right) = \frac{B \pm \sqrt{B^2 - 4AC}}{2A} \tag{2.44}$$

The sign of the discriminant $B^2 - 4AC$ determines the equation classification. The equation is elliptic if the discriminant is smaller than zero ($B^2 - 4AC < 0$), parabolic if the discriminant is zero ($B^2 - 4AC = 0$), and hyperbolic if the discriminant is larger than zero ($B^2 - 4AC > 0$).

The full-potential equation (Eq. (2.40)) is a second-order partial differential equation. However, it is difficult to classify because it is not in standard form (Eq. (2.42)). The standard form is achieved by transforming Eq. (2.40) into nonconservative form, which in two-dimensional Cartesian coordinates is written as:

$$\left[a^2 - \left(\frac{\partial\phi}{\partial x}\right)^2\right]\frac{\partial^2\phi}{\partial^2 x} - 2\frac{\partial\phi}{\partial x}\frac{\partial\phi}{\partial y}\frac{\partial^2\phi}{\partial x\partial y} + \left[a^2 - \left(\frac{\partial\phi}{\partial y}\right)^2\right]\frac{\partial^2\phi}{\partial^2 y} = 0 \tag{2.45}$$

where the local speed of sound is:

$$a = a_\infty\left[1 + \frac{\gamma - 1}{2}M_\infty^2\left(1 - \frac{u^2}{u_\infty^2}\right)\right]^{\frac{1}{2}} \tag{2.46}$$

The dimensionless discriminant of Eq. (2.45) is:

$$\frac{\mathrm{B}^2 - 4\mathrm{AC}}{a_\infty^4} = 4\frac{a^2(u^2 - a^2)}{a_\infty^4} = 4\frac{a^4}{a_\infty^4}(M^2 - 1) \tag{2.47}$$

which is plotted in Figure 2.2 over the local Mach number. Note that the discriminant is negative for subsonic flow ($M < 1$), zero for sonic flow ($M = 1$), and positive for supersonic flow ($M > 1$) [46]. Hence, the full-potential equation is elliptic for subsonic flow, parabolic for sonic flow, and hyperbolic for supersonic flow (see Table 2.2).

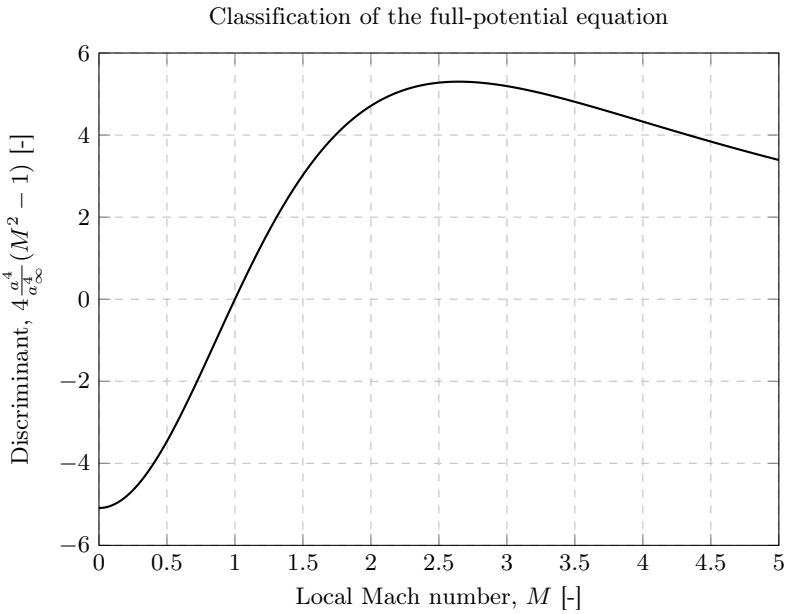

Figure 2.2: The discriminant is negative for subsonic flow ($M < 1$), zero for sonic flow ($M = 1$), and positive for supersonic flow ($M > 1$).

Regime	Mach number	Discriminant	Classification
Subsonic	< 1	< 0	Elliptic
Sonic	$= 1$	$= 0$	Parabolic
Supersonic	> 1	> 0	Hyperbolic

Table 2.2: Classification of the full-potential equation.

2.3.2 Boundary conditions

Figure 2.3 illustrates the fluid domain and its boundaries. The far-field boundary is divided into inlet and outlet using the following criteria:

$$\text{Far field} = \begin{cases} \text{Inlet} & \text{if} \quad \boldsymbol{u}_\infty \cdot \hat{\boldsymbol{n}} < 0 \\ \text{Outlet} & \text{if} \quad \boldsymbol{u}_\infty \cdot \hat{\boldsymbol{n}} > 0 \end{cases} \tag{2.48}$$

where $\hat{\boldsymbol{n}}$ is the far-field boundary outer normal vector. In Figure 2.3 it is shown that the wake intersects the outlet.

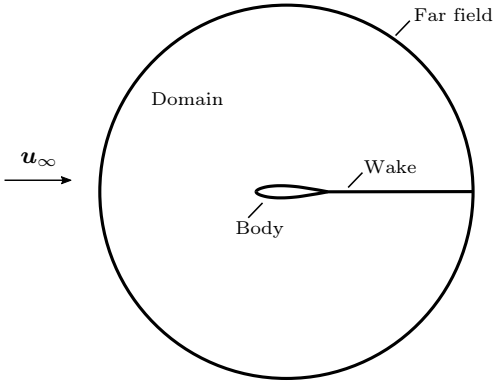

Figure 2.3: Fluid domain and its boundaries in 2D.

Dirichlet condition

A Dirichlet condition is necessary because the full-potential equation and the remaining boundary conditions are only defined in terms of the velocity potential derivatives. The Dirichlet condition cannot be applied at the outlet because the wake intersects the outlet and there is a jump in the potential across the wake. Instead, the Dirichlet condition is applied at the inlet:

$$\phi = \phi_\infty \qquad \text{on the inlet} \tag{2.49}$$

where ϕ_∞ is an arbitrary value.

Freestream conditions

At infinity, the disturbance $\nabla\phi$ induced by the body on the flow vanishes:

$$\lim_{x\to\infty} \nabla\phi = 0 \tag{2.50}$$

This condition is applied at the outlet as a Neumann condition:

$$\hat{\boldsymbol{n}} \cdot (\rho\boldsymbol{u}) = \hat{\boldsymbol{n}} \cdot (\rho_\infty \boldsymbol{u}_\infty) \qquad \text{on the outlet} \tag{2.51}$$

Note that the far-field boundary is illustrated in Figure 2.3 as a circle with finite radius but is theoretically at an infinite distance away from the body. In practice, the far-field boundary is typically modeled at a distance 50 times the reference length of the body [47].

Slip condition

Without viscosity, the no-slip boundary condition at the interface between the flow and the body cannot be enforced. Instead, a slip condition is applied. The slip boundary condition is illustrated in Figure 2.4. The slip condition sets the velocity component normal to the body to zero, remaining the tangential velocity component arbitrary:

$$\hat{\boldsymbol{n}} \cdot (\rho \boldsymbol{u}) = 0 \qquad \text{on the body} \tag{2.52}$$

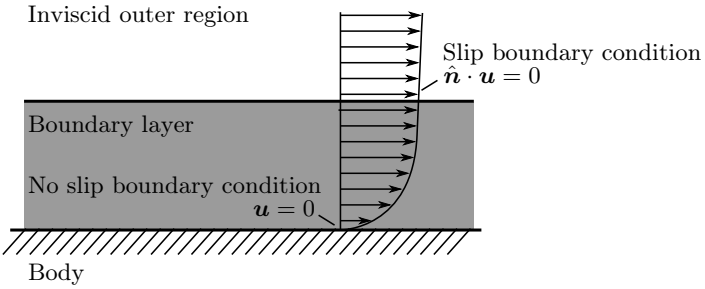

Figure 2.4: The no-slip boundary condition cannot be enforced in inviscid flows. A slip boundary condition is applied instead.

Wake boundary conditions

The wake is modeled as a straight surface in the freestream direction. This assumption neglects the roll-up and downwash effects but avoids iteratively computing the wake's geometry, which is an expensive process. In order to relax the straight wake assumption, mass flux is allowed across the wake. The conservation of mass across the wake is enforced by applying:

$$\hat{\boldsymbol{n}} \cdot (\rho_{\mathrm{u}} \boldsymbol{u}_{\mathrm{u}} - \rho_{\mathrm{l}} \boldsymbol{u}_{\mathrm{l}}) = 0 \qquad \text{across the wake} \tag{2.53}$$

where $\hat{\boldsymbol{n}}$ is the normal vector to the wake pointing upwards and the subscripts u and l stand for the upper and lower wake. Because the wake is thin, it cannot support pressure jumps. The pressure equality condition is imposed by:

$$|\boldsymbol{u}_{\mathrm{u}}|^2 - |\boldsymbol{u}_{\mathrm{l}}|^2 = 0 \qquad \text{across the wake} \tag{2.54}$$

2.4 Aerodynamic loads

This section introduces three different approaches to compute the forces acting on a body. For a detail discussion see [48].

2.4.1 Near-field analysis

In potential flow, the aerodynamic force vector $\mathbf{F}$ depends only on the pressure normal forces because the viscous stress forces are neglected. As illustrated in Figure 2.5, the force can be computed by integrating the pressure forces over the body's surface:

$$\mathbf{F} = \oint_{\text{body}} p\, \hat{\boldsymbol{n}}\, \mathrm{d}S = \oint_{\text{body}} (p - p_\infty)\, \hat{\boldsymbol{n}}\, \mathrm{d}S \tag{2.55}$$

where $\hat{\boldsymbol{n}}$ is the unit normal vector pointing outside of the domain. Lift, drag, and sideforce can be computed by projecting the body force:

$$L = \mathbf{F} \cdot \hat{\mathbf{k}} = \oint_{\text{body}} (p - p_\infty)\, \hat{\boldsymbol{n}} \cdot \hat{\mathbf{k}}\, \mathrm{d}S \tag{2.56}$$

$$Y = \mathbf{F} \cdot \hat{\mathbf{j}} = \oint_{\text{body}} (p - p_\infty)\, \hat{\boldsymbol{n}} \cdot \hat{\mathbf{j}}\, \mathrm{d}S \tag{2.57}$$

$$D = \mathbf{F} \cdot \hat{\mathbf{i}} = \oint_{\text{body}} (p - p_\infty)\, \hat{\boldsymbol{n}} \cdot \hat{\mathbf{i}}\, \mathrm{d}S \tag{2.58}$$

where a wind coordinate system is chosen in which the x-axes points in the direction of the freestream, $\boldsymbol{u}_\infty = u_\infty \hat{\mathbf{i}}$, the y-axes is in the body span

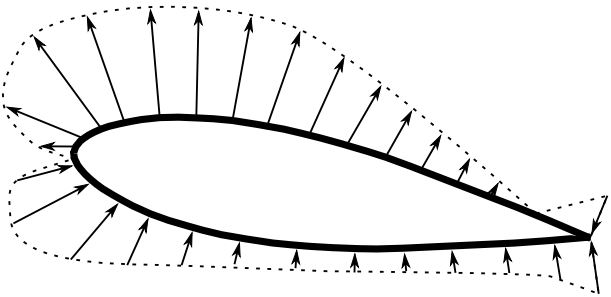

Figure 2.5: Sketch of the pressure forces acting on an airfoil.

direction, and the z-axes points upwards. D'Alambert's paradox states that in 2D inviscid flow drag is zero:

$$D = 0 \qquad \text{(2D inviscid flow)} \tag{2.59}$$

2.4.2 Far-field analysis

Another way to compute the aerodynamic loads is by considering a control volume enclosing the body such as the one illustrated in Figure 2.6. The integral form of Eq. (2.28) can be obtained using Gauss's Theorem:

$$\oint \left[\rho(\boldsymbol{u}\cdot\hat{\boldsymbol{n}})\boldsymbol{u} + p\,\hat{\boldsymbol{n}}\right]\,\mathrm{d}S = 0 \tag{2.60}$$

where steady flow is assumed. The integral can be split into three parts:

$$\oint[\quad]\,\mathrm{d}S = \oint_{\text{body}}[\quad]\,\mathrm{d}S + \oint_{\text{outer}}[\quad]\,\mathrm{d}S + \oint_{\text{cut}}[\quad]\,\mathrm{d}S = 0 \tag{2.61}$$

The cut contribution vanishes because the contributions corresponding to the two boundaries defining the cut cancel each other:

$$\oint_{\text{cut}}[\quad]\,\mathrm{d}S = 0 \tag{2.62}$$

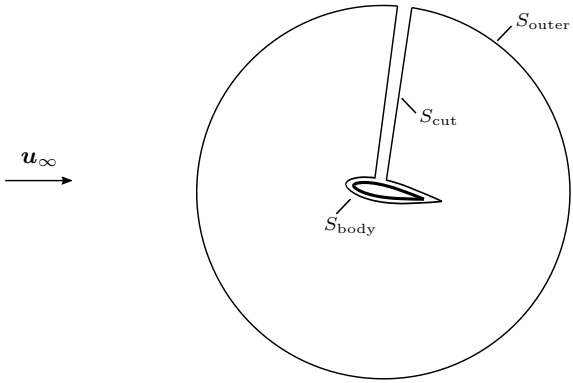

Figure 2.6: Control volume enclosing the body.

Moreover, the contribution corresponding to the body's surface is:

$$\oint_{\text{body}} \left[\rho(\boldsymbol{u}\cdot\hat{\boldsymbol{n}})\boldsymbol{u} + p\,\hat{\boldsymbol{n}}\right]\,\mathrm{d}S = \oint_{\text{body}} p\,\hat{\boldsymbol{n}}\,\mathrm{d}S = \mathbf{F} \tag{2.63}$$

where the slip boundary condition has been used ($\boldsymbol{u}\cdot\hat{\boldsymbol{n}} = 0$). Substituting Eqs. (2.62) and (2.63) in Eq. (2.60) yields the integral momentum theorem, which relates the forces acting on the body with the fluid magnitudes on the control volume's outer surface:

$$\mathbf{F} = -\oint_{\text{outer}} \left[(p - p_\infty)\,\hat{\boldsymbol{n}} + \rho(\boldsymbol{u}\cdot\hat{\boldsymbol{n}})(\boldsymbol{u} - \boldsymbol{u}_\infty)\right]\,\mathrm{d}S = 0 \tag{2.64}$$

2.4.3 Wake potential jump analysis

A third way to compute the forces is by considering the link between the forces and the potential jump across the wake in its intersection with the Trefftz plane. The Trefftz plane, or wake integration plane, is situated aft of the wing and orientated perpendicular to the freestream (i.e., parallel to the yz-plane), as illustrated in Figure 2.7. The pressure equality condition across the wake (Eq. (3.6)) can be expressed as:

$$\begin{aligned}
\boldsymbol{u}_\mathrm{u}\cdot\boldsymbol{u}_\mathrm{u} - \boldsymbol{u}_\mathrm{l}\cdot\boldsymbol{u}_\mathrm{l} &= 0\\
\frac{1}{2}(\boldsymbol{u}_\mathrm{u} + \boldsymbol{u}_\mathrm{l})\cdot(\boldsymbol{u}_\mathrm{u} - \boldsymbol{u}_\mathrm{l}) &= 0\\
\boldsymbol{u}_a\cdot(\boldsymbol{u}_\mathrm{u} - \boldsymbol{u}_\mathrm{l}) &= 0\\
\boldsymbol{u}_a\cdot\Delta\boldsymbol{u} &= 0\\
\boldsymbol{u}_a\cdot\nabla(\Delta\phi) &= 0
\end{aligned} \tag{2.65}$$

where $\boldsymbol{u}_a$ is the average wake velocity, which for a straight wake can be approximated with $\boldsymbol{u}_\infty$. This results in:

$$\boldsymbol{u}_\infty\cdot\nabla(\Delta\phi) = 0 \tag{2.66}$$

which states that the potential jump is constant along the wake streamlines. Using this result, it can be shown that the forces are [48]:

$$L = \rho_\infty u_\infty \int_{y_{\min}}^{y_{\max}} \Delta\phi\,\mathrm{d}y \tag{2.67}$$

$$Y = -\rho_\infty u_\infty \int_{z_{\min}}^{z_{\max}} \Delta\phi\,\mathrm{d}z \tag{2.68}$$

$$D = -\frac{1}{2}\rho_\infty \int_{-b/2}^{b/2} \Delta\phi\,\boldsymbol{u}\cdot\hat{\boldsymbol{n}}\,\mathrm{d}s \tag{2.69}$$

The integrals in Eqs. (2.67) to (2.69) are defined along the intersection between the wake and Trefftz plane.

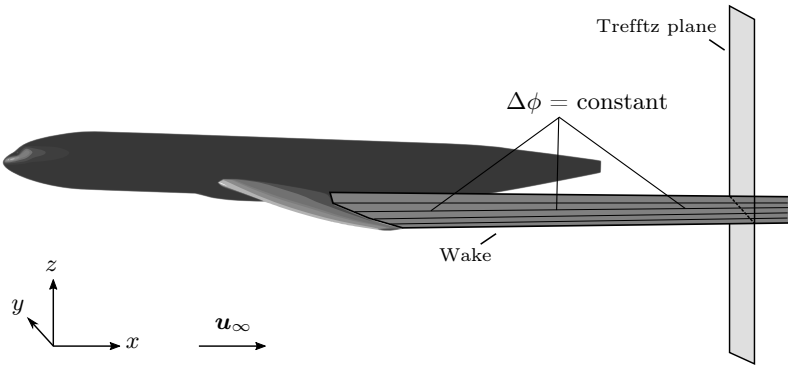

Figure 2.7: The potential jump $\Delta\phi$ is constant along the wake streamlines and is used in the Trefftz plane to compute the aerodynamic loads.

Chapter 3

An Embedded Wake Approach for Potential Transonic Solvers[ab]

This chapter presents the proposed embedded wake approach for the solution of potential transonic flow using the finite element method. Section 3.1 introduces the strong form, the domain's model considered in this work, and the boundary conditions. Section 3.2 presents the finite element discretization using a Galerkin approach. Section 3.3 briefly describes the artificial compressibility method used to stabilize the problem in supersonic flow regions and to capture shock waves. Section 3.4 explains the problem of having areas of high velocity when assuming isentropic flow and the remedy used in the proposed approach. Section 3.5 presents the embedded wake approach in detail, which is the novelty of this work. Finally, Section 3.6 describes the implementation of the potential transonic solver, using the proposed embedded wake approach, in KRATOS Multiphysics.

3.1 Strong form, domain, and boundary conditions

The strong form is the full-potential equation, which is presented together with its boundary conditions in Section 2.3, and they are briefly repeated here for completeness. The full-potential equation is the continuity equation:

$$\nabla \cdot (\rho \boldsymbol{u}) = 0 \tag{3.1}$$

where, assuming irrotational flow, the velocity can be expressed using the freestream velocity $\boldsymbol{u}_\infty$ and the gradient of the scalar potential ϕ as:

$$\boldsymbol{u} = \boldsymbol{u}_\infty + \nabla\phi \tag{3.2}$$

For compressible isentropic flow, the density is:

$$\rho = \rho_\infty \left[1 + \frac{\gamma - 1}{2} M_\infty^2 \left(1 - \frac{u^2}{u_\infty^2}\right)\right]^{\frac{1}{\gamma - 1}} \tag{2.41 revisited}$$

In this dissertation, the flow field is modeled using rectangular domains. Figures 3.1 and 3.2 illustrate the fluid domain and its boundaries in two and three dimensions, respectively.

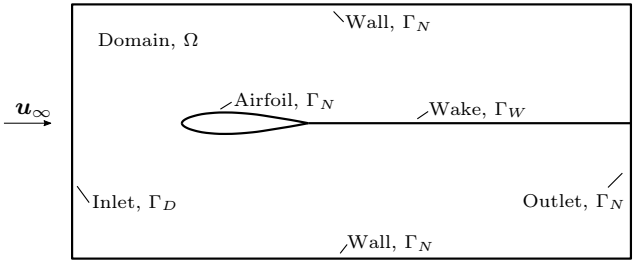

Figure 3.1: Fluid domain and its boundaries in 2D.

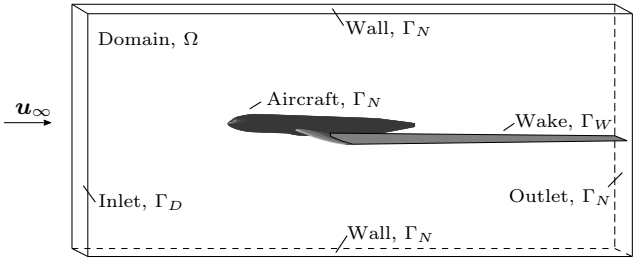

Figure 3.2: Fluid domain and its boundaries in 3D.

The boundary conditions are (see Section 2.3.2):

$$\phi = \phi_\infty \qquad \text{on } \Gamma_D \tag{3.3}$$

$$\hat{\boldsymbol{n}} \cdot (\rho \boldsymbol{u}) = q \qquad \text{on } \Gamma_N \tag{3.4}$$

$$\hat{\boldsymbol{n}} \cdot (\rho_\mathrm{u} \boldsymbol{u}_\mathrm{u} - \rho_\mathrm{l} \boldsymbol{u}_\mathrm{l}) = 0 \qquad \text{on } \Gamma_W \tag{3.5}$$

$$|\boldsymbol{u}_\mathrm{u}|^2 - |\boldsymbol{u}_\mathrm{l}|^2 = 0 \qquad \text{on } \Gamma_W \tag{3.6}$$

At the outlet, the freestream conditions are specified as a Neumann condition using Eq. (3.4) and setting $q = \hat{\boldsymbol{n}} \cdot (\rho_\infty \boldsymbol{u}_\infty)$. On the body and walls, a slip condition is applied ($q = 0$).

3.2 Finite element discretization

Equation (3.1) is discretized using a standard Galerkin approach. Here unstructured meshes with linear triangular and tetrahedral elements are used. Weighting Eq. (3.1) with the test function N and discretizing into finite elements results in:

$$\sum_e \int_{\Omega_e} N \nabla \cdot (\rho \boldsymbol{u}) \; d\Omega_e = 0 \tag{3.7}$$

being Ω_e each element's domain. Using integration by parts, applying the divergence theorem, and inserting Eq. (3.4) yields:

$$\sum_e \int_{\Omega_e} \nabla N \cdot (\rho \boldsymbol{u}) \; d\Omega_e = \sum_c \int_{\Gamma_c} N q \; d\Gamma_c \tag{3.8}$$

where Γ_c is the boundary of element c. Equation (3.8) can be rewritten in residual form using Einstein notation as:

$$R^i = \sum_e \int_{\Omega_e} \frac{\partial N^i}{\partial x^a} \rho u^a \; d\Omega_e - \sum_c \int_{\Gamma_c} N^i q \; d\Gamma_c = 0 \tag{3.9}$$

where R^i is the residual at each node i. Equation (3.9) is solved using Newton's method:

$$J^{ij} \Delta \phi^j = -R^i \tag{3.10}$$

being $\Delta \phi^j$ the solution update and J^{ij} the corresponding Jacobian.

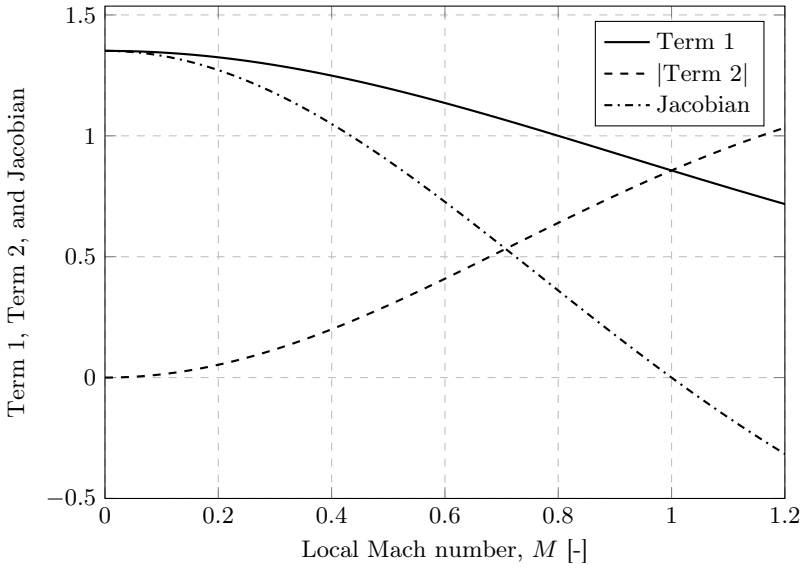

Figure 3.3: The Jacobian is positive for subsonic flow ($M < 1$), zero for sonic flow ($M = 1$), and negative for supersonic flow ($M > 1$).

The Jacobian is defined as:

$$J^{ij} = \frac{\partial R^i}{\partial \phi^j} = \sum_e \int_{\Omega_e} \frac{\partial N^i}{\partial x^a} \left(\rho \frac{\partial u^a}{\partial \phi^j} + \frac{\partial \rho}{\partial \phi^j} u^a \right) d\Omega_e \tag{3.11}$$

$$= \sum_e \int_{\Omega_e} \rho \frac{\partial N^i}{\partial x^a} \frac{\partial N^j}{\partial x^a} \, d\Omega_e \tag{3.12}$$

$$+ \sum_e \int_{\Omega_e} 2 \frac{\partial \rho}{\partial u^2} \left(\frac{\partial N^i}{\partial x^a} u^a \, u^b \frac{\partial N^j}{\partial x^b} \right) \, d\Omega_e \tag{3.13}$$

where:

$$\frac{\partial \rho}{\partial u^2} = -\frac{\rho_\infty}{2a_\infty^2} \left[1 + \frac{\gamma - 1}{2} M_\infty^2 \left(1 - \frac{u^2}{u_\infty^2} \right) \right]^{\frac{2-\gamma}{\gamma-1}} \tag{3.14}$$

For compressible flows, the Jacobian has two terms (Eqs. (3.12) and (3.13)). For a given finite element, the first term (Eq. (3.12)) is proportional to the

local density ρ, and the second term (Eq. (3.13)) is proportional to $2u^2\partial\rho/\partial u^2$. In Figure 3.3 the Jacobian and its terms are plotted over the local Mach number. Note that the second term is negative, and Figure 3.3 shows its absolute value.

For a local Mach number equal to zero (i.e., incompressible flow), the second term vanishes, and the Jacobian is equal to the first term (see Eq. (3.16)). As the Mach number increases, the second term increases, and the first term decreases, yielding a decreasing Jacobian. Reaching the speed of sound ($M = 1$), the first and second terms are equal, resulting in a vanishing Jacobian. Finally, for velocities beyond the speed of sound ($M > 1$), the Jacobian becomes negative. This shows that, as the full-potential equation is elliptic for subsonic flow, the Jacobian is well defined. However, for sonic and supersonic flow, the full-potential equation is respectively parabolic and hyperbolic (see Figure 2.2), and the Jacobian becomes singular.

For incompressible flows, the residual and the Jacobian become:

$$R^i = \sum_e \int_{\Omega_e} \rho_\infty \frac{\partial N^i}{\partial x^a} u^a \; d\Omega_e - \sum_c \int_{\Gamma_c} N^i q \; d\Gamma_c = 0 \tag{3.15}$$

$$J^{ij} = \frac{\partial R^i}{\partial \phi^j} = \sum_e \int_{\Omega_e} \rho_\infty \frac{\partial N^i}{\partial x^a} \frac{\partial N^j}{\partial x^a} \; d\Omega_e \tag{3.16}$$

3.3 Artificial compressibility

In order to stabilize the problem in supersonic flow regions, an artificial compressibility method is employed. This method prevents the Jacobian from becoming singular and allows capturing shock waves. The method is presented in detail in [9] and is briefly described in this section. Writing the steady adiabatic energy Navier-Stokes equation (Eq. (2.4)) in terms of the total enthalpy $h_o = h + u^2/2$, neglecting heat conduction, and retaining the viscous effects yields:

$$\rho \boldsymbol{u} \cdot \nabla h_o = \nabla \cdot (\bar{\bar{\boldsymbol{\tau}}} \cdot \boldsymbol{u}) \tag{3.17}$$

which can be rewritten as:

$$\rho \boldsymbol{u} \cdot \nabla (h_o - h_o') = 0 \tag{3.18}$$

where h_o' is due to the viscous terms. Eq. (3.18) suggests modifying the density. In [23] the following upwind scheme is proposed to compute the density:

$$\tilde{\rho} = \rho - \mu_s \left(\frac{\partial \rho}{\partial s} \right) \Delta s \approx \rho - \mu_s (\rho - \rho_{\text{up}}) \tag{3.19}$$

where ρ_{up} is the upstream element's density. The factor μ_s is defined as the switching function:

$$\mu_s = \mu_{\text{c}} \max(0, \mu, \mu_{\text{up}}) \tag{3.20}$$

where μ_c is the user-defined upwinding factor constant, and μ and μ_{up} are respectively the upwinding and upstream upwinding factors. The upwinding factors are defined as:

$$\mu = 1 - \frac{M_{crit}^2}{M^2} \tag{3.21}$$

$$\mu_{up} = 1 - \frac{M_{crit}^2}{M_{up}} \tag{3.22}$$

where M_{crit} is the user-defined critical Mach number. The user-defined upwinding factor and critical Mach number control the amount of artificial dissipation introduced into the system. Substituting the upwind density $\tilde{\rho}$ (Eq. (3.19)) for the density ρ in the residual and Jacobian derived in the previous section (Eqs. (3.9) and (3.11)) yields:

$$R^i = \sum_e \int_{\Omega_e} \frac{\partial N^i}{\partial x^a} \tilde{\rho} u^a \, d\Omega_e - \sum_c \int_{\Gamma_c} N^i q \, d\Gamma_c = 0 \tag{3.23}$$

$$J^{ij} = \frac{\partial R^i}{\partial \phi^j} = \sum_e \int_{\Omega_e} \frac{\partial N^i}{\partial x^a} \left(\tilde{\rho} \frac{\partial u^a}{\partial \phi^j} + \frac{\partial \tilde{\rho}}{\partial \phi^j} u^a \right) d\Omega_e \tag{3.24}$$

The sensitivities related to the derivative of the upwind density with respect to the degrees of freedom $\partial\tilde{\rho}/\partial\phi^j$ appearing in the second term of the Jacobian are presented in Appendix B.

3.3.1 The switching function

The switching function μ_s (Eq. (3.20)) allows distinguishing between three types of flow:

- Subsonic flow: $M < M_{crit}$
- Supersonic and accelerating flow: $M > M_{crit}$ and $M > M_{up}$
- Supersonic and decelerating flow: $M > M_{crit}$ and $M < M_{up}$

Subsonic flow

If for a given finite element the flow is subsonic, then the upwind density is equal to the density:

$$M < M_{crit} \quad \rightarrow \quad \mu < 0 \quad \rightarrow \quad \mu_s = 0 \quad \rightarrow \quad \tilde{\rho} = \rho \tag{3.25}$$

Supersonic and accelerating flow

For supersonic and accelerating flow the density is:

$$M > M_{crit} \;\rightarrow\; M > M_{up} \;\rightarrow\; \mu_s = \mu \;\rightarrow\; \tilde{\rho} = \rho - \mu(\rho - \rho_{up}) \tag{3.26}$$

Supersonic and decelerating flow

For supersonic and decelerating flow the density is:

$$M > M_{\text{crit}} \;\rightarrow\; M < M_{\text{up}} \;\rightarrow\; \mu_s = \mu_{\text{up}} \;\rightarrow\; \tilde{\rho} = \rho - \mu_{\text{up}}(\rho - \rho_{\text{up}}) \quad (3.27)$$

3.4 Limit velocity in isentropic flow

Because of the assumption of isentropic flow, for large local velocities the term in square brackets:

$$\text{Square brackets term} = \left[1 + \frac{\gamma - 1}{2}\frac{u_\infty^2}{a_\infty^2}\left(1 - \frac{u^2}{u_\infty^2}\right)\right] \quad (3.28)$$

falls below zero. Hence, the density (Eq. (2.41)) and its derivative $\partial\rho/\partial u^2$ (Eq. (3.14)) become ill-defined. This is illustrated in Figure 3.4, where the

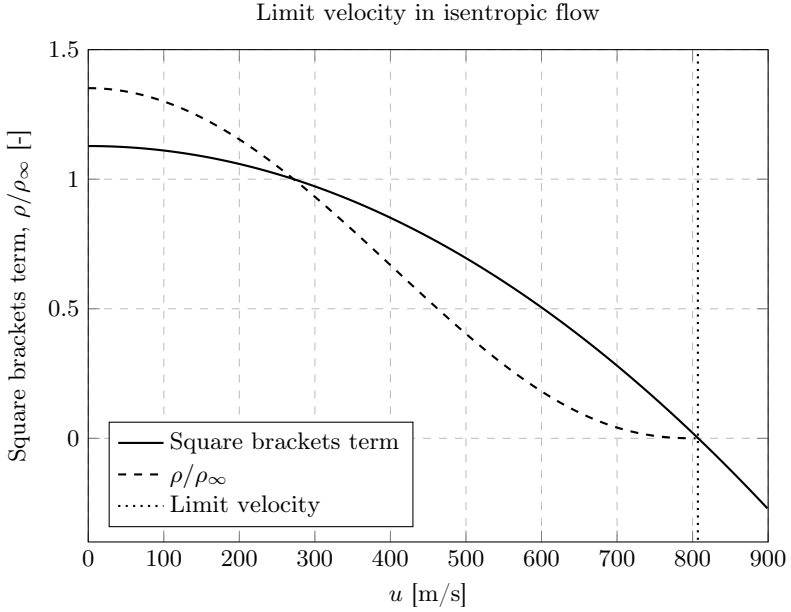

Figure 3.4: For large local velocities the term in square brackets falls below zero, yielding the density ill-defined.

square brackets term and the dimensionless density are plotted over the velocity.

In Figure 3.4 the limit velocity (or vacuum speed) is indicated with a dotted line. The limit velocity u_{lim} can be computed by equating the square brackets term in Eq. (3.28) to zero, which yields:

$$u_{\text{lim}} = u_\infty^2 \left(1 + \frac{2}{(\gamma - 1) M_\infty^2} \right) \tag{3.29}$$

The concept of limit velocity is best explained in [49], and is briefly described in this section. For steady and adiabatic flow, the total (or stagnation) enthalpy is constant:

$$h_o = h + \frac{u^2}{2} \equiv \text{constant} \tag{3.30}$$

Thus, the velocity can be expressed as:

$$u = \sqrt{2(h_o - h)} \tag{3.31}$$

Expanding the flow to the vacuum (i.e. $h = 0$) yields:

$$u_{\text{lim}} = \sqrt{2h_o} \tag{3.32}$$

The limit velocity is a measure of the flow's stagnation enthalpy. It is used to estimate the maximum velocity that can be achieved by expanding a gas close to vacuum conditions. Physically, the flow does not fulfill the isentropic assumptions close to vacuum. Still, in practice the velocity can reach large values close to the limit velocity before yielding the above formulation outside of its range of applicability.

When computing the full-potential flow around streamlined bodies, velocities beyond the limit velocity can be reached in regions of high flow curvature even for subsonic freestream conditions. High flow curvature can happen due to insufficient mesh quality resulting in large dihedral angles, or due to the geometry [40]. A typical region where high flow curvature is reached are the wingtips' trailing edges, which are singular points where the velocity should theoretically be infinite. This singularity is illustrated in Figure 3.5, which shows the resulting magnitude of the velocity modulus in m/s on the surface elements in the vicinity of the wingtip trailing edge. Note how the velocity modulus locally reaches very high velocities at the wingtip trailing edge.

To compute the residual and the Jacobian in the presence of this singularity, a maximum local Mach number squared $M_{\text{max}}^2 \sim O(3.0)$ is set and the density is kept constant from this value on. As presented in [23], other modifications of the density are also possible. Note that only local parts of the boundary are affected by this modification.

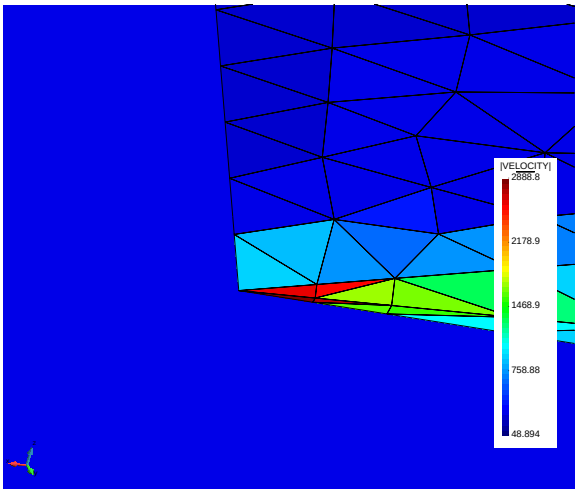

Figure 3.5: The wingtips' trailing edges are singular points where the velocity theoretically is infinite.

3.5 Embedded wake approach

In the analytic solution to Eq. (3.1), there is a jump of the potential across the wake. To support this jump, the method presented in [23, 40] models the wake explicitly within the mesh. The nodes defining the wake surface are duplicated to disconnect the elements across the wake. Without any further treatment, the wake would act as a solid wall. The mass boundary condition (Eq. (3.5)) is then applied by adding the rows corresponding to each pair of duplicated wake nodes and a pressure equality equation (Eq. (3.6)) is added for each pair of nodes. This approach has two major disadvantages. First, it requires modeling the wake explicitly, which can be a rather cumbersome and lengthy process for complex geometries. Second, it hinders the effective use of the solver for aeroelastic optimization, where the wake's position may change due to the structural response and the geometry's evolutionary steps. Even a simple change in the parameters, such as the variation of the angle of attack, would involve remaking the finite-element mesh from the beginning (note that the angle of attack defines the wake direction).

To achieve efficiency, an embedded approach that defines the wake implicitly within the finite-element mesh is proposed. In this approach, the wake geometry is defined as a straight line (in 2D) or surface (in 3D) that extends from the trailing edge into the outlet (see Figures 3.1 and 3.2). In this context, wake elements are all elements intersected (i.e., cut) by the wake. Figure 3.6 shows

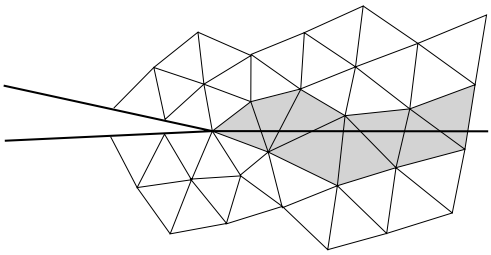

(a) Mesh around the trailing edge.

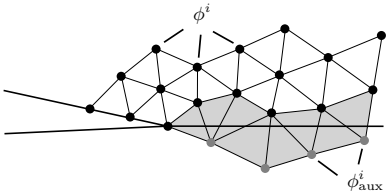

(b) Elements above the wake.

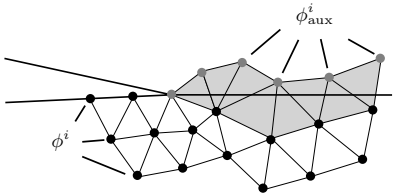

(c) Elements below the wake.

Figure 3.6: Wake elements (in light grey) are disconnected across the wake to support a jump in the potential.

the wake elements behind the trailing edge, which are marked in light grey. In order to support a jump in the potential, wake elements are enriched with auxiliary degrees of freedom and disconnected across the wake so that they are present twice. This is illustrated in Figure 3.6, where the auxiliary degrees of freedom are denoted by ϕ^i_{aux}. Note that the separation between upper and lower mesh presented in Figure 3.6 is only for visualization purposes; in practice, there is only one mesh as shown at the top of Figure 3.6, and the separation is achieved via the auxiliary degrees of freedom.

As shown in Figure 3.6, the degrees of freedom ϕ^i_{u} and ϕ^i_{l} corresponding respectively to the upper and lower wake elements are:

$$\phi^i_{\text{u}} = \begin{cases} \phi^i & \text{if } i^{\text{th}} \text{ node above the wake} \\ \phi^i_{\text{aux}} & \text{if } i^{\text{th}} \text{ node below the wake} \end{cases} \tag{3.33}$$

$$\phi^i_{\text{l}} = \begin{cases} \phi^i_{\text{aux}} & \text{if } i^{\text{th}} \text{ node above the wake} \\ \phi^i & \text{if } i^{\text{th}} \text{ node below the wake} \end{cases} \tag{3.34}$$

The additional equations stemming from these auxiliary degrees of freedom are then used to apply the wake boundary conditions (Eqs. (3.5) and (3.6)).

3.5.1 Wake boundary conditions in two dimensions[cd]

In two dimensions Eqs. (3.5) and (3.6) can be written as a single vector equation:

$$u_{\mathrm{u}}^a - u_{\mathrm{l}}^a = 0 \qquad \text{on } \Omega_W \tag{3.35}$$

where Ω_W is the domain covered by the wake elements. Applying a least squares finite element approach yields the residual energy functional:

$$\Pi = \frac{1}{2}\int_{\Omega_W} (u_{\mathrm{u}}^a - u_{\mathrm{l}}^a)^2 \, d\Omega_W \tag{3.36}$$

Deriving with respect to the degrees of freedom results in the upper and lower wake conditions' residuals:

$$R_u^i = \frac{\partial \Pi}{\partial \phi_{\mathrm{u}}^i} = \sum_{W_{\mathrm{u}}} \int_{\Omega_{W_{\mathrm{u}}}} \frac{\partial N_{\mathrm{u}}^i}{\partial x^a}(u_{\mathrm{u}}^a - u_{\mathrm{l}}^a) \, d\Omega_{W_{\mathrm{u}}} \tag{3.37}$$

$$R_l^i = \frac{\partial \Pi}{\partial \phi_{\mathrm{l}}^i} = \sum_{W_{\mathrm{l}}} \int_{\Omega_{W_{\mathrm{l}}}} \frac{\partial N_{\mathrm{l}}^i}{\partial x^a}(u_{\mathrm{l}}^a - u_{\mathrm{u}}^a) \, d\Omega_{W_{\mathrm{l}}} \tag{3.38}$$

and their corresponding Jacobians:

$$J_{\mathrm{uu}}^{ij} = \frac{\partial R_u^i}{\partial \phi_{\mathrm{u}}^j} = \sum_{W_{\mathrm{u}}} \int_{\Omega_{W_{\mathrm{u}}}} \frac{\partial N_{\mathrm{u}}^i}{\partial x^a} \frac{\partial N_{\mathrm{u}}^j}{\partial x^a} \, d\Omega_{W_{\mathrm{u}}} \tag{3.39}$$

$$J_{\mathrm{ul}}^{ij} = \frac{\partial R_u^i}{\partial \phi_{\mathrm{l}}^j} = -\sum_{W_{\mathrm{u}}} \int_{\Omega_{W_{\mathrm{u}}}} \frac{\partial N_{\mathrm{u}}^i}{\partial x^a} \frac{\partial N_{\mathrm{l}}^j}{\partial x^a} \, d\Omega_{W_{\mathrm{u}}} \tag{3.40}$$

$$J_{\mathrm{lu}}^{ij} = \frac{\partial R_l^i}{\partial \phi_{\mathrm{u}}^j} = -\sum_{W_{\mathrm{l}}} \int_{\Omega_{W_{\mathrm{l}}}} \frac{\partial N_{\mathrm{l}}^i}{\partial x^a} \frac{\partial N_{\mathrm{u}}^j}{\partial x^a} \, d\Omega_{W_{\mathrm{l}}} \tag{3.41}$$

$$J_{\mathrm{ll}}^{ij} = \frac{\partial R_l^i}{\partial \phi_{\mathrm{l}}^j} = \sum_{W_{\mathrm{l}}} \int_{\Omega_{W_{\mathrm{l}}}} \frac{\partial N_{\mathrm{l}}^i}{\partial x^a}, \frac{\partial N_{\mathrm{l}}^j}{\partial x^a} \, d\Omega_{W_{\mathrm{l}}} \tag{3.42}$$

3.5.2 Wake boundary conditions in three dimensions

In the proposed method, first, Eq. (3.5) is linearized by substituting the freestream density ρ_∞ for ρ_{u} and ρ_{l}, which yields:

$$g_{\mathrm{l}} = \hat{\boldsymbol{n}} \cdot (\boldsymbol{u}_{\mathrm{u}} - \boldsymbol{u}_{\mathrm{l}}) = 0 \qquad \text{on } \Omega_W \tag{3.43}$$

where $\hat{\boldsymbol{n}}$ is the normal vector to the wake defined upwards, and Ω_W is the domain covered by the wake elements. Second, approximating the average wake sheet velocity with the freestream velocity allows linearizing Eq. (3.6) as:

$$g_2 = \hat{\boldsymbol{u}}_\infty \cdot (\boldsymbol{u}_\mathrm{u} - \boldsymbol{u}_\mathrm{l}) = 0 \qquad \text{on } \Omega_W \tag{3.44}$$

where $\hat{\boldsymbol{u}}_\infty$ is a unit vector defined as $\hat{\boldsymbol{u}}_\infty = \boldsymbol{u}_\infty / u_\infty$. Eq. (3.44) is a homogeneous linear convection equation for the potential jump across the wake. It states that the potential jump is constant along the freestream sheet streamlines. Applying a least squares finite element approach on Eqs. (3.43) and (3.44), yields the following residual energy functional:

$$\Pi = \frac{1}{2} \int_{\Omega_W} g_1^2 + g_2^2 \; d\Omega_W \tag{3.45}$$

Deriving with respect to the degrees of freedom results in the upper and lower wake conditions' residuals:

$$R_u^i = \frac{\partial \Pi}{\partial \phi_\mathrm{u}^i} = \sum_{W_\mathrm{u}} \int_{\Omega_{W_\mathrm{u}}} \frac{\partial N_\mathrm{u}^i}{\partial x^b} \left(\hat{n}^b g_1 + \hat{u}_\infty^b g_2 \right) \; d\Omega_{W_\mathrm{u}} \tag{3.46}$$

$$R_l^i = \frac{\partial \Pi}{\partial \phi_\mathrm{l}^i} = \sum_{W_\mathrm{l}} \int_{\Omega_{W_\mathrm{l}}} \frac{\partial N_\mathrm{l}^i}{\partial x^b} \left(\hat{n}^b g_1 + \hat{u}_\infty^b g_2 \right) \; d\Omega_{W_\mathrm{l}} \tag{3.47}$$

and their corresponding Jacobians:

$$J_\mathrm{uu}^{ij} = \frac{\partial R_u^i}{\partial \phi_\mathrm{u}^j} = \sum_{W_\mathrm{u}} \int_{\Omega_{W_\mathrm{u}}} \frac{\partial N_\mathrm{u}^i}{\partial x^b} \left(\hat{n}^b \hat{n}^a + \hat{u}_\infty^b \hat{u}_\infty^a \right) \frac{\partial N_\mathrm{u}^j}{\partial x^a} \; d\Omega_{W_\mathrm{u}} \tag{3.48}$$

$$J_\mathrm{ul}^{ij} = \frac{\partial R_u^i}{\partial \phi_\mathrm{l}^j} = -\sum_{W_\mathrm{u}} \int_{\Omega_{W_\mathrm{u}}} \frac{\partial N_\mathrm{u}^i}{\partial x^b} \left(\hat{n}^b \hat{n}^a + \hat{u}_\infty^b \hat{u}_\infty^a \right) \frac{\partial N_\mathrm{l}^j}{\partial x^a} \; d\Omega_{W_\mathrm{u}} \tag{3.49}$$

$$J_\mathrm{lu}^{ij} = \frac{\partial R_l^i}{\partial \phi_\mathrm{u}^j} = -\sum_{W_\mathrm{l}} \int_{\Omega_{W_\mathrm{l}}} \frac{\partial N_\mathrm{l}^i}{\partial x^b} \left(\hat{n}^b \hat{n}^a + \hat{u}_\infty^b \hat{u}_\infty^a \right) \frac{\partial N_\mathrm{u}^j}{\partial x^a} \; d\Omega_{W_\mathrm{l}} \tag{3.50}$$

$$J_\mathrm{ll}^{ij} = \frac{\partial R_l^i}{\partial \phi_\mathrm{l}^j} = \sum_{W_\mathrm{l}} \int_{\Omega_{W_\mathrm{l}}} \frac{\partial N_\mathrm{l}^i}{\partial x^b} \left(\hat{n}^b \hat{n}^a + \hat{u}_\infty^b \hat{u}_\infty^a \right) \frac{\partial N_\mathrm{l}^j}{\partial x^a} \; d\Omega_{W_\mathrm{l}} \tag{3.51}$$

Eqs. (3.46) to (3.51) are assembled in the global equation system together with Eqs. (3.9) and (3.11). The wake surface can be automatically generated by shedding it from the trailing edge in the freestream velocity direction. A robust and accurate capturing of the potential jump across the wake can be achieved by automatically refining the mesh with a metric-based technique [50]. This implicit representation of the wake within the domain saves modeling time and allows to perform aeroelastic optimization in practical applications efficiently.

3.5.3 Treatment of the nodes lying on the wake

The problem

For a given mesh, it can happen that some nodes are lying exactly on the wake. Without further modification, these nodes would have the same potential values from the top and from the bottom of the wake, yielding a zero potential jump and thus a wrong solution.

A solution

In the proposed method, nodes lying on the wake or very close to it are assigned a positive tolerance distance (e.g., $\epsilon = 10^{-6}$ m), such that they are treated as if they were above the wake. This is illustrated in Figure 3.7, where it is shown that assigning a positive distance is equivalent to locally moving the wake downwards. Note that this decision is arbitrary, and the nodes could also be assigned a negative distance (i.e., locally moving the wake upwards).

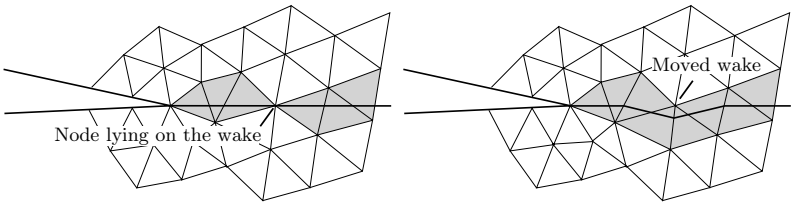

(a) The problem. (b) A solution.

Figure 3.7: Nodes lying on the wake are assigned a tolerance positive distance.

3.5.4 Treatment of the trailing edge nodes

Trailing edge nodes are nodes belonging both to wake elements and to the body. Because these nodes belong to the body, the slip boundary condition (Eq. (3.4) with $q = 0$) is applied instead of the wake boundary conditions. This means that the auxiliary degrees of freedom corresponding to the trailing edge nodes are only used to disconnect the elements above and below the trailing edge and that they implement the conservation of mass equation (Eq. (3.9)) instead of the wake boundary conditions (Eqs. (3.37) and (3.38) in 2D or Eqs. (3.46) and (3.47) in 3D). Thus, these auxiliary degrees of freedom are effectively treated as a normal velocity potential degree of freedom belonging to the elements below the trailing edge. This is illustrated for two dimensions in Figure 3.6, where the trailing edge is marked in grey for the elements below the wake, indicating that it corresponds to the auxiliary degree of freedom.

In two dimensions, there is only one wake element containing the trailing edge node.

Note that this is an exception to the treatment introduced in the previous section. For sharp trailing edges, trailing edge nodes are another example of nodes lying on the wake. Note that in two dimensions, there is only one trailing edge node per airfoil. Moving these nodes upwards would result in cutting all wake elements under the wake that are in touch with the trailing edge, which yields inaccurate results in some cases.

3.5.5 Treatment of small-cut elements

The problem

The first version of the proposed embedded wake approach was first published in [44]. In this first version, wake elements were divided into upper and lower parts, and the integrals stemming from the wake boundary conditions (Eqs. (3.37) to (3.42) and (3.46) to (3.51)) where only evaluated for the upper and lower domains. The shape functions' derivatives were not recomputed, so the only difference (compared to not cutting the elements) was that the integrands were integrated over a smaller domain. This approach yielded ill-conditioned systems when nodes were lying on or close to the wake due to the so called small-cut problem. The small-cut problem is illustrated in Figure 3.8, where the elements below the wake are presented as an example and the small cut wake elements are marked in red. Note that the small-cut elements have a very small area, which when performing the integrals in Eqs. (3.37) to (3.42) and (3.46) to (3.51), yields contributions to the Jacobian and the residual that are very close to zero. These small entries in the Jacobian is what causes the system to be ill-conditioned:

$$J^{ij}_{\mathrm{uu}} = \frac{\partial R^i_u}{\partial \phi^j_{\mathrm{u}}} = \sum_{W_{\mathrm{u}}} \int_{\Omega_{W_{\mathrm{u}}}} \frac{\partial N^i_{\mathrm{u}}}{\partial x^a} \frac{\partial N^j_{\mathrm{u}}}{\partial x^a} \, d\Omega_{W_{\mathrm{u}}} \approx 0 \tag{3.52}$$

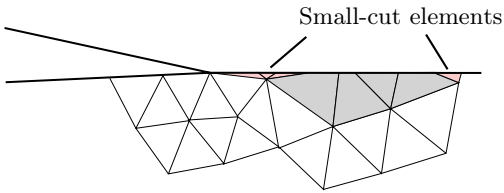

Figure 3.8: Nodes lying close to the wake lead to ill-conditioned systems.

Recomputing the shape functions' derivatives for the small cuts does not solve this problem. The shape functions' derivatives are proportional to the inverse to the element area (or volume in 3D), which results in very large entries in the Jacobian. These large entries also yield ill-conditioned systems:

$$\frac{\partial N^i}{\partial x^a} \propto \frac{1}{A} \gg 1 \tag{3.53}$$

where A is the element area in 2D or volume in 3D.

A solution

To solve the small-cut problem, a full integration approach has been developed. This approach consists on integrating Eqs. (3.37) to (3.42) and (3.46) to (3.51) over the full element. The proposed full integration approach is a very simple yet effective way to maintain similar system condition numbers as in a body fitted method, making the embedded wake approach very robust.

3.6 Implementation in KRATOS Multi-Physics

The potential transonic solver using the proposed embedded wake approach is implemented in KRATOS Multiphysics [52]. Kratos is an open-source finite-element framework for building parallel, multi-disciplinary simulation software [53, 51]. It aims at modularity, extensibility, and high performance. Kratos is available under a BSD license.

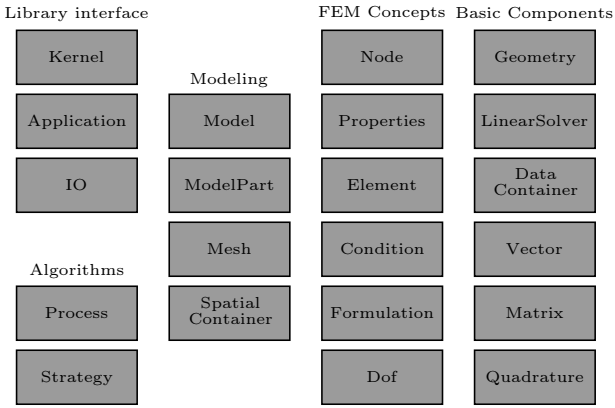

Figure 3.9: Main classes defined in Kratos [51].

3.6.1 Kratos structure

Kratos uses an objected-oriented structure to solve problems with the finite-element method. This structure allows splitting the problem into several objects and defining their interfaces [53]. Figure 3.9 shows the main classes of Kratos. Kratos multi-layer design is illustrated in Figure 3.10. This approach reduces dependencies inside Kratos because an object can only interface with another object in the same layer or a layer below. This allows the developers to only work in specific layers without knowing the whole Kratos. These

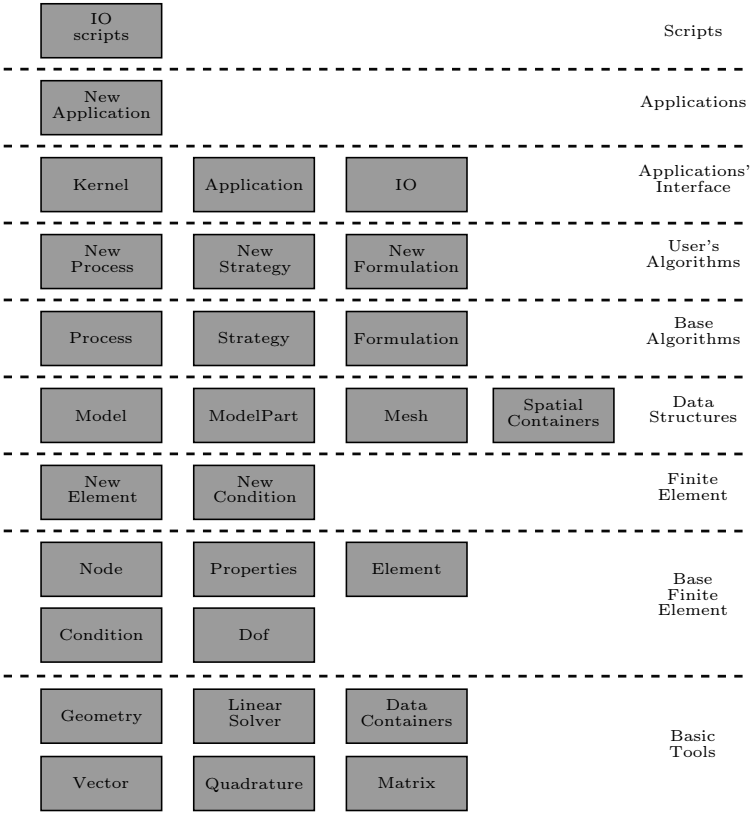

Figure 3.10: Kratos is designed in a multi-layer approach [51].

layers also reflect the working space of developers with different fields of expertise.

To increase performance and efficiency, Kratos uses a kernel and application approach, which is illustrated in Figure 3.11. The kernel is the framework that manages the whole Kratos. It does not contain physics. Kratos data structure is defined in the kernel. The kernel initializes Kratos' different parts, it provides the necessary interface to communicate with the applications, and it contains the IO scripts. The kernel can also synchronize the variables numbering between different applications. The applications contain the physics. For instance, the variables, elements, and conditions are registered in the applications. This separation between kernel and applications also avoids recompiling the whole code when only one application is changed.

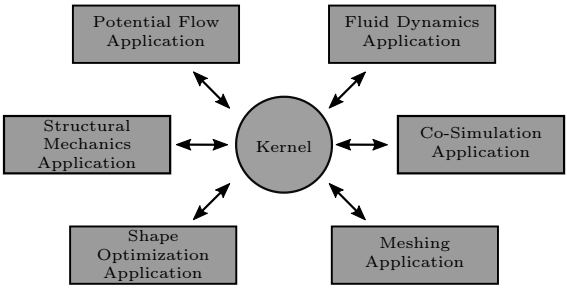

Figure 3.11: Kratos uses a kernel and application approach.

3.6.2 Potential flow application

In total, three potential solvers corresponding to three different fidelity levels have been implemented: a linear incompressible, a nonlinear compressible subsonic, and a nonlinear compressible transonic potential solver. The solvers are implemented in the `Potential Flow Application`. The incompressible solver uses a linear strategy and the `Incompressible Potential Flow Element`, which implements the residual and Jacobian from Eq. (3.15) and Eq. (3.16). The compressible subsonic and transonic solvers use Newton Raphson strategy, and the `Compressible Potential Flow Element` and `Transonic Potential Flow Element` respectively.

The `Compressible Potential Flow Element` implements the residual and Jacobian from Eqs. (3.9) and (3.11) without the density modification introduced with the artificial compressibility method. Thus, this element's range of application is limited to subsonic (elliptic) flow. To be able to compute the residual and the Jacobian in localized pockets of supersonic flow, the isentropic density relation (Eq. (2.41)) is clamped to a user-defined limit

Mach number $M_{\max} \sim O(0.98)$. This clamping approach introduces an error in supersonic flow regions but is very effective in maintaining the elliptic character of the problem [40]. Still, the solution is very accurate as long as these pockets of supersonic flow are localized in small regions (e.g., in the wingtip trailing edges).

The `Transonic Potential Flow Element` implements the residual and Jacobian from Eqs. (3.23) and (3.24) with the density modification introduced with the artificial compressibility method (Eqs. (3.19) and (3.20)).

The three elements are templated to work in both two and three dimensions. All elements implement the proposed embedded wake approach and the wake boundary conditions described in Sections 3.5.1 and 3.5.2. A `Define Wake Process` has been implemented to identify the wake elements (i.e. elements cut by the wake), and the elements below the trailing edge requiring the special treatment described in Section 3.5.4. Two different approaches to define the wake in 3D have been implemented. The first one imports the wake model as an Standard Triangle Language (STL) file format that has to be previously generated from a CAD model. The import is done at python level using numpy-stl. The second one automatically generates the wake triangular mesh. This is implemented in parallel using open multi-processing (OpenMP) at C++ level for performance.

An `Apply Far Field Process` has been implemented to apply the boundary conditions (Eqs. (3.3) to (3.6)). This process fixes the potential value of the nodes within the inlet boundary, it assigns the freestream velocity and density values to the conditions within the outlet boundary, and it assigns the rest of the freestream conditions and user defined parameters to the `Fluid Root Modelpart Process Info`.

Chapter 4

Validation, Verification and Numerical Studies

This chapter presents the validation and verification of the embedded wake approach introduced in Chapter 3. In total, five models are investigated: the NACA 0012 airfoil, the Korn supercritical airfoil, a rectangular wing with NACA 0012 airfoil section, the Onera M6 wing, and NASA CRM. To evaluate the proposed approach, lift, drag, pitching moment, and pressure coefficients are compared with reference data from other codes and wind tunnel tests.

Sections 4.1, 4.3 and 4.4 present the validation and verification cases over the NACA 0012 airfoil. A set of mesh refinement studies and a domain size study are performed to establish confidence with the numerical results. Furthermore, the embedded wake approach is verified in the incompressible, compressible subsonic, and compressible transonic flight regimes. Section 4.2 presents the verification of the compressible subsonic and transonic elemental sensitivities.

In Section 4.5 the transonic solver using the Korn supercritical airfoil is verified. Section 4.6 includes a drag divergence study comparing the NACA 0012 with the Korn airfoil, the verification of the resulting critical Mach number, and a multi-fidelity analysis comparing the incompressible, compressible subsonic, and transonic solvers. Section 4.7 presents the verification of the three-dimensional incompressible solver using the rectangular wing, and Section 4.8 provides the three-dimensional Onera M6 wing transonic validation and verification case. Finally, the results on a full aircraft configuration are presented in Section 4.9.

Salome is used to generate the geometries and the meshes [54]. Salome is an open-source software providing a generic pre-processing platform for numerical simulation. A significant advantage of using an embedded wake approach is that the wake does not need to be explicitly modeled in the domain, substantially reducing the modeling time. In the numerical studies presented here, square and cubic domains are considered, where the inlet, outlet, and walls' dimensions are equal. Triangular and tetrahedral meshes are created using the NETGEN algorithm [55]. The main parameters defining the meshes are the maximum element size, the minimum element size, and the growth rate, which is the maximum ratio by which two adjacent elements can differ (e.g. a growth rate of 0.1 means that the linear dimensions of two adjacent elements can differ by 10%).

Salome has a python interface that allows to easily modify the model parameters, such as mesh or domain sizes. In order to convert Salome's output mesh format into Kratos' input mesh format, Kratos Salome Plugin developed by Philipp Bucher is employed [56]. Using these components, a tool to automatically perform parameter studies has been developed.

4.1 Incompressible flow around NACA 0012 airfoil[a]

In this section, a mesh refinement study and a domain size study are presented for a NACA 0012 airfoil at an angle of attack of 5° using the incompressible potential flow element. Since the incompressible element implements the Laplace equation, the results can be compared with the solution provided by XFOIL [57]. XFOIL is a panel solver developed by Professor Mark Drela at the Massachusetts Institute of Technology. At the end of the section, the resulting lift coefficient is compared with wind tunnel test data for different angles of attack.

NACA 0012 airfoil's geometry was selected due to the large number of reference data available in the literature. The airfoil's shape is described by:

$$z = \pm 0.6(0.2969\sqrt{x} - 0.1260x - 0.3516x^2 + 0.2843x^3 - 0.1015x^4) \quad (4.1)$$

where z is the half thickness, and x the position along the chord ($x \in [0, 1]$). This description results in a blunt trailing edge. For the purposes of this study, the last coefficient was slightly modified to achieve a sharp trailing edge:

$$z = \pm 0.6(0.2969\sqrt{x} - 0.1260x - 0.3516x^2 + 0.2843x^3 - 0.1036x^4) \quad (4.2)$$

This modification is specified by the AIAA Aerodynamic Design Optimization Discussion Group [58]. The airfoil was generated using Salome's parametric curve generator, which allows specifying a parametric equation for each coordinate.

4.1.1 Mesh refinement study of the reference solution

First, to ensure that the reference solution is mesh independent, a refinement study is performed using XFOIL. The coordinates defining the panels were computed with Airfoil Tools using cosine spacing and a closed trailing edge. Figures 4.1 and 4.2 show the convergence of the lift coefficient and its relative error for an increasing number of panels. The lift coefficient relative error is expressed as a percentage using:

$$\delta_{c_l} = \frac{|c_l - c_{l\text{ref}}|}{|c_{l\text{ref}}|} \cdot 100\% \tag{4.3}$$

where the reference lift coefficient $c_{l\text{ref}}$ is the value obtained for 200 panels ($c_{l\text{ref}} = 0.603$). Since the lift coefficients obtained with 180 and 200 panels are equal up to the precision provided by XFOIL, the solution is considered to be converged. XFOIL rounds the solution to the fourth decimal, which for this case yields the following precision expressed as relative error:

$$\delta_{c_l} = \frac{10^{-4}}{0.603} \cdot 100 = 0.017\% \tag{4.4}$$

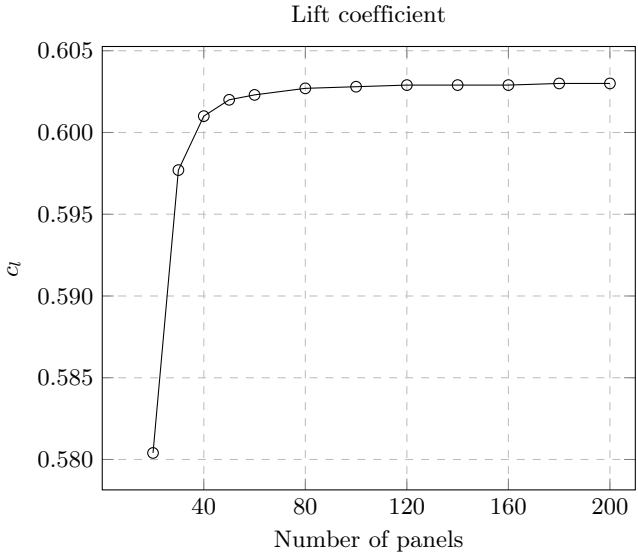

Figure 4.1: Mesh refinement study using XFOIL ($\alpha = 5.0°$).

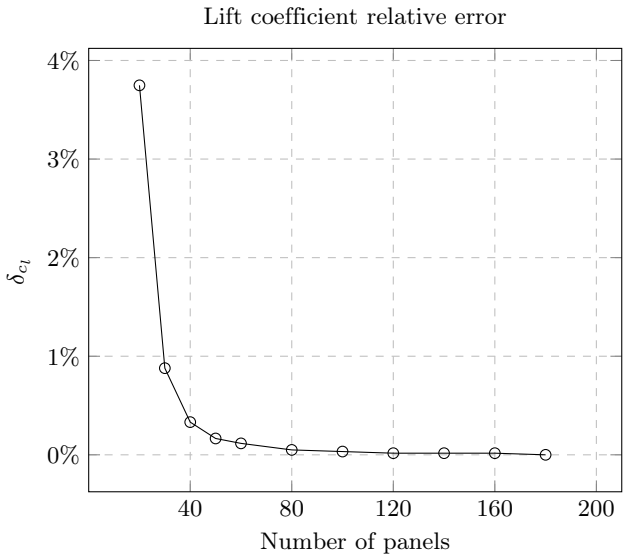

Figure 4.2: Mesh refinement study using XFOIL ($\alpha = 5.0°$).

4.1.2 Mesh refinement study

In the following, the solution provided by XFOIL for 200 panels is used as a reference. In order to verify the proposed embedded wake approach, the convergence of the lift and pitching moment coefficients is investigated. In total, six meshes with a domain size of 100 m and a chord length of 1 m are considered. Figure 4.3 shows the domain's far-field mesh and two meshes in the vicinity of the airfoil for different mesh refinements, where the minimum element size is denoted by h. Note the substantial benefit of using an embedded wake approach, where the wake does not need to be explicitly represented by the mesh. The meshes are refined towards the leading and trailing edges, where the solution's gradients are the largest. This refinement also allows to accurately capture the geometry at the leading edge, where the radius of curvature is the smallest. The airfoil is discretized using a geometric progression where the common ratio is set to 1.01. The domain's boundary is discretized using a uniform distribution with an element size of 2 m ($1/50^{\text{th}}$ of the domain size). The domain's maximum element size matches the boundary's element size, and the mesh growth rate is set to 0.05 to ensure a smooth element size transition.

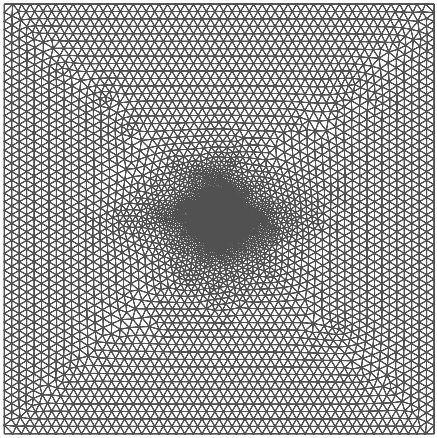

(a) Domain's far-field mesh.

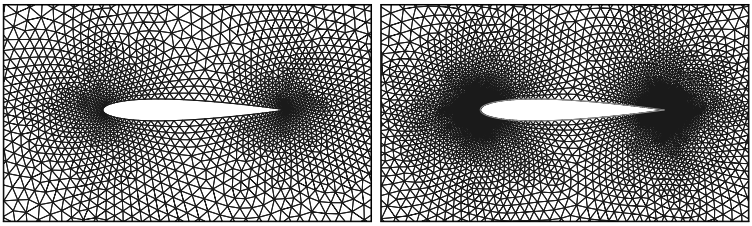

(b) Mesh around the airfoil for $h = 1 \times 10^{-2}$ m (left) and $h = 1 \times 10^{-3}$ m (right).

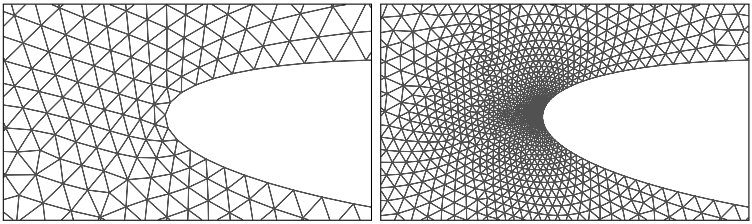

(c) Mesh around the leading edge for $h = 1 \times 10^{-2}$ m (left) and $h = 1 \times 10^{-3}$ m (right).

Figure 4.3: Meshes around NACA 0012.

In the following, the convergence of lift and pitching moment coefficients and their relative errors for a decreasing minimum element size is examined. The reference point to compute the moment is the leading edge. The pitching moment coefficient's relative error is expressed as a percentage in the same way as for the lift using:

$$\delta_{c_m} = \frac{|c_m - c_{m\text{ref}}|}{|c_{m\text{ref}}|} \cdot 100\% \tag{4.5}$$

where the reference moment coefficient $c_{m\text{ref}}$ is the value obtained with XFOIL for 200 panels ($c_{m\text{ref}} = -0.1570$). The moment coefficient is computed using a near-field analysis, whereas the lift coefficient is computed using three approaches:

1. Near-field analysis, integrating the pressure force over the airfoil:

$$c_l = \frac{1}{c} \oint_{\text{airfoil}} C_p \; \hat{\boldsymbol{n}} \cdot \hat{\boldsymbol{y}} \; ds \tag{4.6}$$

2. Wake potential jump analysis, using Kutta-Joukowski theorem:

$$c_l = \frac{2\Delta\phi}{u_\infty c} \tag{4.7}$$

3. Far-field analysis, using the integral momentum theorem:

$$c_l = -\frac{1}{c} \oint_{\text{far-field}} \left[C_p \; \hat{\boldsymbol{n}} - \frac{\rho(\boldsymbol{u} \cdot \hat{\boldsymbol{n}})(\boldsymbol{u} - \boldsymbol{u}_\infty)}{\frac{1}{2}\rho_\infty u_\infty^2} \right] \cdot \hat{\boldsymbol{y}} \; ds \tag{4.8}$$

Figures 4.4 and 4.5 present the lift and pitching moment coefficients and their relative errors over the minimum element size. Figure 4.4 shows that the solution accurately matches the reference. For a minimum element size smaller than 10^{-2}, the lift and moment relative errors are below 2% and 4%, respectively. However, the solution does not converge towards the reference solution. The smallest lift relative error is around 0.44%, larger than the 0.017% precision provided by XFOIL. A contribution to this error comes from the influence of the far-field boundary conditions, which are applied at a finite distance from the airfoil. This approximation is a major disadvantage of the grid methods compared to the singularity methods, in which Green's functions automatically satisfy the far-field boundary conditions. Nevertheless, this error can be estimated via domain size studies, as presented in the next section. For a quantitative comparison, the lift and moment coefficient values obtained for the different mesh refinements are presented in Table 4.1, where the values are rounded to the sixth decimal to show the difference between the force analysis approaches. To verify that the embedded wake approach delivers robust results for an arbitrary angle of attack, this mesh refinement study was repeated for eight additional angles of attack. The results can be found in Appendix C.

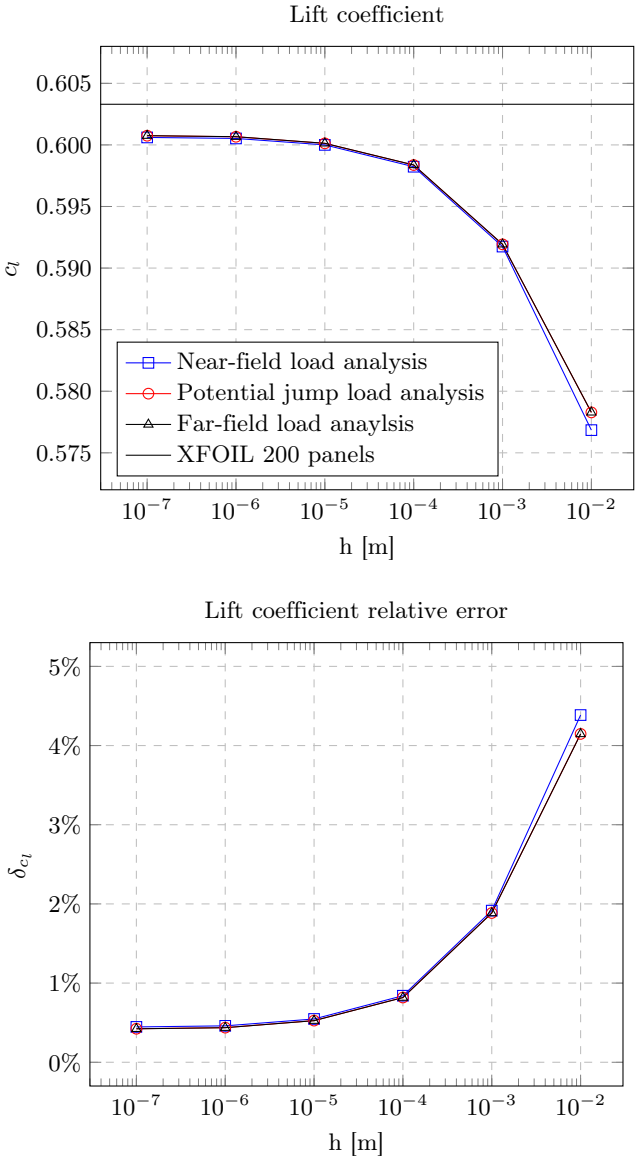

Figure 4.4: NACA 0012 mesh refinement study ($\alpha = 5.0°$).

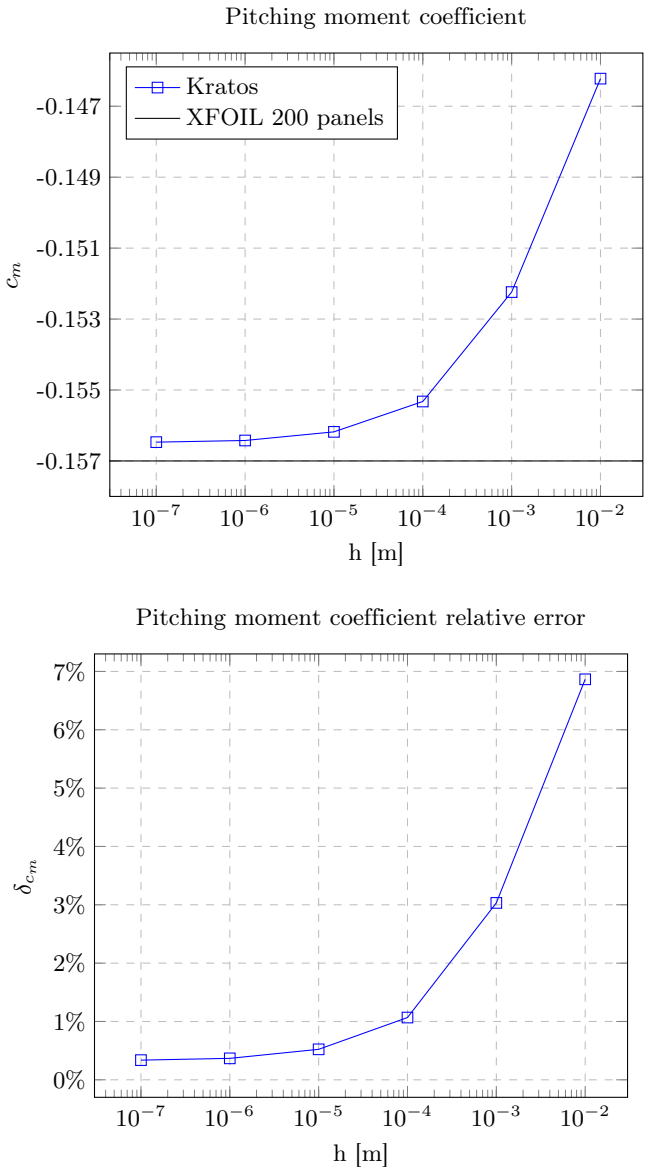

Figure 4.5: NACA 0012 mesh refinement study ($\alpha = 5.0°$).

	c_l [-]			c_m [-]
h [m]	Near-field	Potential jump	Far-field	Near-field
10^{-2}	0.576844	0.578281	0.578285	-0.146222
10^{-3}	0.591746	0.591927	0.591931	-0.152239
10^{-4}	0.598230	0.598367	0.598371	-0.155324
10^{-5}	0.600002	0.600126	0.600131	-0.156180
10^{-6}	0.600525	0.600662	0.600667	-0.156423
10^{-7}	0.600607	0.600746	0.600751	-0.156470
Reference	0.6030	0.6030	0.6030	-0.1570

Table 4.1: NACA 0012 mesh refinement study ($\alpha = 5.0°$).

4.1.3 Pressure coefficient distribution verification

Figure 4.6 compares the resulting and reference pressure coefficient distributions along the upper and lower airfoil's surfaces for the different mesh refinements. The pressure coefficient is computed using the incompressible Bernoulli equation:

$$C_p \equiv \frac{p - p_\infty}{\frac{1}{2}\rho u_\infty^2} = 1 - \frac{u^2}{u_\infty^2} \tag{4.9}$$

where the velocity is evaluated at the edges constituting the discretized airfoil. The velocity at the edges is equal to the velocity at the edges' parent elements because linear shape functions are considered.

Figure 4.6 shows that the resulting pressure coefficient distribution is that of a typical subsonic solution, where the flow expands around the leading edge and then slowly starts to compress. Note that despite using an embedded wake approach, the stagnation point and the equality of pressures at the trailing edge are accurately captured. The largest disagreements with the reference solution occur for $h = 10^{-2}$, at the suction peak point. The smaller the mesh size, the better the pressure gradients at the leading and trailing edges are resolved. The solution matches the reference very accurately, such that it is difficult to observe the difference by the naked eye.

4.1.4 Domain size study

In order to estimate the error introduced by applying the far-field boundary conditions at a finite distance from the airfoil, a domain size study is performed.

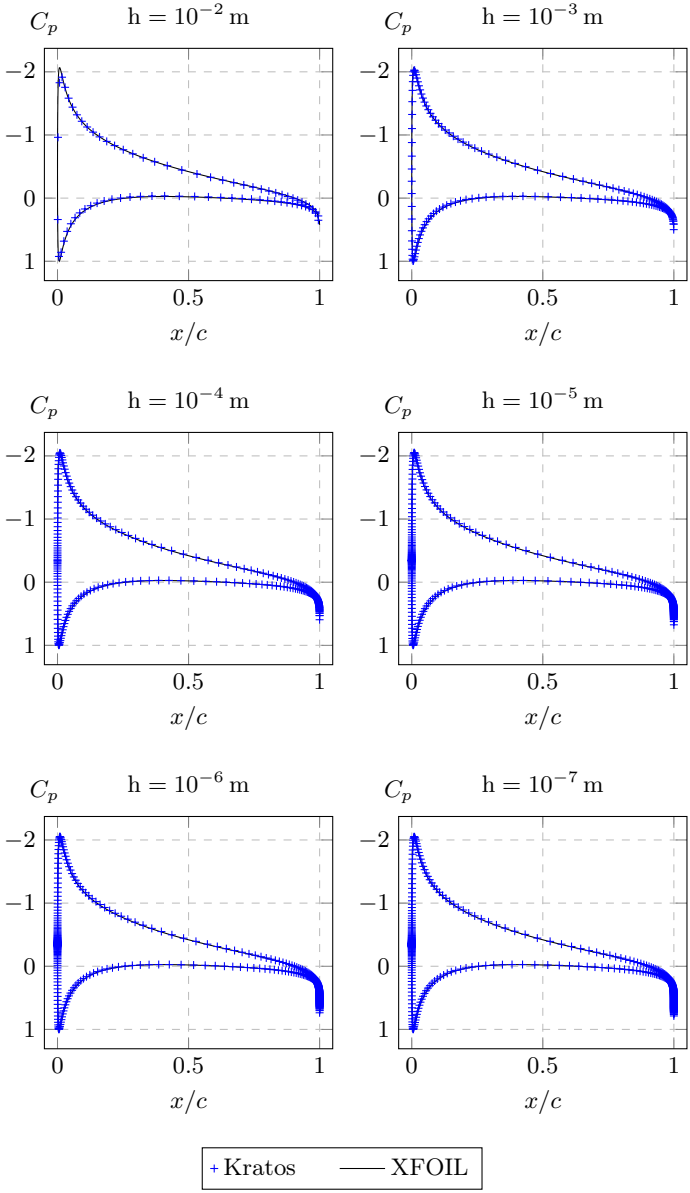

Figure 4.6: Pressure coefficient distribution for different mesh refinements.

In total, six domain sizes are investigated. The minimum element size is $h = 1 \times 10^{-6}$ m, and the ratio between the domain's size and the maximum element size is 50. The mesh growth rate is set to 0.05. Figure 4.7 shows the value of the lift coefficient relative error over the domain sizes. Note that all the values are below 0.5%. For a domain size larger than 1×10^3 m the relative error varies less than 0.01%, and the solution can be considered to be converged. The difference between the relative error at $L = 1 \times 10^3$ m and the converged value yields an estimation of the error due to applying the far-field boundary conditions at a finite distance from the airfoil, which for $L = 1 \times 10^3$ m is around 0.3%. However, the solution still does not converge towards the reference. The smallest lift relative error is around 0.17%, which is still larger than the 0.017% precision provided by XFOIL.

One possible explanation for this error may be the difference in the wake's geometry definition between both methods. In two dimensions, panel methods do not require an explicit definition of the wake's geometry since it is sufficient

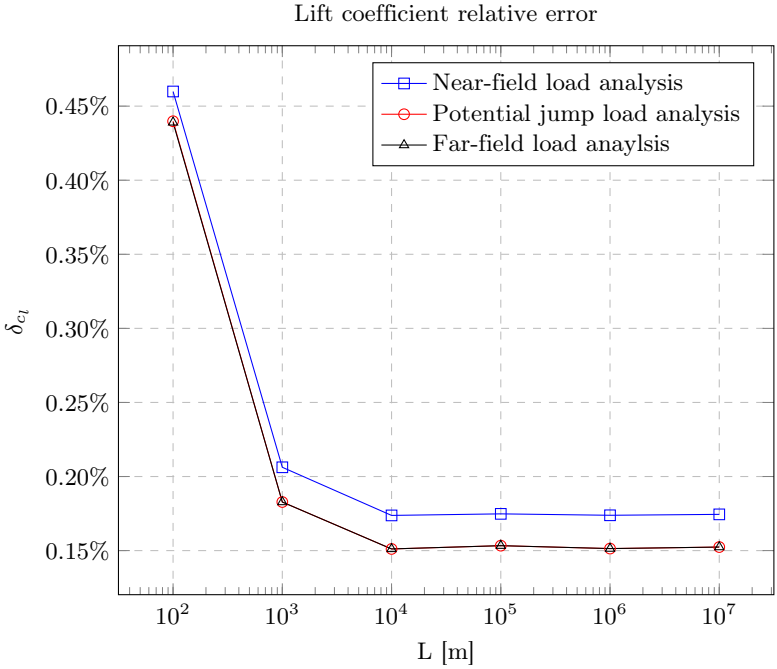

Figure 4.7: NACA 0012 domain size study ($\alpha = 5.0°$, $h = 1 \times 10^{-6}$ m).

to apply the Kutta condition at the trailing edge, and the wake's location is a product of the solution. However, finite element potential solvers require the modeling of the wake to specify the potential jump location. In the proposed approach, the wake is assumed to be straight in the direction of the freestream velocity. This assumption is relaxed by allowing mass flow through the wake. Still, it has been shown that the wake's geometry affects the solution [47].

A further possible contribution to the small disagreement between the solutions is the lack of refinement in the airfoil's middle and the far-field, where the mesh size is kept constant. Finally, another contribution could be that the modification used in Airfoil Tools to close the trailing edge is perhaps different than the one presented in Section 4.1, and so, the solution and the reference might be related to slightly different geometries. In any case, bearing in mind that the comparison involves two different software implementing different methods, the solution obtained with the embedded wake approach is considered to accurately match the reference within an error of $\sim O(10^{-1}\%)$.

Note that each force analysis approach yields different results. In order to assess this difference, the lift coefficient values are presented in Table 4.2, where the values are rounded to the 11^{th} decimal to capture the difference for the whole domain size range. In order to analyze this difference in more detail, the relative difference between each force analysis approach is computed as

$$\Delta c_l = \frac{|c_{l1} - c_{l2}|}{|c_{l\text{ref}}|} \cdot 100\% \tag{4.10}$$

where c_{l1} and c_{l2} are the lift coefficients corresponding to two different approaches. The results are presented in Table 4.3. The results obtained with the potential jump and the far-field approaches are closer to each other

Domain size	c_l [-]		
L [m]	Near-field	Potential jump	Far-field
10^2	0.60052549154	0.60066222393	0.60066679183
10^3	0.60205576097	0.60219717746	0.60219722243
10^4	0.60225177462	0.60238828036	0.60238828087
10^5	0.60224545055	0.60237499288	0.60237499287
10^6	0.60225121829	0.60238680718	0.60238680722
10^7	0.60224749338	0.60238062378	0.60238062386

Table 4.2: NACA 0012 domain size study ($\alpha = 5°$, $\text{h} = 1 \times 10^{-6}$ m).

Domain size	Δc_l [%]		
L [m]	Near-field vs. Potential jump	Near-field vs. Far-field	Potential jump vs. Far-field
10^2	$2.27 \cdot 10^{-2}$	$2.34 \cdot 10^{-2}$	$7.57 \cdot 10^{-4}$
10^3	$2.34 \cdot 10^{-2}$	$2.34 \cdot 10^{-2}$	$7.45 \cdot 10^{-6}$
10^4	$2.26 \cdot 10^{-2}$	$2.26 \cdot 10^{-2}$	$8.45 \cdot 10^{-8}$
10^5	$2.15 \cdot 10^{-2}$	$2.15 \cdot 10^{-2}$	$1.82 \cdot 10^{-9}$
10^6	$2.25 \cdot 10^{-2}$	$2.25 \cdot 10^{-2}$	$5.47 \cdot 10^{-9}$
10^7	$2.21 \cdot 10^{-2}$	$2.21 \cdot 10^{-2}$	$1.39 \cdot 10^{-8}$

Table 4.3: Relative difference between the force analysis approaches.

($< O(10^{-3}\%)$ error) than to the ones obtained with the near-field approach ($\sim O(10^{-2}\%)$ error). This result is to be expected since the potential jump approach is an alternative far-field analysis. In fact, the difference between the potential jump and the far-field results is smaller than the precision provided by XFOIL and is close to single precision for a domain size larger than 1×10^4 m. Note that here a relative error of $O(10^{-8}\%)$ is equivalent to a difference in the 9^{th} decimal. The difference between the near-field and the other approaches is of the same order of magnitude as the precision provided by XFOIL and may be related to the discretization error introduced in the areas that are not refined.

4.1.5 Validation with wind tunnel data

To validate the proposed embedded wake approach, the lift and pressure coefficients are compared with wind tunnel data (WTD) for different angles of attack in Figures 4.8 and 4.9. The wind tunnel data is taken from [59–61]. There are some differences between the experimental data, especially near stall where the experiments are not two-dimensional anymore. Thus, since two-dimensional experiments are very difficult to achieve, especially at high angles of attack approaching stall, the experimental data should be interpreted carefully. The experimental data presented in [60] is likely more two-dimensional and thus is used for the validation of surface pressures. Figure 4.8 also displays XFOIL's solution as an incompressible potential flow numerical reference. The lift polar shows that the lift coefficient obtained with the incompressible potential flow solvers is proportional to the angle of attack. Numerical and experimental results present an accurate agreement for smalls angles of attack, where the flow is still attached. As the angle of attack increases, the disagreement between data grows because viscous effects are

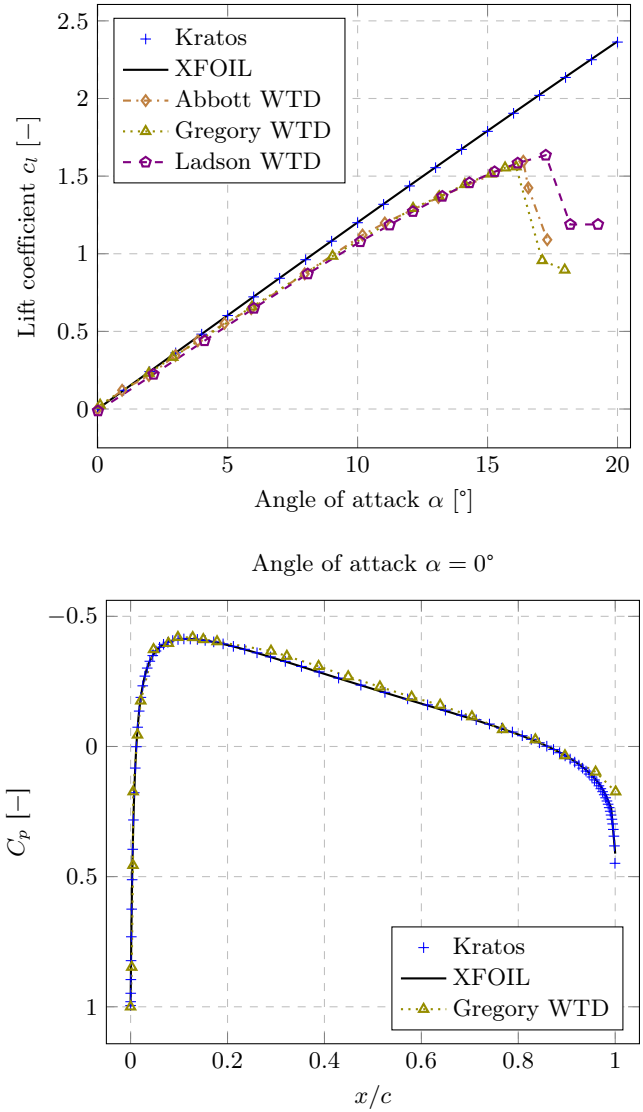

Figure 4.8: Lift polar (h = 1×10^{-3} m, L = 1×10^{2} m).

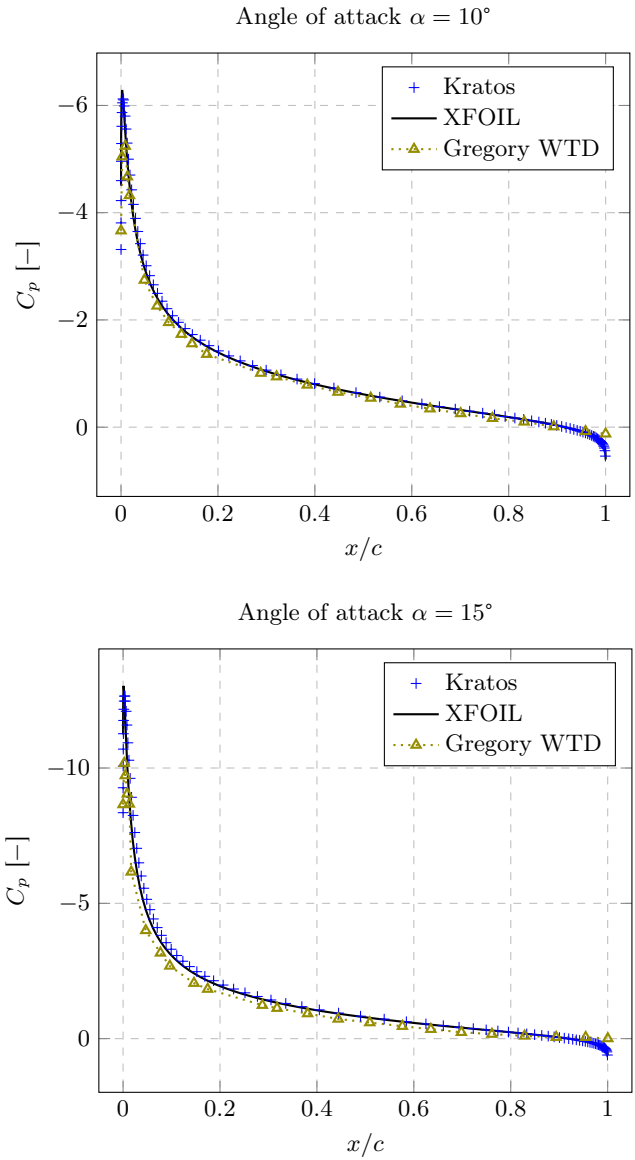

Figure 4.9: Pressure coefficient distribution validation.

neglected in the proposed solver. Thus, the potential flow solver cannot capture the separation of the boundary layer, causing stall. The pressure coefficient distributions show the same behavior; an accurate agreement is achieved for $\alpha = 0°$, whereas for $\alpha = 10°$ and $\alpha = 15°$ the pressure is underestimated in the suction peak. This pressure underestimation explains the lift overestimation observed in the lift polar. To account for viscous effects, instead of setting the mass flow at the airfoil's surface to zero, it can be set to a known transpiration value (e.g., to model displacement or wall transpiration effects). Methods to couple potential flow and boundary layers are presented in [23, 48].

4.2 Verification of the compressible subsonic and transonic elemental sensitivities

To verify that the Jacobian of the compressible subsonic and transonic elements is correctly implemented, the method proposed by Nishida and Drela is applied [62]. This method compares the Jacobian values obtained by evaluating the implemented analytical formulas with the values obtained by computing the Jacobian using finite differences.

This verification has been carried out both in 2D and 3D using triangular and tetrahedral elements like the ones depicted in Figure 4.10. The first step of this method is to assume a random nodal potential field ϕ^j. With this field, the original analytical value of the Jacobian can be evaluated:

$$(J^{ij})_{\text{original}} = \left(\frac{\partial R^i}{\partial \phi^j}\right)_{\text{original}} \tag{4.11}$$

The second step is to perturb the assumed potential field with a small value $\Delta\phi^j$:

$$\phi^j_{\text{perturbed}} = \phi^j + \Delta\phi^j \tag{4.12}$$

Third, the Jacobian can be computed using finite differences:

$$\left(\frac{\partial R^i}{\partial \phi^j}\right)_{\text{f.d.}} = \frac{(R^i)_{\text{perturbed}} - (R^i)_{\text{original}}}{(\phi^j)_{\text{perturbed}} - (\phi^j)_{\text{original}}} \tag{4.13}$$

Finally, the average analytic Jacobian is:

$$\left(\frac{\partial R^i}{\partial \phi^j}\right)_{\text{average}} = \frac{1}{2}\left\{\left(\frac{\partial R^i}{\partial \phi^j}\right)_{\text{original}} + \left(\frac{\partial R^i}{\partial \phi^j}\right)_{\text{perturbed}}\right\} \tag{4.14}$$

Comparing the results obtained with Eqs. (4.13) and (4.14) allows establishing whether the Jacobian is correctly implemented. This method has been

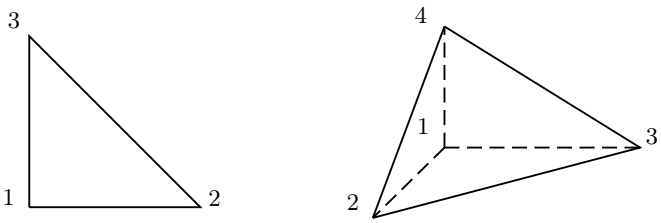

Figure 4.10: Triangular and tetrahedral elements and local nodal ids.

implemented as a unit test in Kratos. The results match up to a tolerance of 10^{-10} with a perturbation step of 10^{-3}. This small error means that the Jacobian accurately matches the derivative of the implemented residual. Note that it can be that the residual is implemented incorrectly, but the Jacobian correctly represents its derivative. In this case, the test presented in this section would pass, and the solver would converge quadratically but to the wrong solution. In order to check whether the solver converges towards the right solution, the following sections present the comparison between the obtained results and the reference data.

4.3 Compressible subsonic flow around NACA 0012 airfoil

4.3.1 Mesh refinement study

This section presents the verification of the embedded wake approach for compressible subcritical flow. In order to do so, a mesh refinement is performed for the test cases indicated in Table 4.4. The first case is lifting, and the second one is non-lifting. The solution is compared to the finite-difference reference solution from Lock [63]. Lock uses Sells' method to solve subsonic compressible flows mapping the region external to the airfoil conformally into the interior of a unit circle [64]. It is reported that this method yields

Case	Airfoil	α	M_∞	Chord length
(1)	NACA0012	2.0	0.63	1.0089
(2)	NACA0012	0.0	0.72	1.0089

Table 4.4: Subsonic compressible test cases.

an accuracy of the order of 1% of the maximum perturbation velocity. The method is limited to a maximum local Mach number of about 0.98.

Lock does not use the modification introduced in Eq. (4.2) to close the trailing edge. Instead, the original NACA0012 airfoil (Eq. (4.1)) is extended to $x = 1.0089$. For the purposes of this study, the same approach is used in this section. For these examples, the critical Mach number is set to 0.99. Figures 4.11 and 4.12 show the convergence of the lift coefficient for both test cases, its relative error for the lifting case, and its absolute error for the non-lifting case. The convergence characteristics are close to the ones observed for the incompressible case. The three force analysis approaches yield very similar results. The relative error converges towards a value less than 1% in the first case. The absolute error does not converge for the second case. Note that the value corresponding to h=10^{-7} is slightly off. Since this case is symmetric, the resulting lift coefficient is very sensitive to mesh asymmetries. Still, the absolute error of the three smaller meshes is smaller than 10^{-4}, which is deemed very accurate.

4.3.2 Pressure coefficient distribution verification

The pressure coefficient distribution for the different mesh refinements is compared to Lock's solution in Figures 4.13 and 4.14. The critical pressure coefficient is indicated with a dashed line as reference. The critical value is the pressure coefficient corresponding to a local Mach number of 1.0. The pressure coefficient is computed using Bernoulli's compressible equation:

$$C_p \equiv \frac{p - p_\infty}{\frac{1}{2}\rho u_\infty^2} = \frac{2}{\gamma M_\infty^2}\left(\frac{p}{p_\infty} - 1\right) \tag{4.15}$$

$$= \frac{2}{\gamma M_\infty^2}\left\{\left[\frac{1 + \frac{\gamma-1}{2}M_\infty^2}{1 + \frac{\gamma-1}{2}M^2}\right]^{\frac{\gamma}{\gamma-1}} - 1\right\} \tag{4.16}$$

$$= \frac{2}{\gamma M_\infty^2}\left\{\left[1 + \frac{\gamma-1}{2}M_\infty^2\left(1 - \frac{u^2}{u_\infty^2}\right)\right]^{\frac{\gamma}{\gamma-1}} - 1\right\} \tag{4.17}$$

Note that the pressure is under the critical pressure over the whole airfoil, meaning that both cases are subcritical. As for the incompressible case, an accurate matching with the data is achieved. The smaller refinements capture the pressure gradients more precisely. This is particularly visible in the trailing edge, where the rear stagnation point consequence of Kutta's condition is resolved better the smaller the minimum element size.

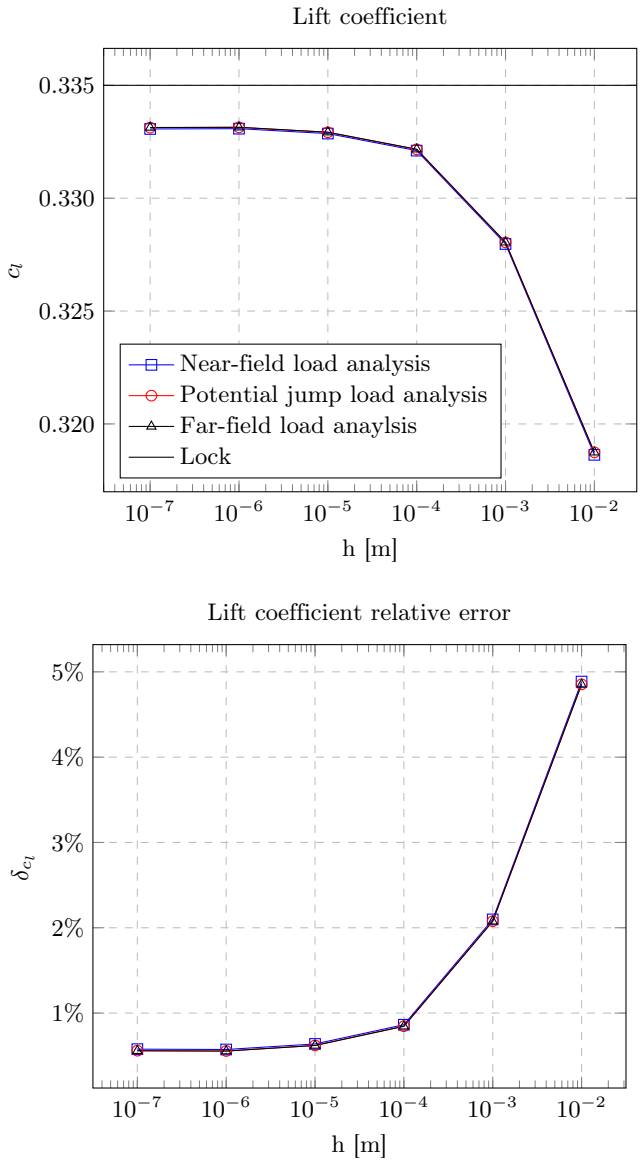

Figure 4.11: Mesh refinement study for compressible subsonic flow conditions (Case 1: $\alpha = 2°$ and $M_\infty = 0.63$).

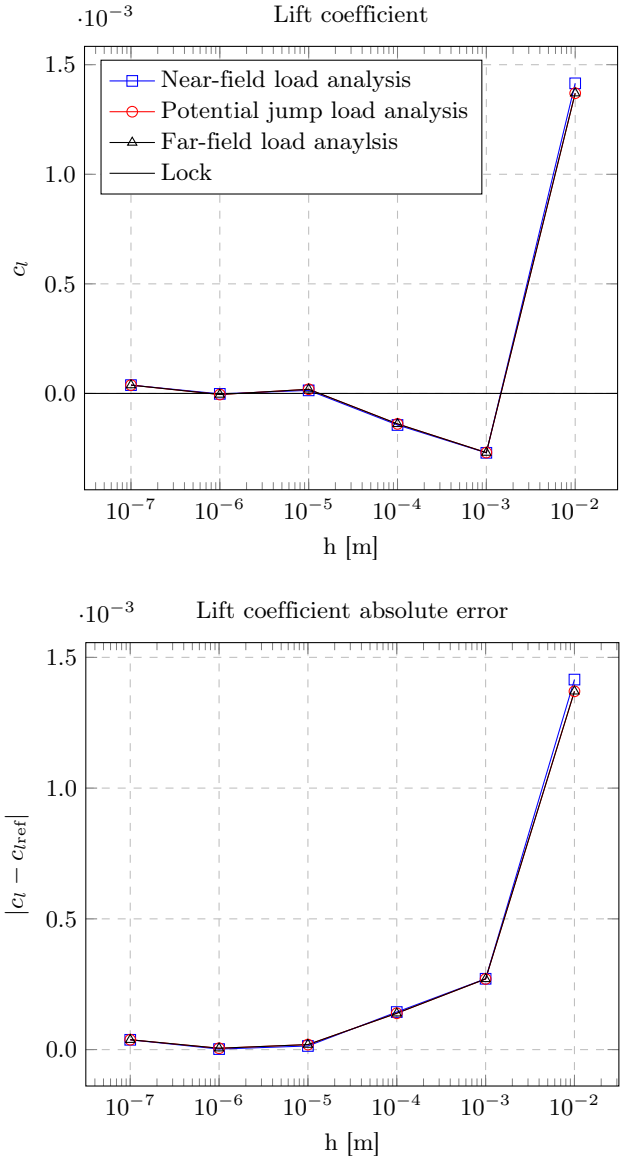

Figure 4.12: Mesh refinement study for compressible subsonic flow conditions (Case 2: $\alpha = 0°$ and $M_\infty = 0.72$).

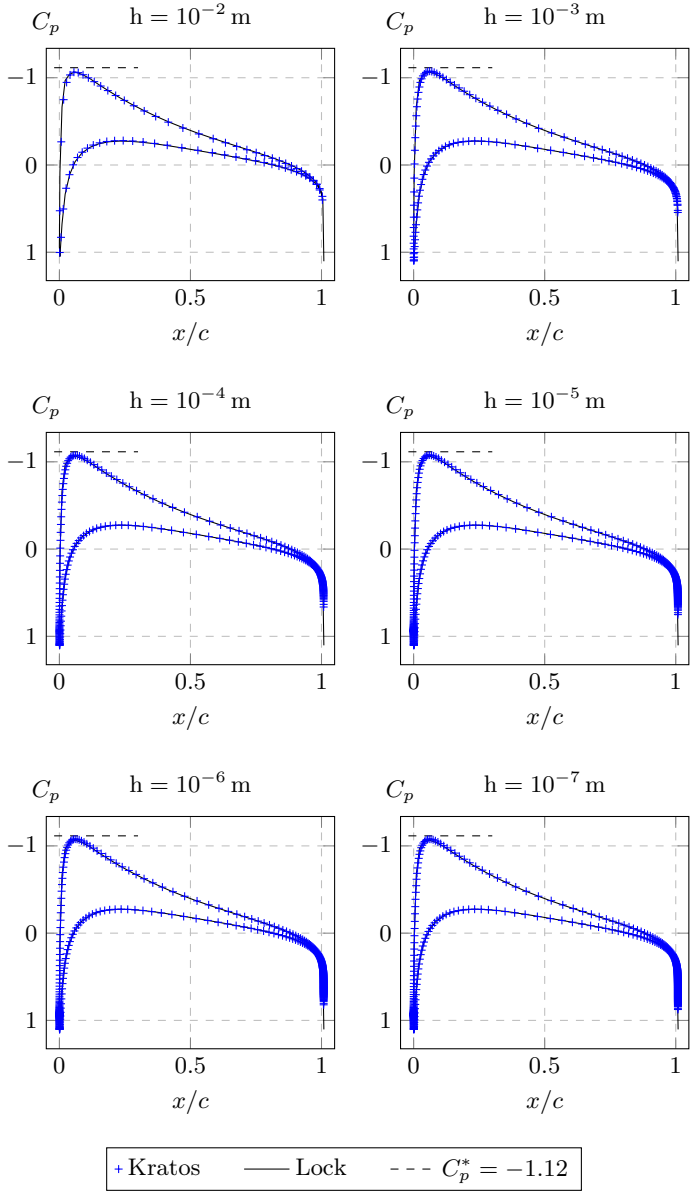

Figure 4.13: Pressure coefficient distribution (Case 1: $\alpha = 2°$, $M_\infty = 0.63$).

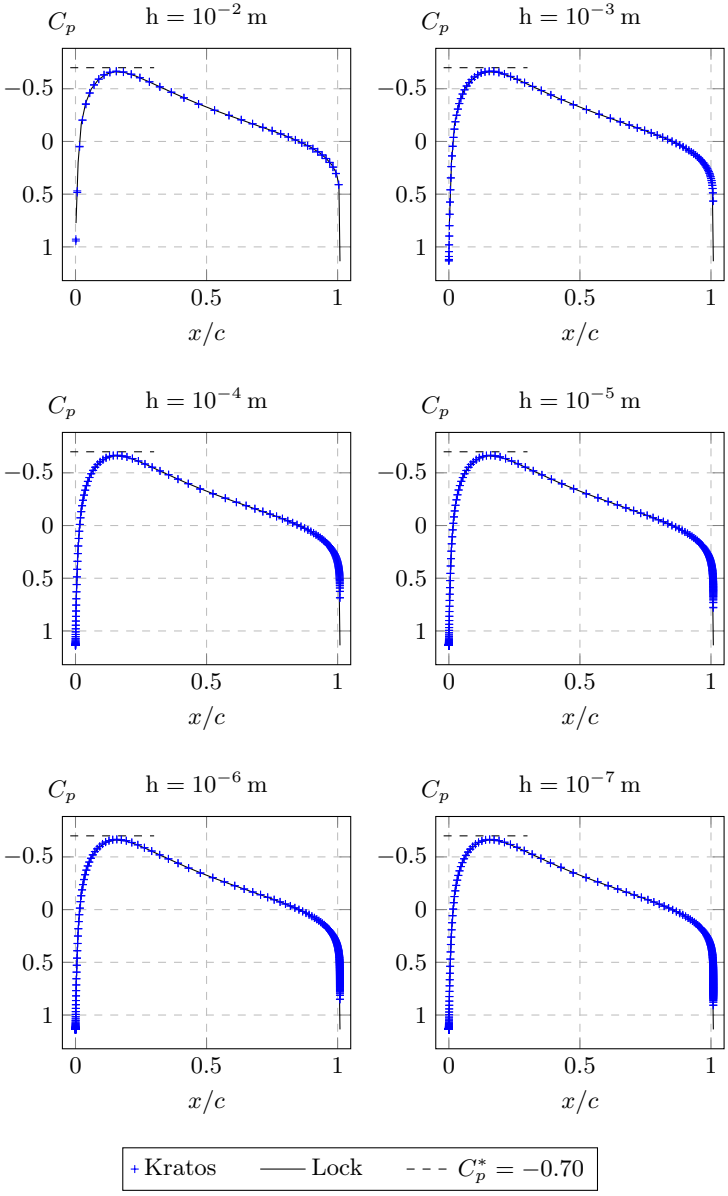

Figure 4.14: Pressure coefficient distribution (Case 2: $\alpha = 0°$, $M_\infty = 0.72$).

4.3.3 Newton Raphson's method convergence

To verify that the Jacobian is implemented correctly, the Newton Raphson method's convergence is evaluated. The residual's L_2 norm is presented in Tables 4.5 and 4.6, and displayed in Figures 4.15 and 4.16 over the nonlinear iteration number for each mesh refinement. Note that the residual converges quadratically once it is within the region of quadratic convergence so that the nonlinear problem converges in five to ten iterations with a tolerance of 10^{-10}. Interestingly, case one converges in five iterations for all mesh refinements, whereas case two shows different convergence for different mesh refinements.

h [m]	10^{-2}	10^{-3}	10^{-4}	10^{-5}	10^{-6}	10^{-7}
k			Resiual L_2 norm: $\lvert\boldsymbol{R}\rvert$			
1	$2 \cdot 10^{0}$	$1 \cdot 10^{0}$	$7 \cdot 10^{-1}$	$7 \cdot 10^{-1}$	$7 \cdot 10^{-1}$	$7 \cdot 10^{-1}$
2	$5 \cdot 10^{-2}$	$1 \cdot 10^{-1}$	$9 \cdot 10^{-2}$	$8 \cdot 10^{-2}$	$8 \cdot 10^{-2}$	$8 \cdot 10^{-2}$
3	$2 \cdot 10^{-4}$	$5 \cdot 10^{-4}$	$5 \cdot 10^{-4}$	$4 \cdot 10^{-4}$	$4 \cdot 10^{-4}$	$4 \cdot 10^{-4}$
4	$9 \cdot 10^{-9}$	$1 \cdot 10^{-8}$	$9 \cdot 10^{-9}$	$8 \cdot 10^{-9}$	$8 \cdot 10^{-9}$	$8 \cdot 10^{-9}$
5	$8 \cdot 10^{-12}$	$8 \cdot 10^{-12}$	$8 \cdot 10^{-12}$	$8 \cdot 10^{-12}$	$8 \cdot 10^{-12}$	$9 \cdot 10^{-12}$

Table 4.5: Newton Raphson convergence (Case 1: $\alpha = 2°$, $M_\infty = 0.63$).

h [m]	10^{-2}	10^{-3}	10^{-4}	10^{-5}	10^{-6}	10^{-7}
k			Resiual L_2 norm: $\lvert\boldsymbol{R}\rvert$			
1	$3 \cdot 10^{0}$	$2 \cdot 10^{0}$	$1 \cdot 10^{0}$	$1 \cdot 10^{0}$	$1 \cdot 10^{0}$	$1 \cdot 10^{0}$
2	$1 \cdot 10^{-1}$	$8 \cdot 10^{-1}$	$6 \cdot 10^{-1}$	$5 \cdot 10^{-1}$	$5 \cdot 10^{-1}$	$5 \cdot 10^{-1}$
3	$4 \cdot 10^{-4}$	$2 \cdot 10^{-1}$	$1 \cdot 10^{0}$	$1 \cdot 10^{0}$	$1 \cdot 10^{0}$	$1 \cdot 10^{0}$
4	$2 \cdot 10^{-8}$	$3 \cdot 10^{-3}$	$3 \cdot 10^{-1}$	$3 \cdot 10^{-1}$	$3 \cdot 10^{-1}$	$4 \cdot 10^{-1}$
5	$9 \cdot 10^{-12}$	$1 \cdot 10^{-7}$	$8 \cdot 10^{-2}$	$4 \cdot 10^{-1}$	$2 \cdot 10^{-1}$	$2 \cdot 10^{-1}$
6		$8 \cdot 10^{-12}$	$5 \cdot 10^{-3}$	$8 \cdot 10^{-2}$	$5 \cdot 10^{-2}$	$5 \cdot 10^{-2}$
7			$6 \cdot 10^{-6}$	$1 \cdot 10^{-2}$	$3 \cdot 10^{-3}$	$2 \cdot 10^{-3}$
8			$1 \cdot 10^{-11}$	$5 \cdot 10^{-5}$	$3 \cdot 10^{-6}$	$8 \cdot 10^{-7}$
9				$3 \cdot 10^{-10}$	$9 \cdot 10^{-12}$	$9 \cdot 10^{-12}$
10				$7 \cdot 10^{-12}$		

Table 4.6: Newton Raphson convergence (Case 2: $\alpha = 0°$, $M_\infty = 0.72$).

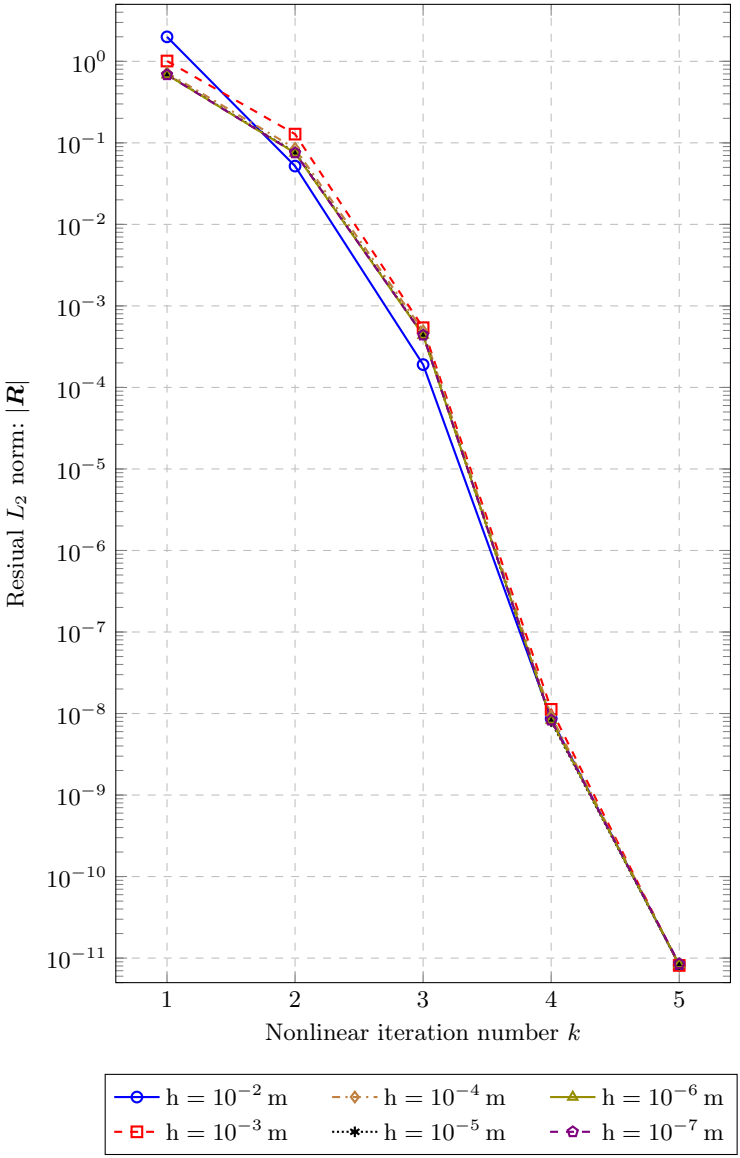

Figure 4.15: Newton Raphson convergence (Case 1: $\alpha = 2°$, $M_\infty = 0.63$).

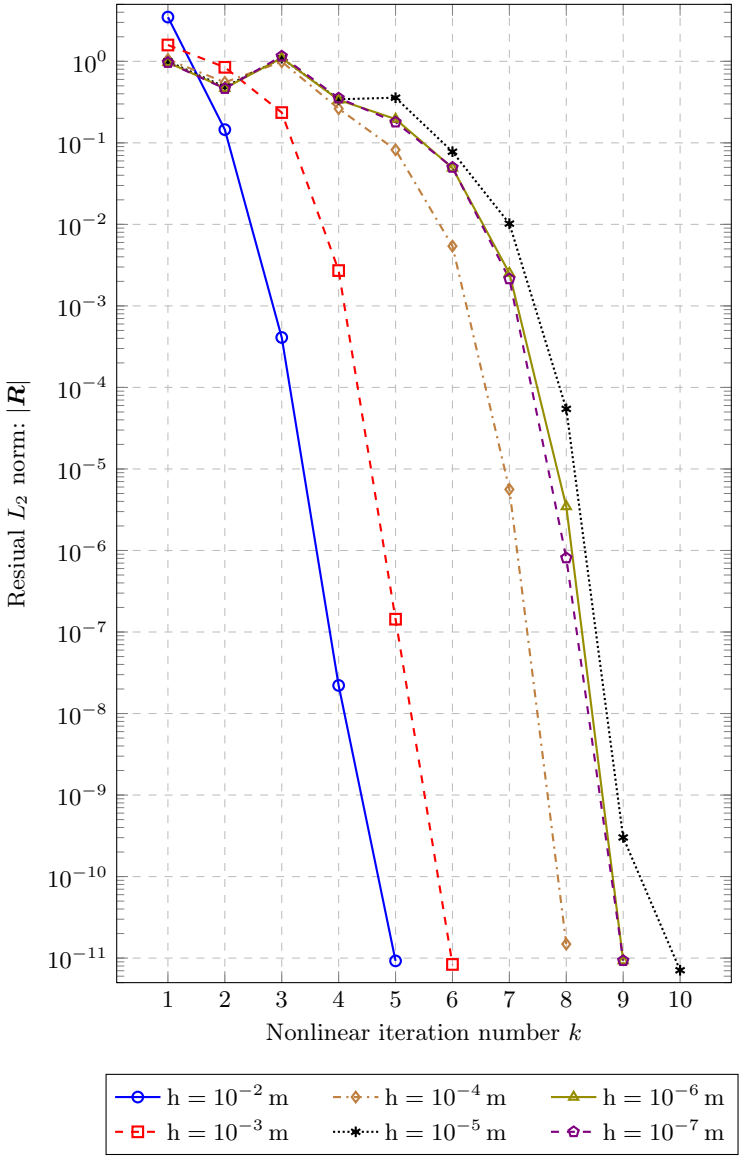

Figure 4.16: Newton Raphson convergence (Case 2: $\alpha = 0°$, $M_\infty = 0.72$).

4.4 Transonic flow around NACA 0012 airfoil[a]

In order to verify the transonic element, the four test cases presented in Table 4.7 are considered. These cases are highly nonlinear, and a load stepping control is required to achieve convergence (Table 4.8). Note that as the freestream Mach number and the angle of attack are increased, more dissipation and load steps are required to achieve convergence.

Case	α	M_∞	M_{crit}	μ_{c}
(1)	1.0	0.72	0.99	1.0
(2)	1.0	0.73	0.99	1.0
(3)	1.0	0.75	0.95	1.1
(4)	2.0	0.75	0.90	1.1

Table 4.7: Transonic test cases.

Case	(1)	(2)	(3)	(4)
Step	M_∞			
1	0.70	0.70	0.70	0.70
2	0.71	0.71	0.71	0.71
3	0.72	0.72	0.72	0.72
4		0.73	0.73	0.73
5			0.74	0.74
6			0.75	0.75

Table 4.8: Solution load stepping.

4.4.1 Mesh refinement study

The lift and moment coefficient's convergence is assessed for case 1 in Figures 4.17 and 4.18. The solution is compared with the reference data provided in [65]. The same level of accuracy as for the incompressible and the compressible subsonic cases is achieved. For a minimum element size smaller than 10^{-2}, the lift relative error is below 2%. Note that the three force analyses yield very similar results.

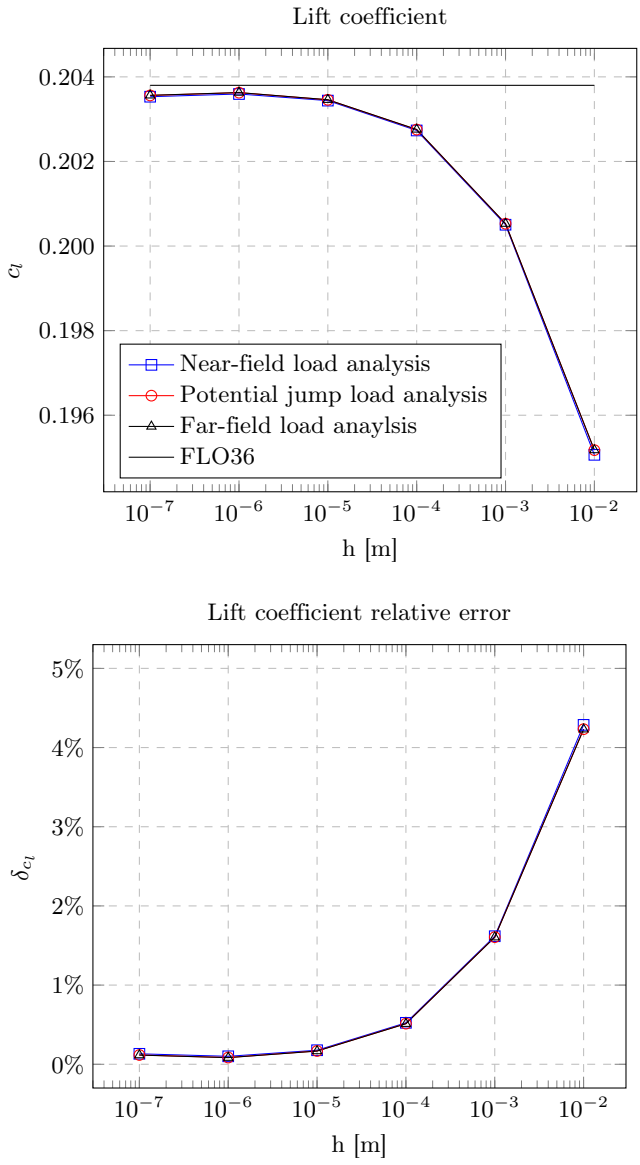

Figure 4.17: NACA 0012 mesh refinement study ($\alpha = 1°$, $M_\infty = 0.72$).

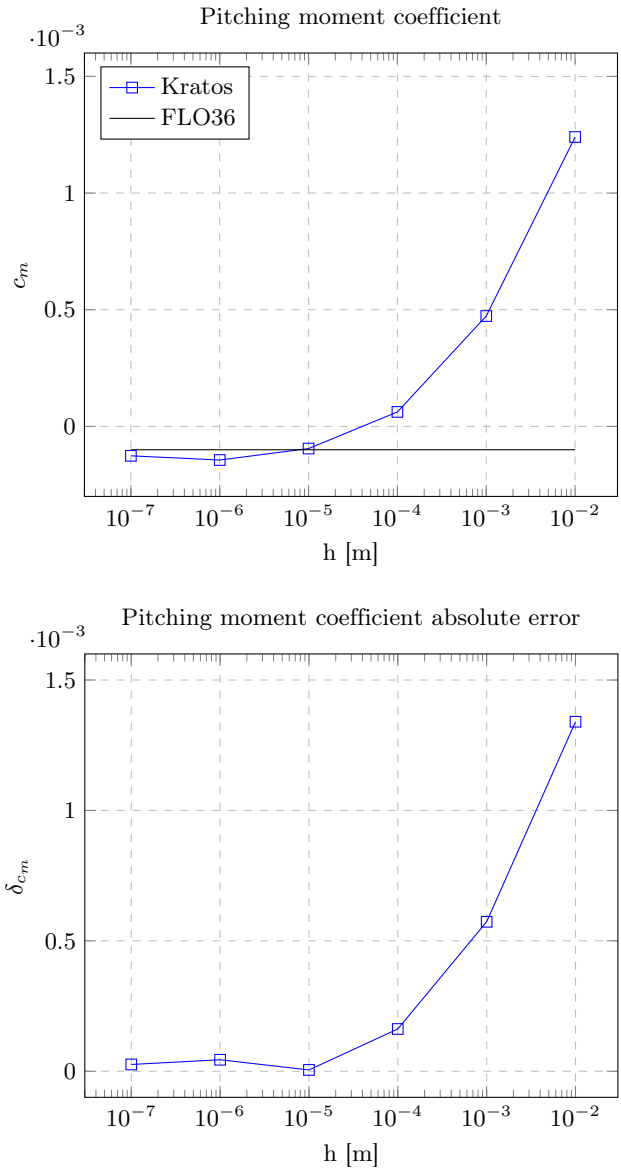

Figure 4.18: NACA 0012 mesh refinement study ($\alpha = 1°$, $M_\infty = 0.72$).

4.4.2 Pressure coefficient distribution verification

The resulting pressure coefficient distribution is compared with the reference data in Figure 4.19 for the four test cases. In the transonic regime, subsonic and supersonic regions coexist in the vicinity of the profile. The supersonic regions can be identified by comparing the value of the pressure coefficient to the critical value, marked with a dashed line. If the pressure coefficient is smaller than the critical value at a given point, the flow is supersonic. Note that the pressure distribution trend on the upper surface is different from the subsonic cases, where the flow expands around the leading edge and then starts compressing. In these cases, the flow continues to expand after going

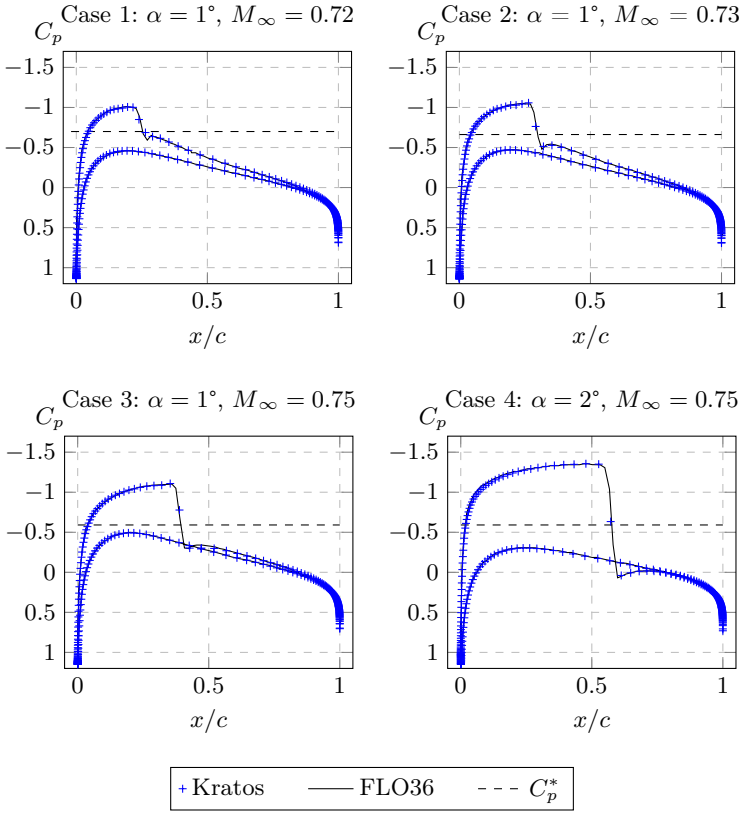

Figure 4.19: Pressure coefficient distributions for transonic test cases.

around the leading edge and returns to subsonic speed through a shock wave. Figure 4.20 shows the pressure coefficient contour plot in the vicinity of the airfoil for case 4. In this figure, the stagnation points are indicated in red. The shock wave can be observed on top of the airfoil.

What is a shock wave? Anderson describes shock waves as extremely thin regions across which the flow variables can change drastically [66]. This is precisely what is represented in Figure 4.19, where the pressure coefficient drastically changes across the shock wave on the upper surface. Note that an explosive compression process occurs within the shock wave, where the pressure coefficient increases rapidly across the wave. Also, note that the flow ahead of the shock is supersonic, whereas the flow is subsonic behind the shock.

But how does the shock wave appear in the first place? If the freestream Mach number is progressively increased, at some point, a region of local supersonic flow appears on the upper surface. Because the flow is supersonic, pressure waves coming towards this region from behind cannot penetrate the supersonic pocket, and pressure progressively starts to build at the interface between the supersonic and subsonic regions.

For $M_\infty = 0.72$, the shock is relatively weak, and the supersonic region is small. As the Mach number and the angle of attack are increased, the shock moves aft and becomes stronger, increasing the size of the supersonic region and requiring more dissipation and more load steps to achieve convergence

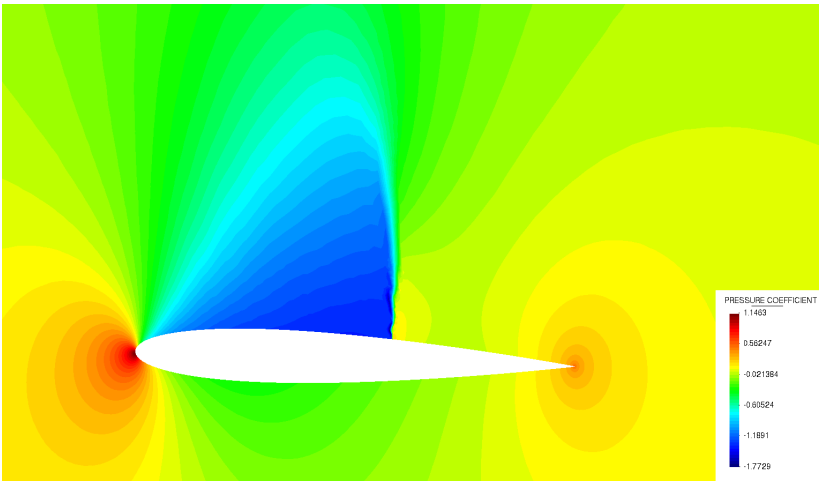

Figure 4.20: Pressure coefficient contour plot ($\alpha = 2.0°$, $M_\infty = 0.75$).

(Tables 4.7 and 4.8). The results obtained for cases 3 and 4 should be interpreted cautiously. Such strong shock waves typically cause the separation of the boundary layer, deeming the solution outside of the method's limits of application. Also, note that the solution's sensitivity with respect to the freestream Mach number and angle of attack is very large, leading small changes of M_∞ and α to large changes in the solution.

For all cases, the shock is captured within one element. This gives a sharp definition of the shock compared to other reference solutions, where the shock is typically smeared over several grid points. This is probably not because of the artificial compressibility method but rather a consequence of using a coarse mesh at the shock's position. Note that the pressure coefficient is continuous across the wake, meaning that the wake pressure equality condition is satisfied.

4.4.3 Newton Raphson's method convergence

To verify that the Jacobian is also implemented correctly for the transonic element, the Newton Raphson method's convergence is evaluated. The residual's L_2 norm is presented in Table 4.9 for all cases second load step. As for the compressible subsonic cases, the residual converges quadratically once it is within the region of quadratic convergence.

Case	(1-2)	(3)	(4)
k	Resiual L_2 norm: $\lvert\boldsymbol{R}\rvert$		
1	$1 \cdot 10^{-2}$	$1 \cdot 10^{-2}$	$5 \cdot 10^{-1}$
2	$4 \cdot 10^{-3}$	$5 \cdot 10^{-4}$	$3 \cdot 10^{-1}$
3	$4 \cdot 10^{-5}$	$1 \cdot 10^{-6}$	$9 \cdot 10^{-2}$
4	$4 \cdot 10^{-9}$	$9 \cdot 10^{-12}$	$2 \cdot 10^{-2}$
5	$9 \cdot 10^{-12}$		$7 \cdot 10^{-5}$
6			$8 \cdot 10^{-10}$

Table 4.9: Newton Raphson convergence (Step 2: $M_\infty = 0.71$).

4.5 Transonic flow around Korn supercritical airfoil

Supercritical airfoils are designed to delay the onset of wave drag in transonic flow. During the late 1960s, Richard Whitcomb developed airfoils using an experimental approach to control the flow's expansion to supersonic conditions and its following recompression [67]. Dave Korn made another major contribution to the development of supercritical airfoils at the NYU

Courant Institue in the early 1970s when he developed the Korn equation to estimate transonic airfoils' performance [68].

4.5.1 Pressure coefficient distribution verification

To further verify the embedded wake approach in transonic conditions, the flow solution around the Korn supercritical airfoil is compared to the reference data presented in [65]. The mesh used in this study is shown in Figure 4.21, where the main characteristics of supercritical airfoils can be observed:

- A relatively large leading edge radius to expand the flow towards the upper surface.
- A flat upper surface to maintain the supersonic flow at constant pressure and, in some cases, slow it down slightly before the shock.
- An aft camber to increase the lift.
- An almost parallel upper and lower surfaces at the trailing edge to avoid flow separation.

The test cases considered in this section are presented in Table 4.10. Note that the required artificial dissipation increases with the angle of attack and the Mach number like for the NACA 0012. The resulting pressure coefficient distribution is compared with the reference data in Figure 4.22. For case 1, the shock on the upper surface is very weak. After recompression, the pressure

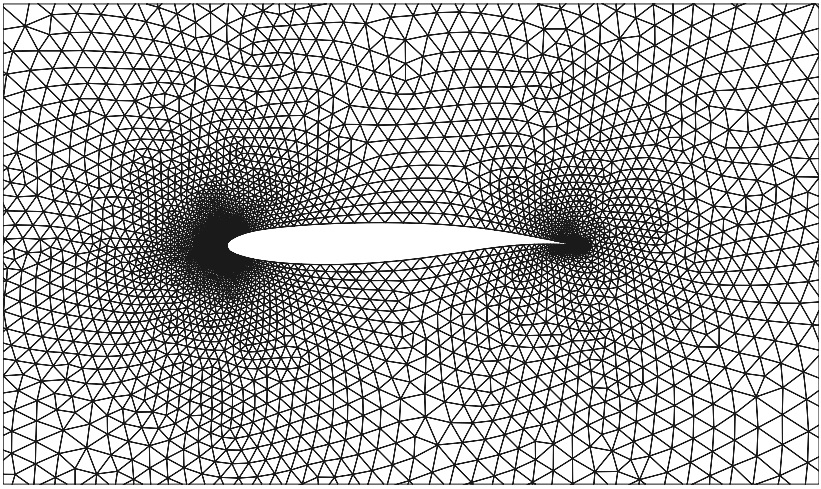

Figure 4.21: Mesh around Korn's supercritical airfoil.

Case	α	M_∞	M_{crit}	μ_c
(1)	1.0	0.70	0.99	1.0
(2)	2.0	0.70	0.93	1.0
(3)	0.2	0.75	0.91	1.0
(4)	0.7	0.75	0.88	1.6

Table 4.10: Korn supercritical airfoil transonic test cases.

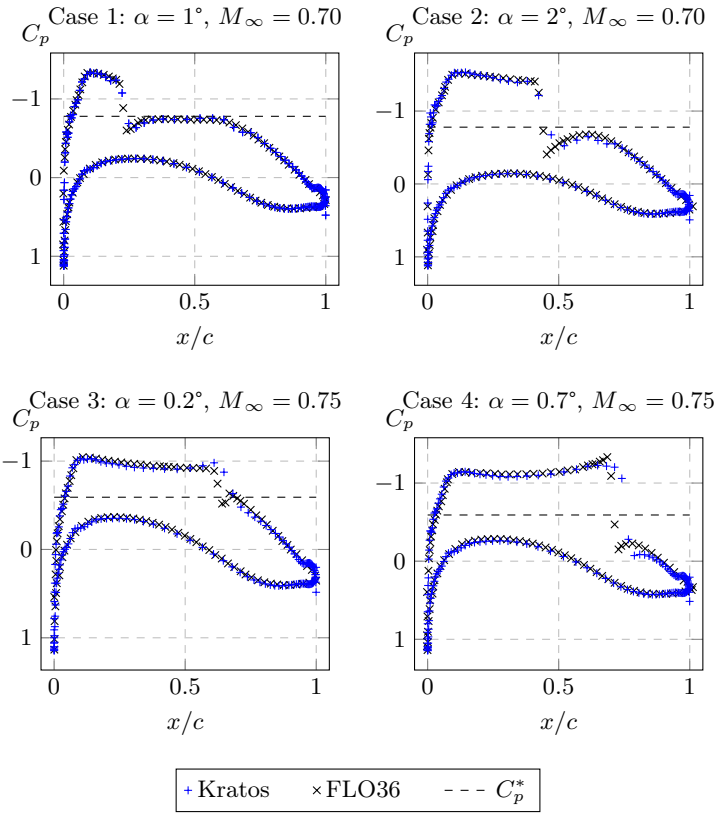

Figure 4.22: Pressure coefficient distributions for transonic test cases.

coefficient remains constant and slightly below the critical value. The shock is captured sharply, and the results are in good agreement with the reference data. The consequences of increasing the angle of attack by just one degree are presented at the top right for case 2. The shock has become stronger and has moved aft by around 20% of the chord. In this case, the area of constant pressure is no longer after but before the shock. A good agreement is found in general between the obtained pressure coefficient and the reference, being the largest disagreements in the vicinity of the shock wave where the solution is most sensitive. Similar results can be observed for cases 3 and 4, where even though the angle of attack has been decreased, the freestream Mach number has been increased, moving the shock even after, increasing the region of constant pressure, and reducing the critical pressure coefficient. The shock in case 4 is relatively strong and could lead to the separation of the boundary layer, meaning that the results would be outside of the range of applicability of the potential approximation.

4.6 Drag divergence study

Drag divergence is a transonic effect that refers to the rapid increase of the drag coefficient as the freestream Mach number increases, caused by the development of a shock wave on the airfoil's upper surface. The Mach number at which the onset of drag divergence occurs is denoted drag-divergence Mach number. In order to verify that the implemented solver can capture this effect and show the difference between using conventional and supercritical airfoils, the flow over the NACA 0012 and Korn airfoils is computed for an increasing freestream Mach number at a constant angle of attack. The resulting drag and lift coefficients are plotted over the freestream Mach number and against each other in Figure 4.23, where the critical Mach numbers are marked with black dashed lines. The critical Mach number is defined as the minimum Mach number at which the first point on the flow field, typically on the airfoil's upper surface, reaches sonic conditions. In order to make the comparison fair, the angles of attack have been chosen such that both airfoils have approximately the same lift coefficient under subcritical conditions. The dashed green curve indicates the theoretical trend that the curves follow after separation occurs outside the potential solver range of application. This trend is based on wind tunnel experiments of a symmetric airfoil with a relative thickness of 10%, so it should not be interpreted quantitatively but rather qualitatively. In order to discuss the results presented in Figure 4.23, the pressure coefficient distribution change over the NACA 0012 for an increasing freestream Mach number is shown in Figure 4.24.

Figure 4.23 shows that in the incompressible and compressible subsonic regime, below the critical Mach number, the lift increases slowly due to the flow compressibility effects, while the drag values are zero. This zero drag result is in accordance with D'Alambert's paradox. Kutta-Joukowski theorem shows that the drag over a two-dimensional body under potential flow is

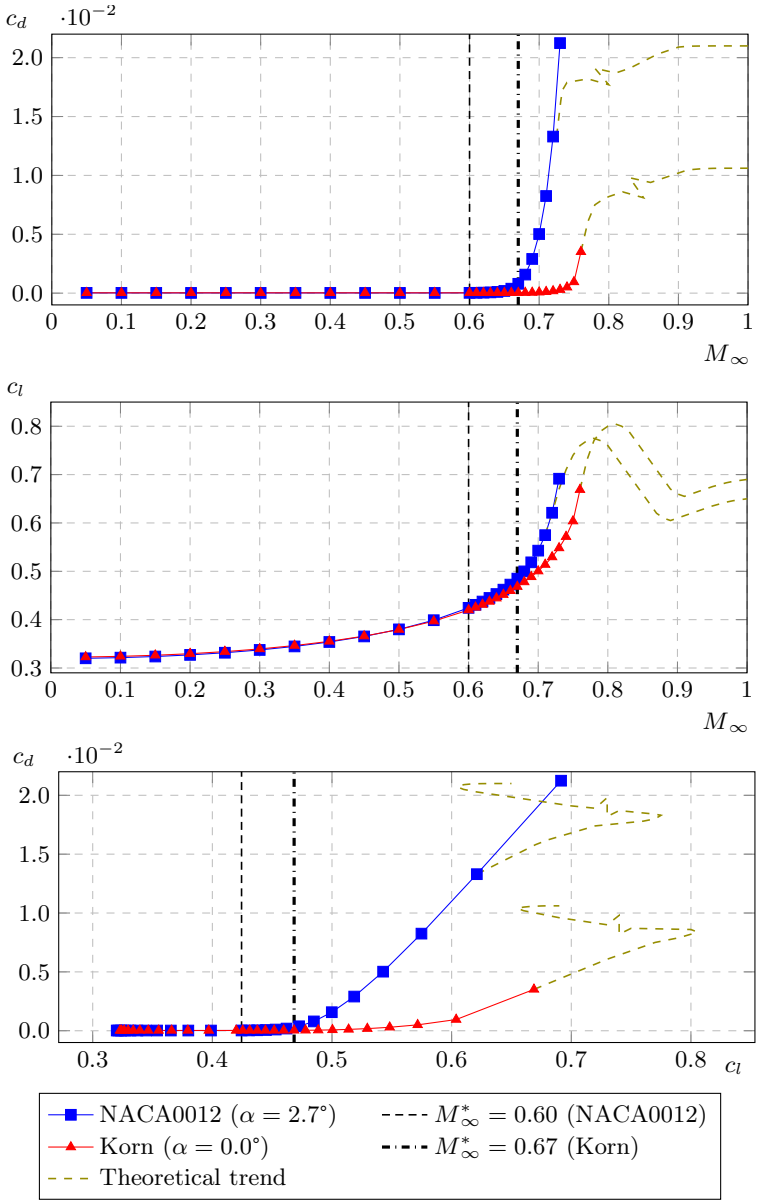

Figure 4.23: Drag divergence study.

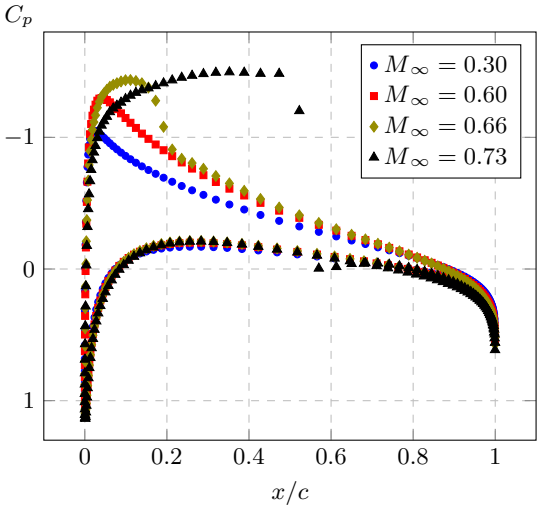

Figure 4.24: Pressure coefficient change for increasing freestream Mach number (NACA 0012 $\alpha = 2.7°$).

zero [66]. The increase in lift can be explained by looking at Figure 4.24 and comparing the change in the pressure coefficient distributions between $M_\infty = 0.3$ and $M_\infty = 0.6$. Note that the area enclosed by the red data is larger than the area enclosed by the blue one. The largest changes occur on the airfoil's upper surface, where the compressibility effects are more noticeable, whereas the pressure coefficient remains practically constant on the lower surface.

Once the critical Mach number is reached, a shock wave starts to develop on the airfoils' upper surface, indicating the transonic regime's beginning. The top plot in Figure 4.23 shows that right after surpassing the critical Mach number, the drag coefficient increases relatively slowly. This is because the shock is fairly weak, and so the associated wave drag is small. If the freestream Mach number is further increased, the area covered by the supersonic flow on top of the airfoil grows, and the shock wave moves after becoming stronger (see the green data corresponding to $M_\infty = 0.66$ in Figure 4.24). In the beginning, this movement and strengthening of the shock wave happen slowly, explaining the small increase of drag observed in Figure 4.23.

Nevertheless, there is a freestream Mach number, at which the shock's movement and strengthening accelerate, causing the drag coefficient to increase rapidly (see the black data corresponding to $M_\infty = 0.73$ in Figure 4.24 and the

corresponding change in the NACA 0012 drag coefficient between $M_\infty = 0.66$ and $M_\infty = 0.73$ in the top plot of Figure 4.23). The freestream Mach number at which this happens is the so-called drag-divergence Mach number, which for the considered angles of attack is predicted to be around $M_\infty = 0.66$ and $M_\infty = 0.75$ for the NACA 0012 and Korn airfoils, respectively. The fact that the drag-divergence Mach number is larger for the supercritical airfoil than for the conventional one shows the substantial benefit of using supercritical airfoils in the transonic regime. One could argue that this is not a fair comparison because even though the drag coefficient is larger for the NACA 0012 than for the Korn airfoil for any given Mach number in the transonic regime, the lift coefficient is also larger. However, the bottom plot in Figure 4.23 shows that for the same lift coefficient, the associated drag is much smaller for the Korn airfoil than for the NACA 0012. Supercritical airfoils are designed to have significantly better transonic performance than conventional airfoils, allowing them to fly at larger Mach numbers with less drag.

If the freestream Mach number is further increased, there is a point in which the pressure increment across the shock is high enough to produce the separation of the boundary layer at the shock's base. Typically, separation occurs when the local Mach number before the shock is between 1.25 and 1.30, and as the Reynolds number is high, separation happens when the boundary layer is already turbulent. Beyond this point, the implemented potential solver is not applicable anymore, and a solver capturing the viscous effects of the boundary layer is required.

This study shows that the potential transonic solver with an embedded wake approach can capture the phenomenon of drag divergence.

4.6.1 Critical Mach number verification

To further verify the transonic solver, the predicted critical Mach number is compared with the solution obtained via the graphical method illustrated in Figure 4.25 for the Korn airfoil. This method consists of first plotting the critical pressure coefficient:

$$C_p^* = \frac{2}{\gamma M_\infty^2} \left[\left(\frac{1 + \frac{\gamma-1}{2} M_\infty^2}{1 + \frac{\gamma-1}{2}} \right)^{\frac{\gamma}{\gamma-1}} - 1 \right] \tag{4.18}$$

over the freestream Mach number. This curve is marked in blue in Figure 4.25. Second, the minimum pressure coefficient obtained from the incompressible solution $(C_{p\min})_{\text{inc}}$ is used to estimate the minimum pressure coefficient in compressible flow predicted with the Prandtl-Glauert transformation:

$$C_{p\min} = \frac{(C_{p\min})_{\text{inc}}}{\sqrt{1 - M_\infty^2}} \tag{4.19}$$

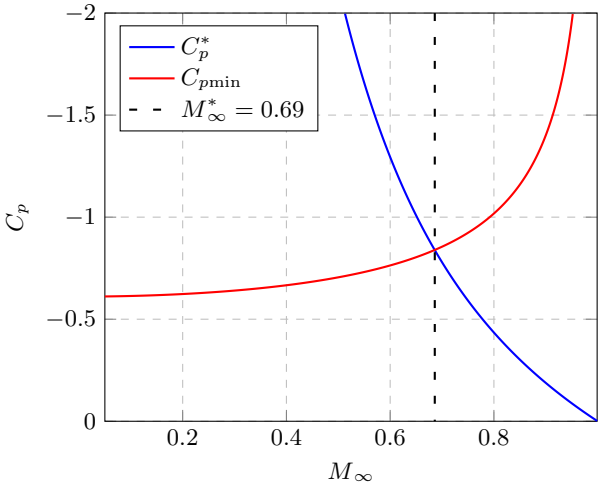

Figure 4.25: Graphical Solution to find M_∞^* for the Korn airfoil ($\alpha = 0°$).

Eq. (4.19) is plotted in red over the freestream Mach number in Figure 4.25. The intersection between both curves yields the sought solution, which is marked with a dashed line. In this case, the solution obtained with the graphical method is $M_\infty^* = 0.69$, which is very close to the value predicted by the solver ($M_\infty^* = 0.67$). The solutions are not expected to be the same because this method uses Prandtl-Glauert transformation, which assumes that the airfoil is slender ($t/c \ll 1$) and that the problem is linear. Still, the problem at hand fulfills these assumptions (at least to a certain degree), and so the solutions provided by both methods are very close to each other.

4.6.2 Multi-fidelity analysis study

In total, three different solvers corresponding to three different fidelity levels have been implemented (Table 4.11). Figure 4.26 and Table 4.12 compare respectively the pressure coefficient distribution and the aerodynamic coefficients obtained with each of the solvers in different flow regimes. To compare the computational cost between the different fidelities, Table 4.12 also presents the central processing unit (CPU) times required by each solver. All cases presented in this section were run in serial in a desktop machine fitted with an Intel Xeon E5-1650 processor (3.5 GHz).

The three solvers are expected to yield identical results in the incompressible regime ($M_\infty = 0.01$) because they all solve the same equation. Indeed,

Fidelity level	Solver
Low-fidelity	Linear incompressible solver
Medium-fidelity	Nonlinear compressible subsonic solver
High-fidelity	Nonlinear compressible transonic solver

Table 4.11: Fidelity levels implemented in KRATOS.

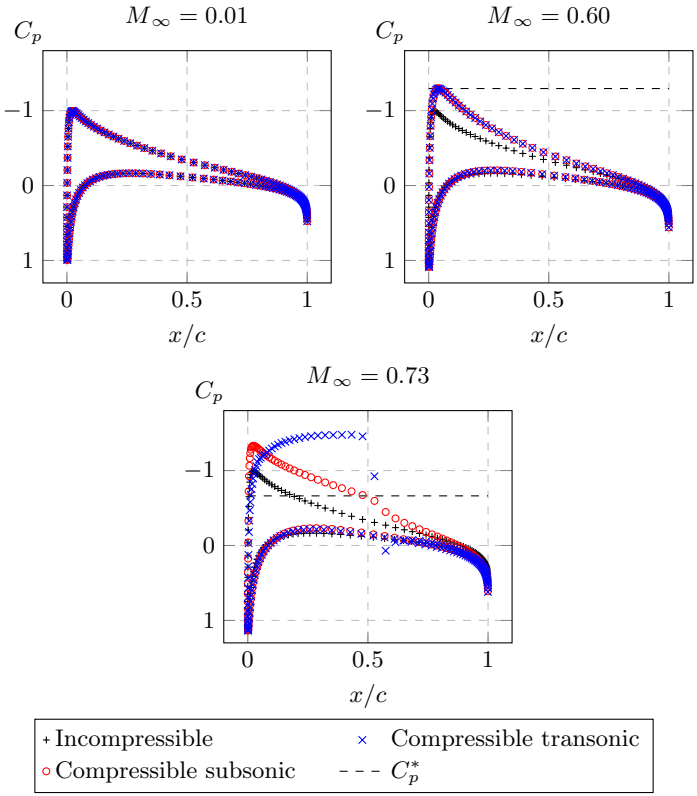

Figure 4.26: Pressure coefficient for different fidelity solvers (NACA 0012 $\alpha = 2.7°$).

Incompressible flow $M_\infty = 0.01$				
Solver	c_l	c_d	c_m	Time [s]
Incompressible	0.320	$2 \cdot 10^{-5}$	$2.7 \cdot 10^{-3}$	1.8
Subsonic	0.320	$2 \cdot 10^{-5}$	$2.7 \cdot 10^{-3}$	2.0
Transonic	0.320	$2 \cdot 10^{-5}$	$2.7 \cdot 10^{-3}$	2.3
Compressible subsonic flow $M_\infty = 0.60$				
Solver	c_l	c_d	c_m	Time [s]
Incompressible	0.320	$2 \cdot 10^{-5}$	$2.7 \cdot 10^{-3}$	1.8
Subsonic	0.425	$1 \cdot 10^{-5}$	$1.8 \cdot 10^{-3}$	2.3
Transonic	0.425	$1 \cdot 10^{-5}$	$1.8 \cdot 10^{-3}$	2.8
Transonic flow $M_\infty = 0.73$				
Solver	c_l	c_d	c_m	Time [s]
Incompressible	0.320	$2 \cdot 10^{-5}$	$2.7 \cdot 10^{-3}$	1.8
Subsonic	0.511	$3 \cdot 10^{-3}$	$1.2 \cdot 10^{-2}$	2.5
Transonic	0.677	$2 \cdot 10^{-2}$	$1.5 \cdot 10^{-2}$	19.4

Table 4.12: Aerodynamic coefficients and computational time.

the pressure coefficient data lay on top of each other, and the resulting aerodynamic coefficients are identical. The drag coefficient is not exactly zero due to the discretization error. The subsonic and transonic solvers require more time than the incompressible one because they need two Newton Raphson iterations to converge. The transonic solver takes longer than the subsonic one due to the larger amount of internal checks inside the element, penalizing the time it takes to assemble the global Jacobian system matrix.

The nonlinear solvers give the same result in the compressible subsonic regime ($M_\infty = 0.60$) but different from the linear solver solution. This case is outside of the range of application of the linear solver, which cannot capture nonlinear compressibility effects that are especially significant on the airfoil's upper surface, as shown in Figure 4.26.

In the transonic regime ($M_\infty = 0.73$), all solvers provide a different prediction. Note that the linear solver solution is the same as in the incompressible and compressible subsonic regimes since this solution is independent of the freestream Mach number. The nonlinear subsonic solver does not implement an artificial compressibility method and thus cannot capture shock waves. The transonic solver can capture the shock wave on the upper surface and

the associated wave drag. The difference between the computational time is much more noteworthy in this regime. The linear solver only requires one linear solve and the nonlinear solver converges within seven Newton Raphson iterations, whereas the transonic solver needs eight load steps to converge, each step requiring from five to nine Newton Raphson iterations. Note that a large freestream Mach number was selected for this case to show the difference between the solvers. However, it may well be that the shock wave is too strong and causes the separation of the boundary layer, making the transonic solver also outside of its range of applicability.

In conclusion, the linear solver is always the fastest but provides only accurate solutions in the incompressible flow regime. The nonlinear subsonic and transonic solvers require a similar amount of time in the subsonic regime and provide the same solution. In general, this might make the transonic solver more appealing than the subsonic one since it provides more accurate solutions in the low transonic regime.

4.7 3D rectangular wing with NACA 0012 airfoil section in incompressible flow[a]

In order to verify the embedded wake approach in three dimensions, first, the incompressible flow solution around a rectangular wing of aspect ratio 4 at an angle of attack of $\alpha = 5°$ is compared with the solution provided by XFLR5. XFLR5 is an analysis tool for streamlined bodies flying at low

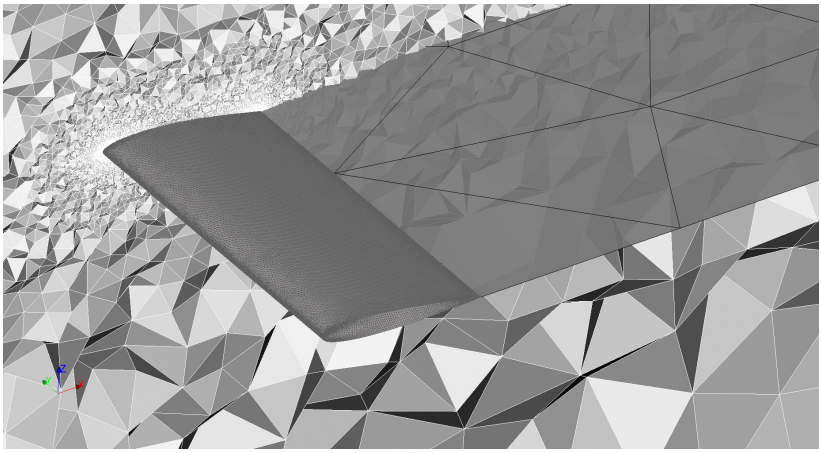

Figure 4.27: Rectangular NACA 0012 wing's mesh.

Reynolds numbers [69]. Figure 4.27 shows the wing's surface mesh and a clip of the tetrahedral volume mesh along the symmetry plane. The wake surface is indicated in black triangles with transparent faces. Note that the wake's STL mesh is only used to define the wake's geometry. The mesh is refined towards the leading and trailing edges to capture the geometry and the solution gradients as in the airfoil cases. In contrast to the two-dimensional cases, a refinement towards the wake is necessary to capture the velocity potential's spanwise variation. This requirement is not specific to the embedded wake approach but also applies to body-fitted wake approaches. The clip of the tetrahedral mesh in Figure 4.27 shows that the computational mesh in the vicinity of the wake is much finner. The parameters defining the mesh are the mesh minimum element size (0.002 m), the wing surface mesh growth rate (0.2), and the volume mesh growth rate (0.64). The domain's size is 25 meters. The volume mesh has a total of $1.4 \cdot 10^6$ degrees of freedom and $8 \cdot 10^6$ elements. The wing's surface mesh has $1.2 \cdot 10^5$ degrees of freedom and $2.4 \cdot 10^5$ triangular conditions.

4.7.1 Pressure coefficient distribution verification

Figure 4.28 compares the resulting pressure coefficient distribution with the solution of XFLR5 at four different wing sections, where each section spanwise location y is nondimentionalized using the half span b ($\eta = y/b$). Note that the embedded wake approach captures the stagnation point at the trailing edge in this three-dimensional case.

4.7.2 Potential jump distribution verification

Figure 4.29 shows the potential jump spanwise distribution at the trailing edge and at the intersection between the wake and a Trefftz plane positioned at the outlet, justifying the need to refine towards the wake. The linearized pressure equality condition imposes the potential jump to be constant in the direction of the freestream velocity. Figure 4.29 shows that this condition is fulfilled accurately. The largest disagreements occur in the vicinity of the wake tips, where the mesh at the outlet is too coarse and cannot capture the largest solution gradients. Note that as the potential jump tends to zero towards the wake tips, the error introduced in the formulation due to the lack of conformity between the elements is small. Figure 4.30 presents the potential jump contour plot at the wake surface, showing that the potential jump remains constant in the direction of the freestream velocity. In order to show that the embedded wake approach is also capable of capturing the wingtip vortices, Figure 4.31 shows a front view of the wing where the streamlines shed from the wingtips are displayed.

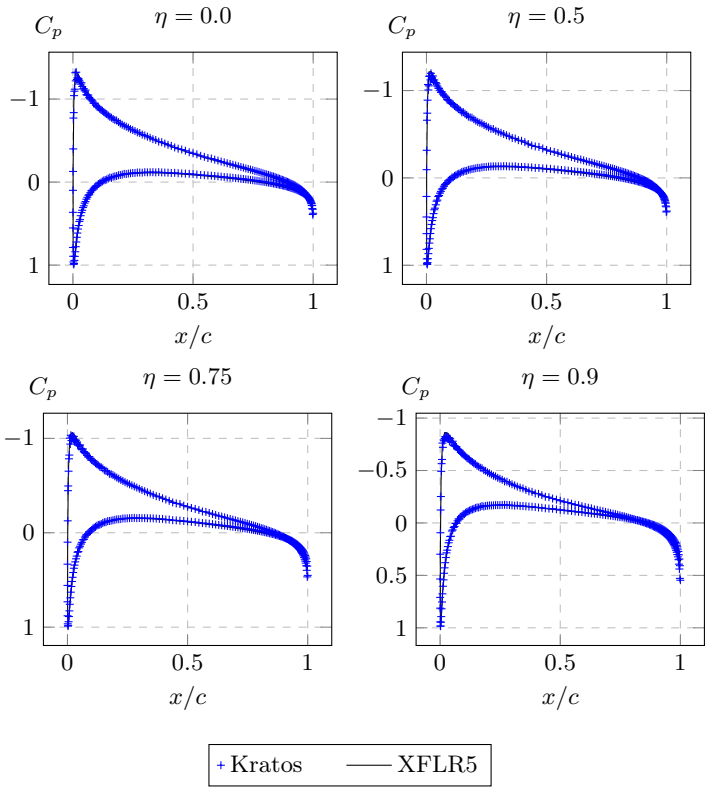

Figure 4.28: Pressure coefficient distribution at different wing sections.

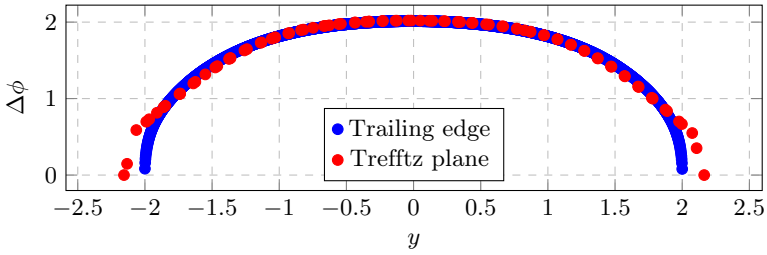

Figure 4.29: Potential jump spanwise distribution.

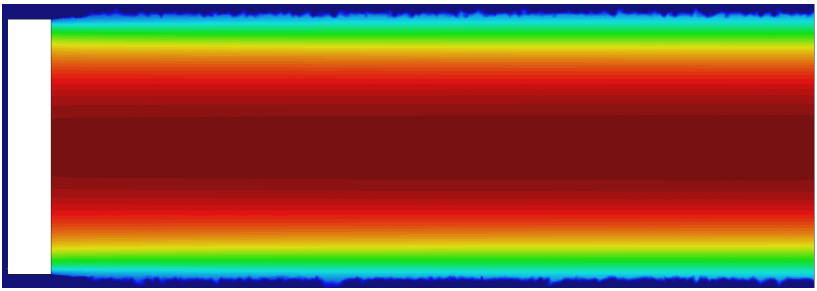

Figure 4.30: Potential jump contour plot at the wake surface.

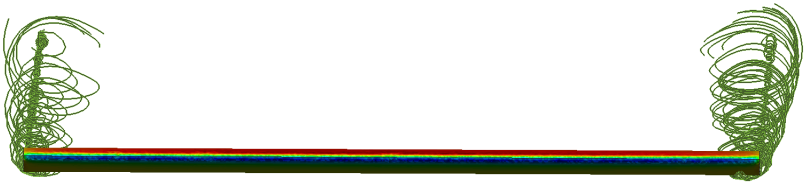

Figure 4.31: wingtip vortices.

4.8 3D ONERA M6 wing transonic validation case[b]

This section presents the validation and verification of the three-dimensional potential transonic solver using the proposed embedded wake approach. In order to do so, the flow solution over the ONERA M6 wing is compared with wind tunnel test data and with reference solutions from other solvers using different fluid fidelity levels. The Onera M6 wing is a standard CFD validation case for external transonic flows due to the complex double shock appearing on the upper surface and the underlying local supersonic flow. In this case, the wing is at an angle of attack of $\alpha = 3.06°$ and a freestream Mach number of $M_\infty = 0.84$. These conditions correspond to Test 2308 described in [70].

4.8.1 Wing's geometry and mesh

Onera M6 is a swept, semi-span wing with no twist. The wing's surface is constructed via conical generation from the symmetrical ONERA-D airfoil, i.e., all airfoil sections are homothetical. Figure 4.32 presents the parameters describing the wing's planform geometry. The numbers 1 to 6 in Figure 4.32 indicate the position of the sections where the pressure coefficient distribution

Parameter	Value
Span b	1.1963 m
Mean aerodynamic chord $\bar{c}$	0.64607 m
Aspect ratio Λ	3.8
Taper ratio λ	0.562
Sweep angle φ_{25}	26.7°
Leading edge sweep	30.0°
Trailing edge sweep	15.8°

Sections	
N	y/b
1	0.20
2	0.44
3	0.65
4	0.80
5	0.90
6	0.95

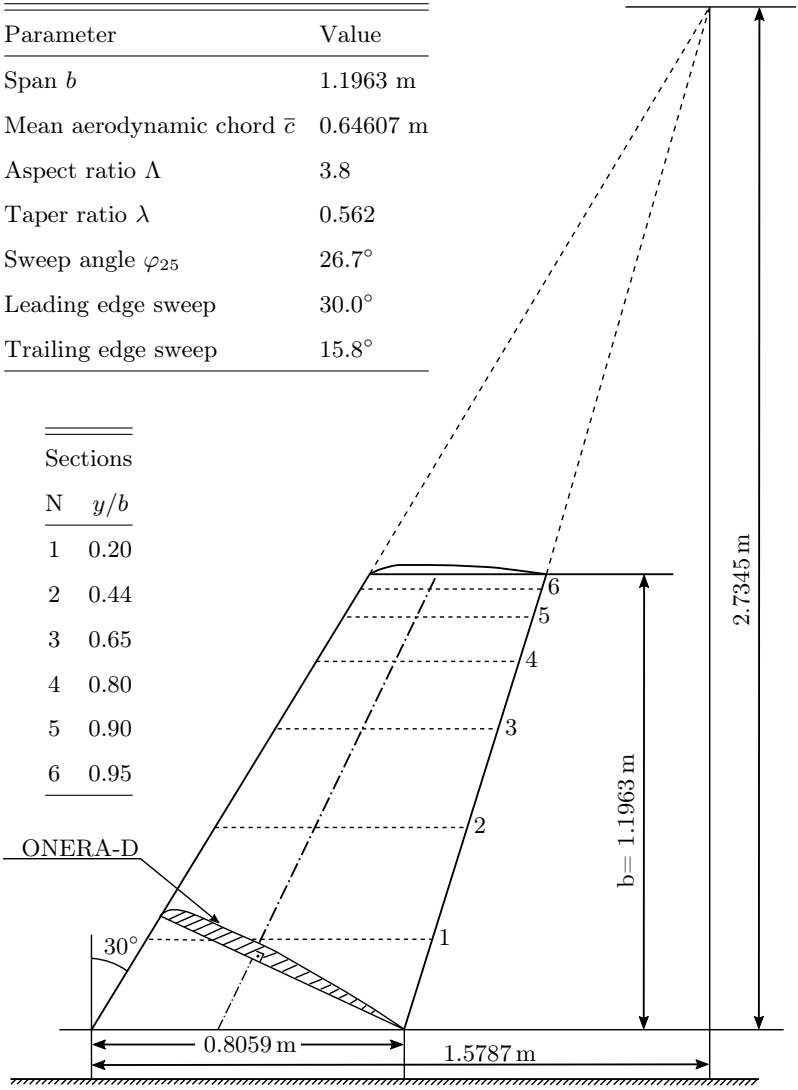

Figure 4.32: ONERA M6 planform layout [70].

is analyzed. The reference area for the computation of the aerodynamic coefficients is $A_{\text{ref}} = 0.7532\,\text{m}^2$. The ONERA-D airfoil coordinates can be found in [70], where it can be seen that the trailing edge has a finite thickness. For the purposes of this study, the CAD geometry is taken from [71], where the trailing edge has been made sharp, as described in [72].

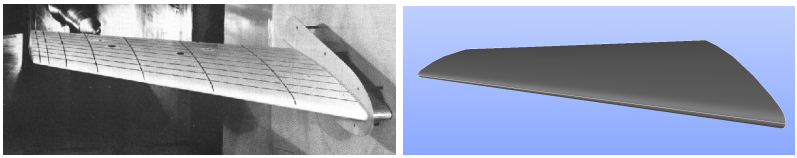

(a) Wind tunnel model [70]. (b) CAD model [72].

Figure 4.33: ONERA M6 models.

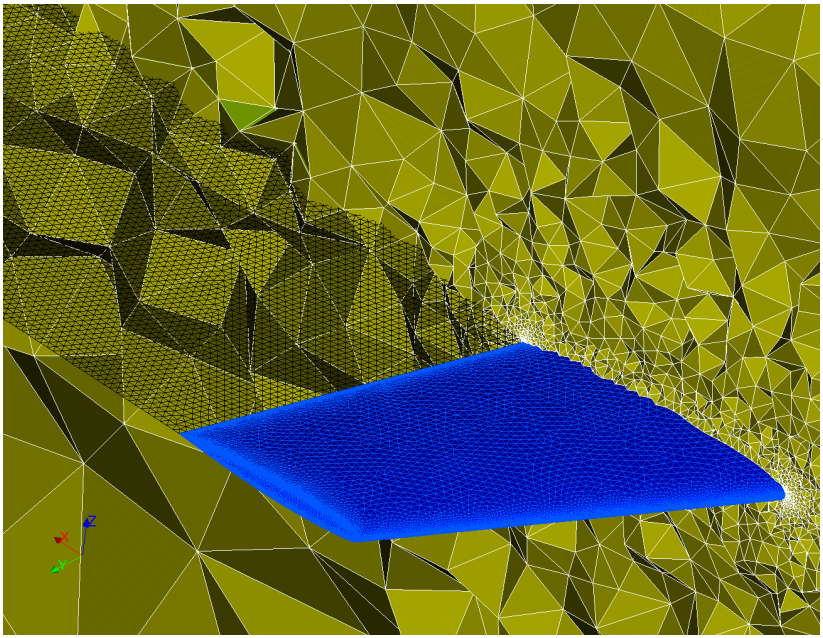

Figure 4.34: ONERA M6 wing mesh.

Figure 4.33 shows the wind tunnel and CAD models. Around the wing's surface, a volumetric domain of 25 m has been generated, which is discretized using a tetrahedral mesh. A minimum element size of 0.002 m is set at the leading and trailing edges and the wingtip. The wing's surface and the domain's volume growth rates are 0.2. Figure 4.34 shows the wing's surface mesh in blue together with a cut of the tetrahedral volume mesh along $\eta = 0.2$ in green. Transparent black triangles indicate the embedded wake surface. The volume mesh has a total of $1.7 \cdot 10^5$ degrees of freedom and $8.7 \cdot 10^5$ elements. The wing's surface mesh has $2.7 \cdot 10^4$ nodes and $5.4 \cdot 10^4$ triangular conditions.

4.8.2 Pressure coefficient validation and verification

Figures 4.35 to 4.38 compare the pressure coefficient distribution, at the sections indicated in Figure 4.32, with the finite volume potential transonic solution from [73], the Reynolds-averaged Navier-Stokes (RANS) reference solution from [74], and the wind tunnel data from [70]. The accuracy of the

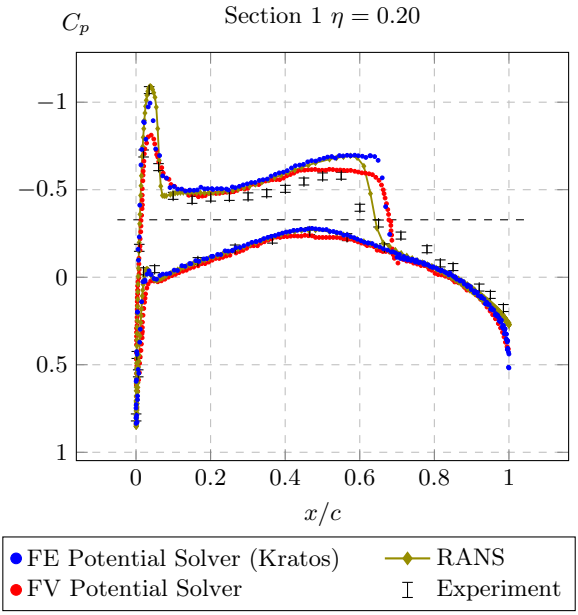

Figure 4.35: Pressure coefficient distribution at different wing sections.

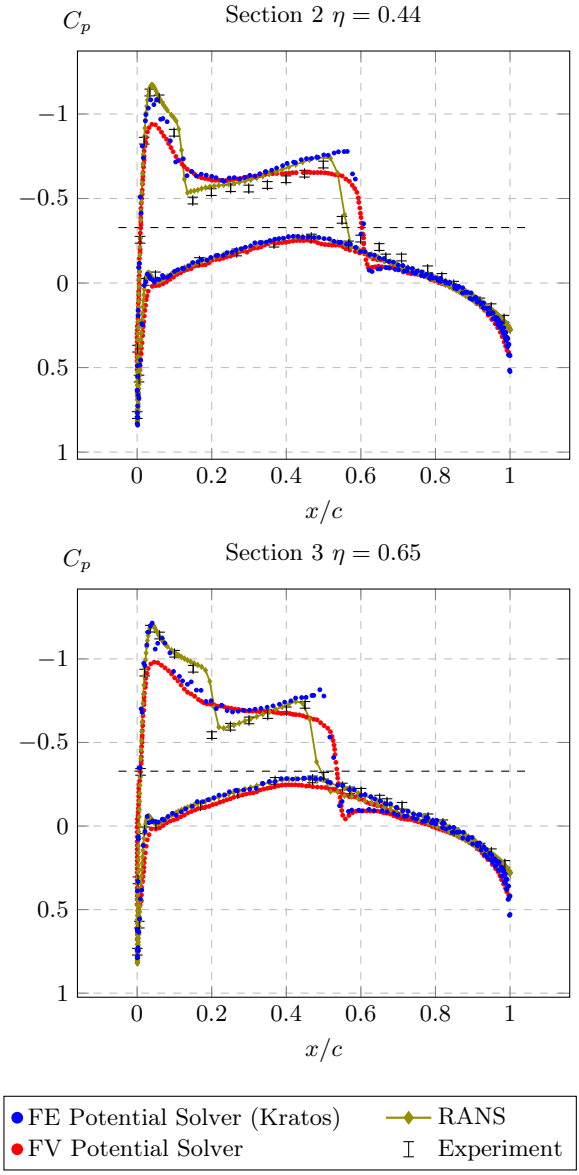

Figure 4.36: Pressure coefficient distribution at different wing sections.

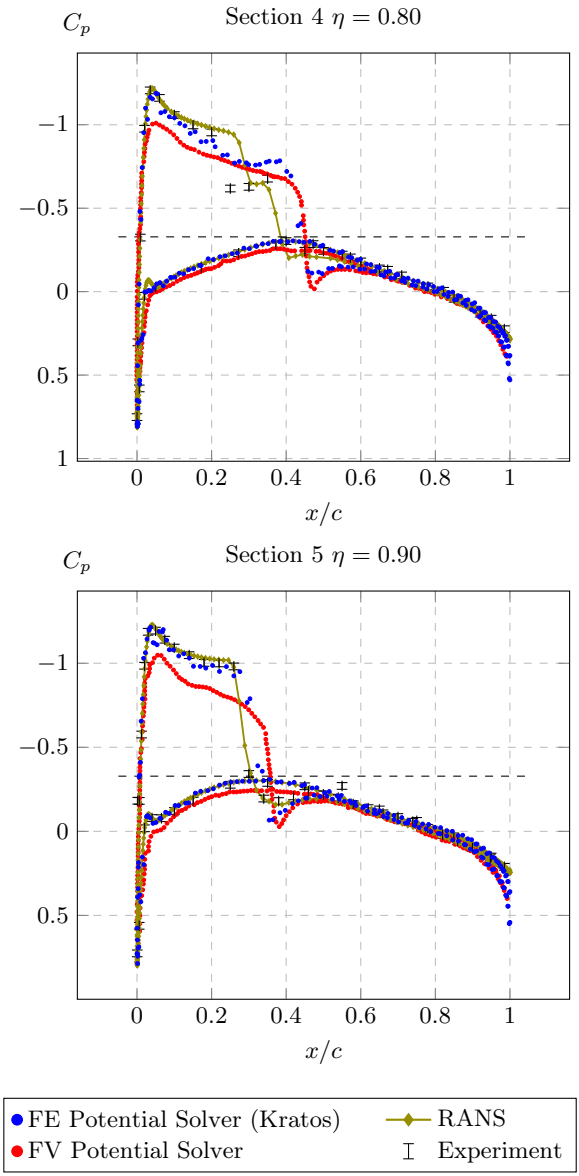

Figure 4.37: Pressure coefficient distribution at different wing sections.

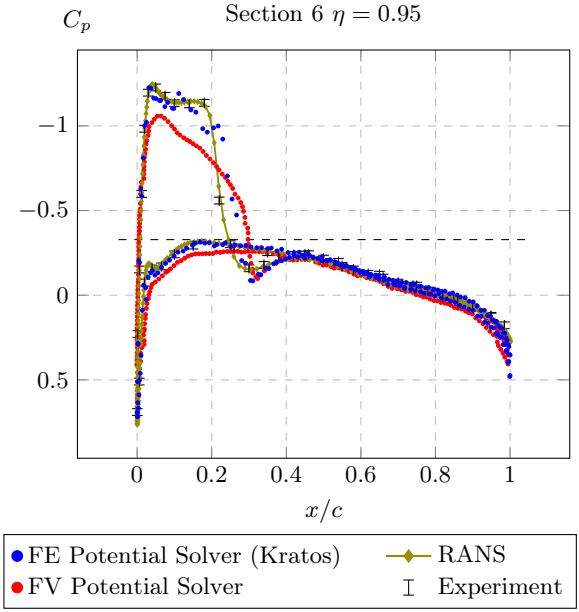

Figure 4.38: Pressure coefficient distribution at different wing sections.

wind tunnel data is +/-0.02. In order to quickly identify the regions where the flow is locally supersonic, the critical pressure coefficient is indicated with a dashed line. All data predict the appearance of a double-shock pattern on the upper surface.

In general, the solution is close to the RANS data, except in the vicinity of the shock wave in sections 1 to 4 (Figures 4.35 to 4.37). In these sections, the computed shock wave position is closer to the other full potential solution, and both full potential solutions predict a shock that is stronger and located after compared to the RANS and wind tunnel data. As a general rule, the RANS solution lays closer to the wind tunnel data than the full potential solutions. In fact, the c_p predicted by RANS matches with the wind tunnel data, except in section 1 (Figure 4.36), where the shock appears to be stronger and after, and in section 4 (Figure 4.37), where RANS predicts the coalescence of the two shocks whereas for the wind tunnel measurements this coalescence happens at a further spanwise location. In sections 5 and 6, the solution predicted by Kratos accurately matches with the RANS and wind tunnel data, even regarding the shock's strength and position. It seems that the other

potential solution has too much artificial dissipation, which would explain why this curve appears below the rest in the supersonic region, and why the shock is not as sharply captured as for the rest of the solutions. Note that the proposed potential solver with an embedded wake approach successfully captures the pressure gradients and the pressure equality condition in the vicinity of the trailing edge.

Step	M_∞	M_{crit}	μ_c
1	0.50	0.95	2.0
2	0.60	0.95	2.0
3	0.70	0.95	2.0
4	0.80	0.95	2.0
5	0.81	0.95	2.0
6	0.82	0.95	2.0
7	0.83	0.95	2.0
8	0.84	0.95	2.0
9	0.84	0.95	1.9
10	0.84	0.95	1.8
11	0.84	0.95	1.7
12	0.84	0.95	1.6

Table 4.13: Load steps required to solve the ONERA M6 case.

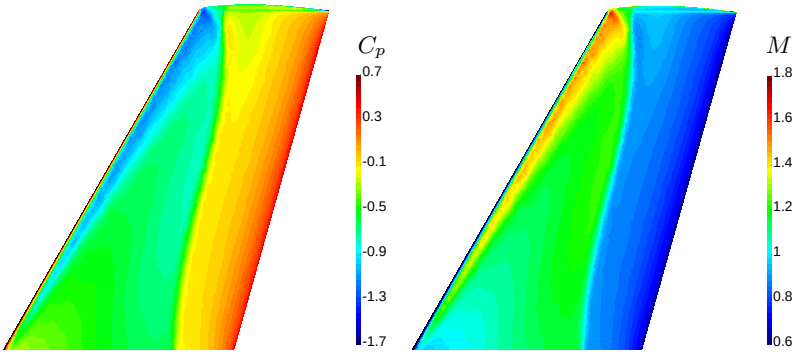

(a) Pressure coefficient. (b) Mach number.

Figure 4.39: Contour plots over ONERA M6.

Onera's validation case is highly nonlinear, Table 4.13 shows the load steps used to achieve convergence. Figure 4.39 presents the pressure coefficient and Mach contour distributions on the wing's upper surface. Both distributions capture the three-dimensional lambda-type shock structure formed by the double-shock pattern on top of the wing.

4.8.3 Aerodynamic loads verification

Crovato et al. provide a rigorous study on the impact of the aerodynamic fidelity level used in preliminary aircraft design [75]. Following their results, the solution obtained with the proposed embedded wake approach is compared to the reference data from five other solvers, including five fidelity levels. Table 4.14 presents the naming convention used to refer to the fidelity levels and the corresponding software packages. The aerodynamic coefficients resulting from the pressure coefficient integration over the wing are given in Table 4.15. The reference point for the computation of the moment coefficient is taken at the root's chord leading edge. Note that Kratos accurately matches the solution predicted by Tranair. In fact, the lift coefficient is the same up to the precision used, and the drag and moment coefficients relative errors lay within 1% and 2%, respectively.

Compared with the other models, the linear inviscid solvers (PAN and NAS) underestimate the lift and moment coefficients. The drag coefficient predicted by Panair is very small because it cannot capture the wave drag. Correcting NAS solution with Euler (NASC) yields results closer to the nonlinear inviscid models. The nonlinear inviscid solvers (TRN, KRATOS, FLO, and SU2) overestimate the lift and moment coefficients and underestimate the drag

Model	Solver	Aerodynamic fidelity level (Equations)
PAN	Panair	Linear Potential
NAS	NASTRAN	Linear Potential
NASC	NASTRAN	Linear Potential corrected by Euler
TRN	Tranair	Full Potential
KRATOS	Kratos	Full Potential with Embedded Wake
FLO	Flow	Full Potential
SU2	SU2	Euler
TRNV	Tranair	Full Potential and Boundary Layer
SU2V	SU2	Reynolds-Averaged Navier-Stokes

Table 4.14: Naming convention [75].

Model	C_L	C_D	C_m
PAN	0.247	0.0047	-0.181
NAS	0.248		-0.181
NASC	0.271		-0.201
TRN	0.288	0.0111	-0.212
KRATOS	0.288	0.0112	-0.208
FLO	0.294	0.0110	-0.217
SU2	0.286	0.0130	-0.212
TRNV	0.255	0.0161	-0.181
SU2V	0.272	0.0181	-0.196

Table 4.15: Aerodynamic coefficients obtained with different levels of fidelity for the Onera M6 wing ($\alpha = 3.06°$, $M_\infty = 0.84$) [75].

coefficient compared to the viscous solvers (TRNV and SU2V) because they do not solve the boundary layer, which changes the pressure coefficient distribution and includes the skin friction drag effect.

4.8.4 Performance comparison

In order to compare the computational cost of the proposed approach with other solvers, the wall-clock and CPU times required to obtain the solutions presented in Section 4.8.3 are given in Table 4.16 along with the mesh sizes. Kratos was run in serial in a desktop machine fitted with an Intel Xeon E5-1650 processor (3.5 GHz), SU2 was run on a cluster with Intel Xeon X5650 processors (2.7 GHz), and the rest of the solvers were run in serial on a laptop equipped with an Intel Core i7-7700HQ processor (2.8GHz). According to Table 4.16, KRATOS performs slightly faster than FLO and slightly slower than TRN. Note that the comparison is not completely fair since the solvers were run in different machines. However, this comparison allows assessing that the time required by KRATOS, TRN, and FLOW is of the same order of magnitude. This shows that the capability of embedding the wake does not come at the cost of increasing the computational time nor losing accuracy.

Table 4.16 shows that the linear inviscid solvers provide a much faster solution compared to the other solvers. This is because they only solve a comparatively small linear system of equations once, whereas the nonlinear inviscid solvers require finer meshes and several Newton iterations. The highest fidelity solvers (SU2 and SU2V) need more time because they have more degrees of freedom per cell (corresponding to the 5 and 6 equations models) compared

Model	n. Cells [1]	n. Threads	Wall-Clock Time	CPU Time
PAN	$1.0 \cdot 10^3$	1	10 s	10 s
NAS	$5.0 \cdot 10^2$	1	20 s	20 s
NASC	$5.0 \cdot 10^2$	1	20 s	20 s
TRN	$5.0 \cdot 10^5$	1	7 min	7 min
KRATOS	$8.7 \cdot 10^5$	1	10 min	10 min
FLO	$5.9 \cdot 10^5$	1	13 min	13 min
SU2	$5.1 \cdot 10^5$	12	14 min	3 h
TRNV	$5.0 \cdot 10^5$	1	15 min	15 min
SU2V	$1.5 \cdot 10^6$	36	24 h	36 d

Table 4.16: Models mesh size and computational time [75].

to the potential solvers, which only solve for one degree of freedom per cell (corresponding to the scalar potential equation).

4.8.5 Wake potential jump condition and wingtip vortex

Figure 4.40 shows the potential jump contour plot over the wake surface. Note that the potential jump is constant along the freestream sheet streamlines, which means that Eq. (3.44) is applied correctly with the proposed embedded wake approach. This result is also shown in Figure 4.41, where the potential jump at the trailing edge and the intersection between the wake and a Trefftz plane positioned at the outlet is plotted over the dimensionless spanwise location. The largest disagreements occur in the vicinity of the wake tips at the outlet, where the mesh is too coarse and cannot capture the largest solution gradients. As the potential jump tends to zero towards the wake tips, the error introduced by the lack of conformity between elements can be

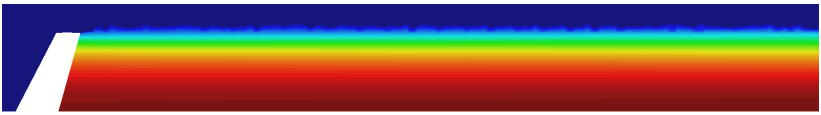

Figure 4.40: Potential jump contour plot over the wake surface.

[1] For Kratos it is number of elements.

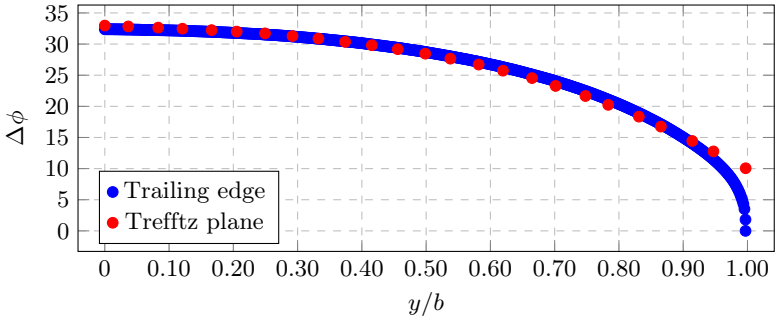

Figure 4.41: Potential jump spanwise distribution.

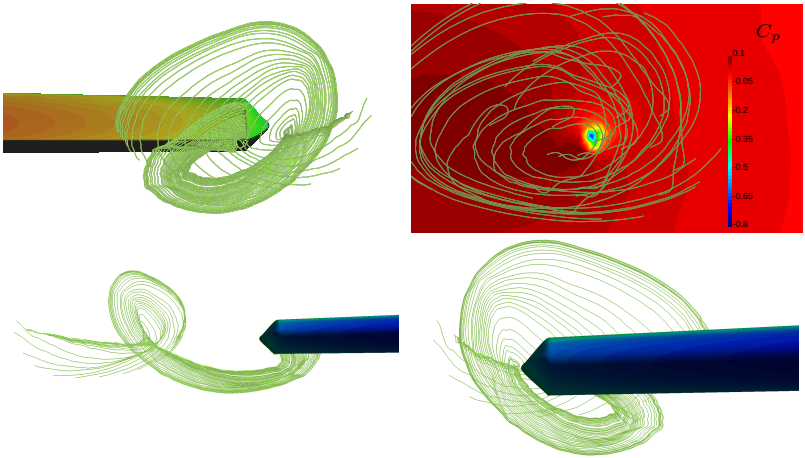

Figure 4.42: Wingtip vortex behind the ONERA M6 wing rolling up from the trailed vorticity sheet.

neglected.

Four different perspectives of the wingtip vortex behind the ONERA M6 wing are shown in Figure 4.42 to demonstrate that the proposed embedded wake approach can also capture the wingtip vortices. The top right figure also shows the pressure coefficient contour plot at the plane $x = 1.2\,\mathrm{m}$, where the low-pressure core of the vortex can be identified. This low-pressure core is related to the high-speed spin reached in the vortex center.

4.9 NASA Common Research Model transonic validation and verification case

The Common Research Model (CRM) is a modern commercial aircraft geometry that was developed in a joint effort between Boeing and NASA to assess the state of the art in CFD [76]. The CRM was developed in the context of the Drag Prediction Workshops (DPW) initiated by the American Institute of Aeronautics and Astronautics (AIAA) Applied Aerodynamics Technical Committee [77]. In order to enable the widest cooperation, the geometries under study as well as experimental and numerical data for validation and verification are open source and can be found in the DPW, and the CRM official websites [78]. The CRM was selected in the context of this thesis in order to validate the proposed embedded wake approach for an industrial size full aircraft configuration under transonic conditions and to verify that the method works for multiple lifting surfaces and trailing wakes. It was also of interest to investigate whether the method works on blunt and curved trailing edges. In this section the wing/body/horizontal-tail (WBH) configuration used in the 4th AIAA CFD DPW is considered [79]. Unless otherwise stated, the following results were obtained for an angle of attack of $\alpha = 2.31°$ and a freestream Mach number of $M_\infty = 0.85$ for comparison purposes with the RANS reference data provided in [80].

4.9.1 Model description

The detailed aerodynamic design of the CRM was developed by the Boeing Company, whereas the model design, fabrication, and wind tunnel testing of the CRM were undertaken by NASA's Subsonic Fixed Wing Project within the Fundamental Aerodynamics Program. Figure 4.43 shows CRM's CAD model and Figure 4.44 shows a photo of the wind tunnel model in the National Transonic Facility (NTF). Note that since the WBH configuration has two lifting surfaces, two trailing wakes must be taken into account. Figure 4.45 illustrates the trailing wakes behind the wing and the horizontal stabilizer.

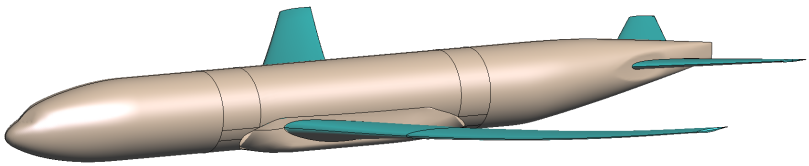

Figure 4.43: CAD model of the CRM.

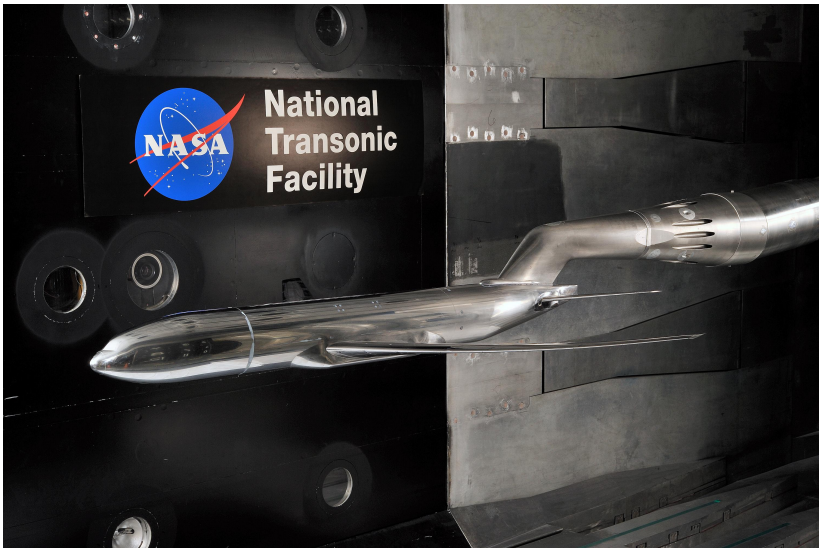

Figure 4.44: CRM in the National Transonic Facility [81].

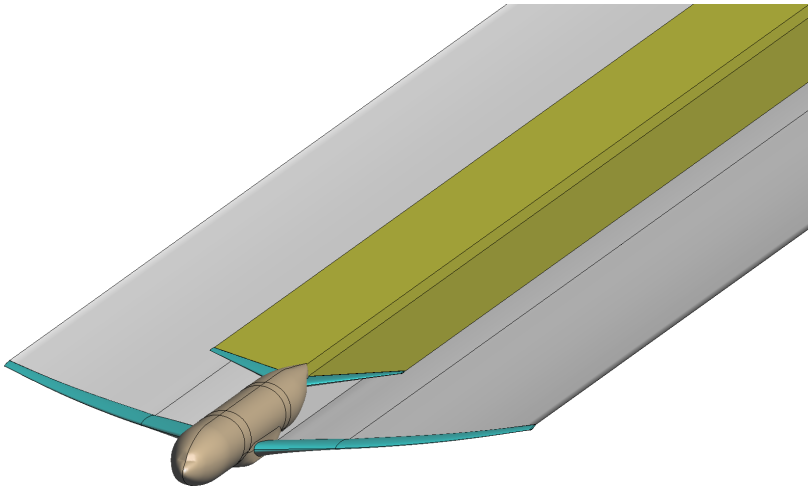

Figure 4.45: The WBH CRM configuration has two trailing wakes.

The CRM was designed to fly at a cruise Mach number of $M_\infty = 0.85$ and a lift coefficient of $C_L = 0.5$. Figure 4.46 shows the CRM planform dimensions and illustrates the yehudi break at 37% of the semispan. It also indicates the spanwise position of the sections where the pressure coefficient distribution will be monitored in the following sections. The reference quantities of the full-scale model are presented in Table 4.17. Details about airfoil information at the wing's 21 defining stations are provided in [76]. As described in [76],

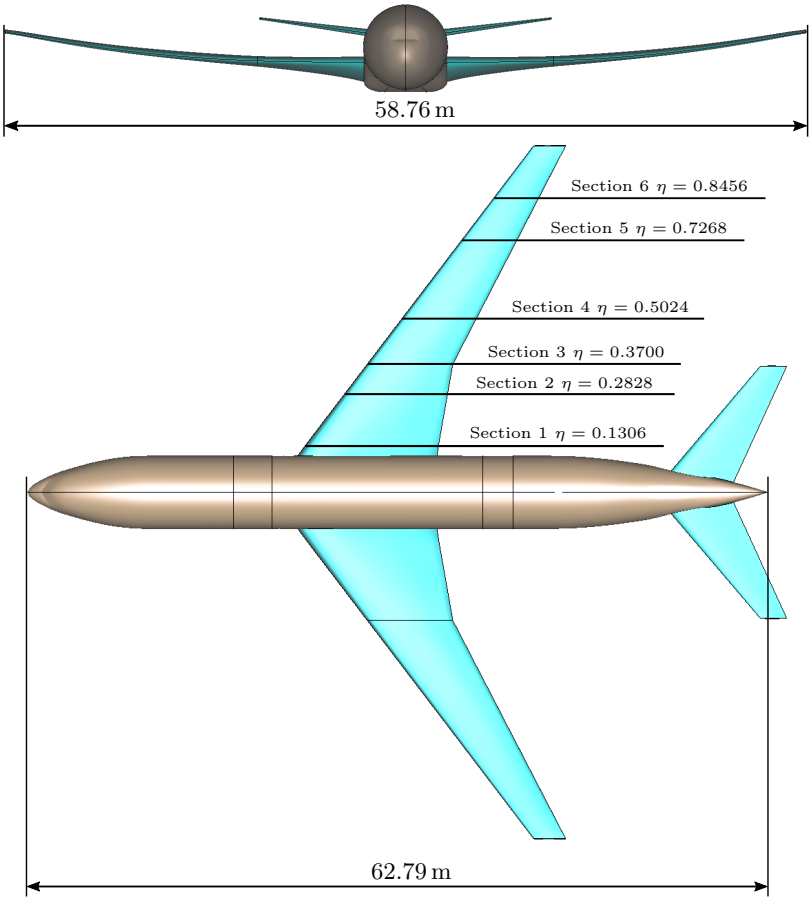

Figure 4.46: CRM planform dimensions.

Parameter	Value
Reference area A_{ref}	$383.69\,\text{m}^2$
Span b	$58.76\,\text{m}$
Mean aerodynamic chord $\bar{c}$	$7.00\,\text{m}$
Taper ratio λ	0.275
Leading edge sweep φ	35.0°
Aspect ratio Λ	9.0

Table 4.17: Reference quantities of the CRM [76].

the contemporary transonic supercritical wing was designed to have high performance for both configurations: with and without the nacelle/pylon group. The wing's design was achieved using SYN107 to optimize the wing taking the fuselage's effect into account. SYN107 is a wing/body Navier-Stokes code for analysis and design developed by Jameson [82]. The wing has a blunt trailing edge to allow for a minimum-gauge fabrication constraint. Further details about the wing's geometry such as maximum thickness, maximum camber and twist distributions can be found in [76].

The horizontal stabilizer was sized following characteristic control and stability specifications and was designed for dive Mach number conditions. The parameters describing its planform are presented in Table 4.18. The tail is defined by two symmetric airfoil sections, a 10%-thick section at the symmetry plane, and an 8%-thick airfoil at the tip. The fuselage is typical of a wide/body commercial aircraft. It includes a wing-body fairing and a scrubbing seal for the horizontal stabilizer.

Parameter	Value
Area A	$92.90\,\text{m}^2$
Span b	$21.34\,\text{m}$
Mean aerodynamic chord $\bar{c}$	$4.70\,\text{m}$
Taper ratio λ	0.35
Quarter-chord sweep φ_{25}	37.0°
Aspect ratio Λ	4.90

Table 4.18: Parameters describing the horizontal stabilizer's planform [76].

For the purpose of this study, the CAD geometry was downloaded directly from the 4th AIAA CFD DPW official website [79]. The downloaded CAD contained several holes between the surfaces that were closed using GiD [83]. Exploiting the symmetry of the geometry and boundary conditions, only half of the aircraft was modelled. Based on the domain size studies presented in Section 4.1.4, a volumetric domain of 1000 m was generated around the vehicle.

4.9.2 Mesh refinement study

In order to study the sensitivity of the solution with respect to the mesh size, a mesh refinement study is presented. The meshes were first generated using Salome and they were then automatically refined towards the wake using a metric-based technique. Table 4.19 presents the mesh information for each refinement level before and after the wake refinement. Note that the wake refinement involves adding approximately the same number of nodes and elements for each refinement level, namely about 726,000 nodes and 4,320,000 elements.

Figure 4.47 shows a side view of the finest mesh generated in Salome before the wake refinement. The clip of the tetrahedral volume mesh is indicated in light red, the model's surface mesh is indicated in grey, and the mesh used for the wing and tail wakes are indicated in light yellow and blue, respectively. The tetrahedral volume mesh was achieved using the NETGEN algorithm allowing for a maximum element size of 50 m in the far-field and using an element growth rate of 0.2. The triangular surface meshes were also generated with the NETGEN algorithm. The minimum element size was set at the wingtips and the leading and trailing edges, and is denoted as h in Table 4.19. The maximum element sizes at the wing and tail surfaces were set to 0.1 m (but for the very coarse grid, where they were set at 0.16 m). The maximum element size at the fuselage was set to 0.25 m.

		CRM surface mesh		Volume mesh before/after wake refinement			
				Before refinement		After refinement	
Mesh label	h [m]	Nodes	Triangles	Nodes	Tetrahedra	Nodes	Tetrahedra
Very coarse	0.16	29,726	58,928	142,769	736,658	869,255	5,061,239
Coarse	0.08	65,957	131,390	300,847	1,562,546	1,026,420	5,881,704
Medium	0.04	76,135	151,746	349,563	1,817,714	1,077,844	6,152,143
Fine	0.02	109,044	217,564	514,495	2,689,007	1,240,153	7,008,497
Very fine	0.01	173,046	345,568	828,145	4,345,664	1,554,135	8,667,159

Table 4.19: Mesh sequence used for the convergence study.

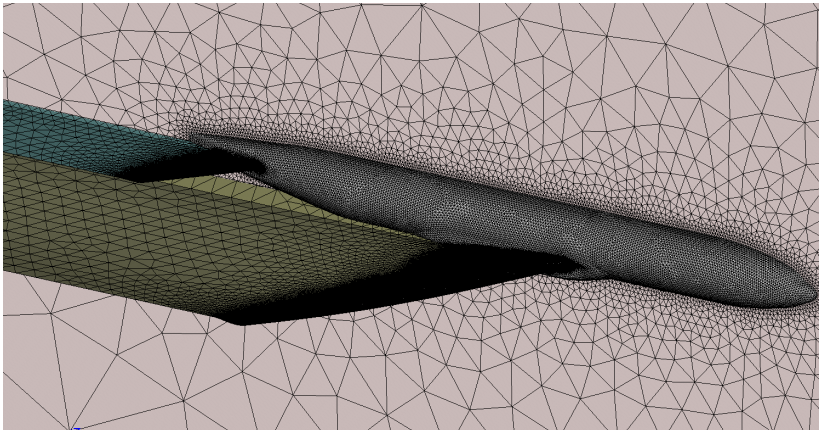

Figure 4.47: CRM surface and volume mesh including wake (h = 0.01 m).

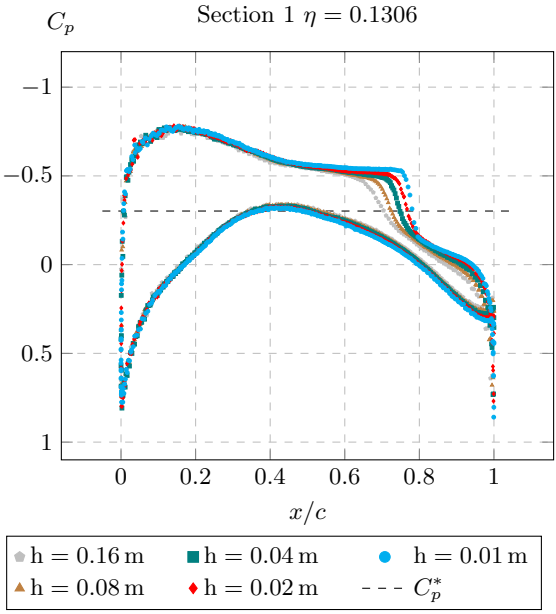

Figure 4.48: Pressure coefficient distribution convergence.

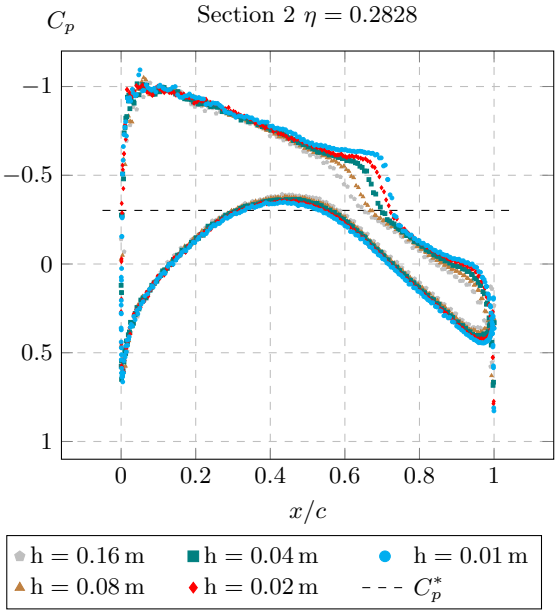

Figure 4.49: Pressure coefficient distribution convergence.

The resulting pressure coefficient distribution is presented in Figures 4.48 and 4.49 at two wing sections for each refinement level. In order to stop the Newton Raphson iterations, a tolerance of 10^{-8} for the residual L_2 norm was set as a convergence criteria. The critical pressure coefficient is indicated with a dashed line. The largest sensitivity of the solution occurs in the vicinity of the shock wave. Lower mesh resolutions predict the shock wave to be further upstream. The finest grid was selected for the subsequent sections.

4.9.3 Pressure coefficient validation and verification

To validate and verify the proposed method, the resulting pressure coefficient distribution is compared with RANS and wind tunnel reference data at six different wing sections along the span. The comparison is presented in Figures 4.50 to 4.52. The RANS data corresponds to the CFL3D results presented in [80, 84], and the wind tunnel measurements are presented in [85]. There is no wind tunnel data for section 3. As in the other examples, the proposed method accurately matches with the RANS data in most of

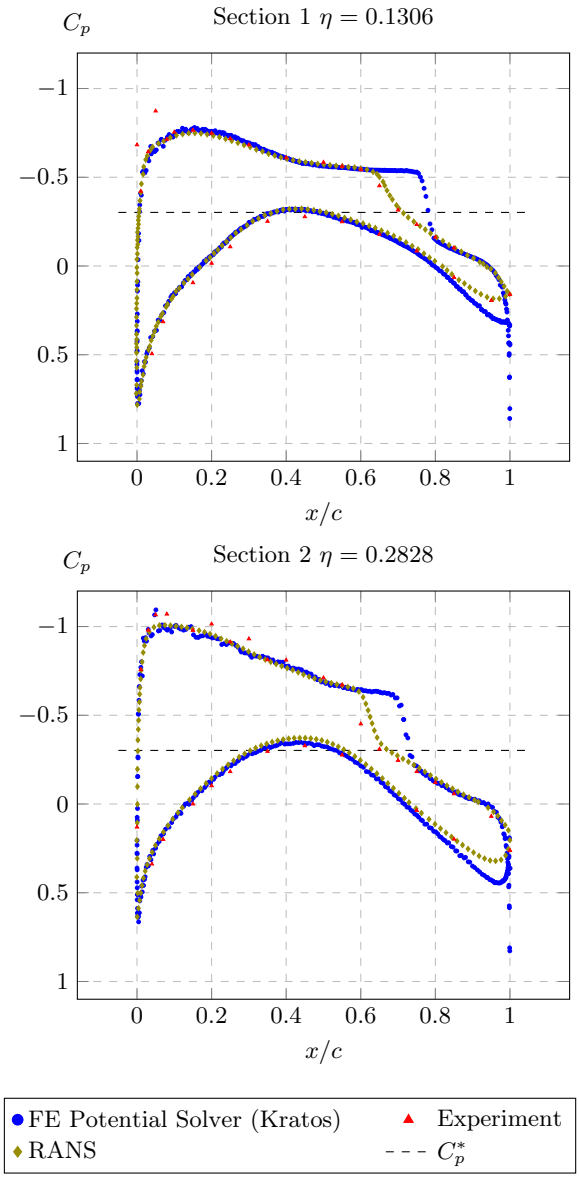

Figure 4.50: Pressure coefficient distribution at different wing sections.

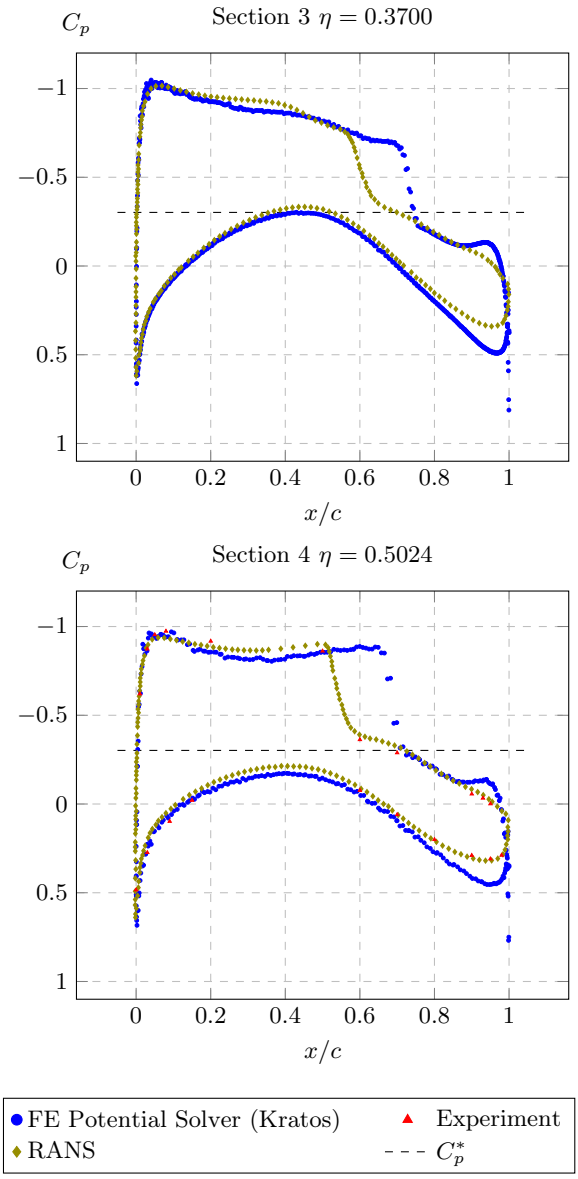

Figure 4.51: Pressure coefficient distribution at different wing sections.

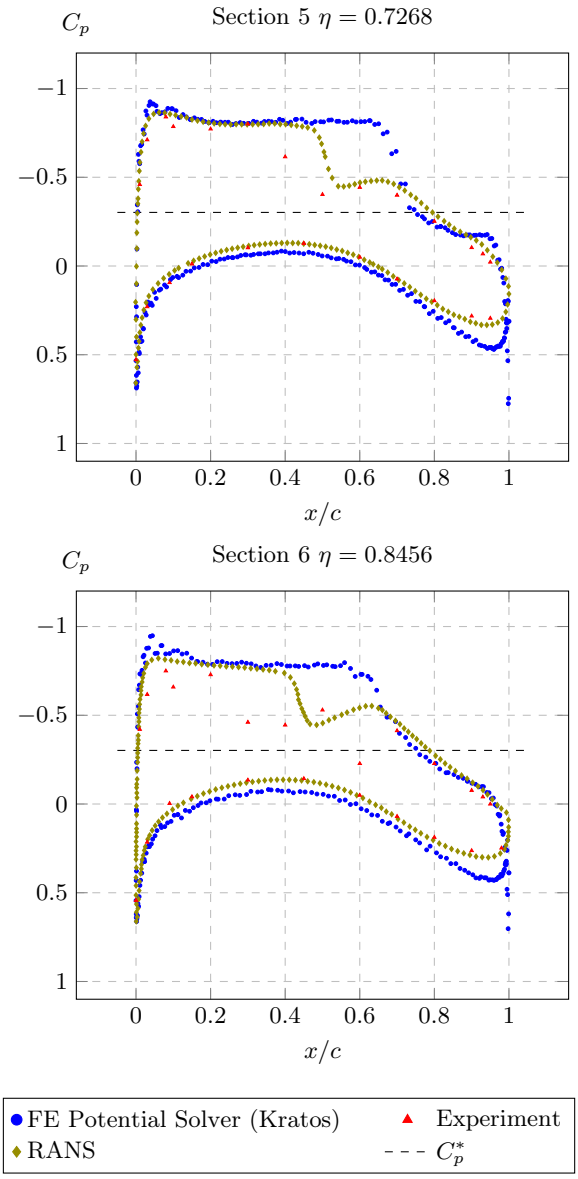

Figure 4.52: Pressure coefficient distribution at different wing sections.

the domain. The largest discrepancies occur close to the shock wave and the trailing edge. As expected, the full-potential solver predicts the position of the shock wave further downstream compared to RANS and the experiments. The differences at the trailing edge are associated with the fact that the potential solver cannot predict the separation at the blunt trailing edge. Instead, the potential solver enforces the wake boundary conditions, leading to an overestimation of the pressure coefficient. The discrepancies between the RANS and wind tunnel data are related to the effects of the model support system and the static aeroelastic deformation presented in [86].

4.9.4 Aerodynamic loads validation and verification

The aerodynamic loads obtained with the proposed FPS are compared with RANS and wind tunnel reference data in Table 4.20. The RANS data corresponds to the CFL3D results presented in [80, 84] and the statistical analysis of continuum data presented in the 4th DPW [87]. The NTF wind tunnel data is also presented in [87]. For comparison purposes, the same angle of attack as the one obtained with CFL3D is used. As expected and as for the Onera M6 wing validation case, the full-potential solver overestimates the value of the lift coefficient compared to the reference data. This result can be explained by looking at the pressure coefficient distributions presented in the previous section (see Figures 4.50 to 4.52). Since the FPS predicts the shock wave's position on the upper surface further downstream compared to the RANS solution, the area enclosed by the pressure distribution curve and thus the lift coefficient are larger for FPS than for RANS. Opposingly, the total drag coefficient C_D is underestimated and the skin-friction drag coefficient is

Model		α	C_L	C_D	C_{Dpr}	C_{Dsf}	C_m
KRATOS	FPS	2.31°	0.568	0.0137	0.0137	0.0	-0.060
CFL3D [80]	RANS	2.31°	0.500	0.0267	0.0140	0.0127	-0.039
NTF wind tunnel [87]		3.02°	0.500	0.0272	-	-	+0.038
4th DPW	RANS	4th DPW statistical analysis of continuum data [87]					
Average		2.34°	0.500	0.0270	0.0147	0.0123	-0.040
σ		0.097°	-	0.0008	0.0008	0.0005	0.016
$Avg + \sigma$		2.44°	-	0.0278	0.0155	0.0128	-0.024
$Avg - \sigma$		2.24°	-	0.0262	0.0139	0.0119	-0.056
$\frac{\sigma}{\lvert Avg \rvert}$		0.04	-	0.0300	0.0564	0.0381	0.400

Table 4.20: CRM aerodynamic coefficients ($M_\infty = 0.85$). Comparison between different models [80, 87].

zero because the potential solver cannot capture the viscous effects. However, the predicted drag pressure coefficient C_{Dpr} accurately matches the reference data, being only four counts apart from the CFL3D result and ten counts from the 4th DPW average value. Regarding the pitching moment coefficient C_m, even though the obtained value underestimates the reference value obtained with CFL3D, it lies close to the 4th DPW lower bound determined by the pitching moment coefficient average value minus one standard deviation. The fact is that in the 4th DPW a large spread among the pitching moment coefficient values obtained with different RANS solvers and a large discrepancy between numerical and experimental data were found [87]. As mentioned in the previous section, the discrepancies between the RANS and wind tunnel data are attributed to the effects of the model support system and the static aeroelastic deformation presented in [86].

4.9.5 Potential jump across embedded wakes

Figure 4.53 presents the resulting velocity potential contour plot on the aircraft's surface and the symmetry plane. The proposed method is capable of capturing the jump in the potential across both embedded wakes. Note that the jump is also captured at the intersection between the wake and the fuselage. This shows the substantial benefit of using the proposed embedded wake approach, where the wake does not need to be explicitly represented in the mesh.

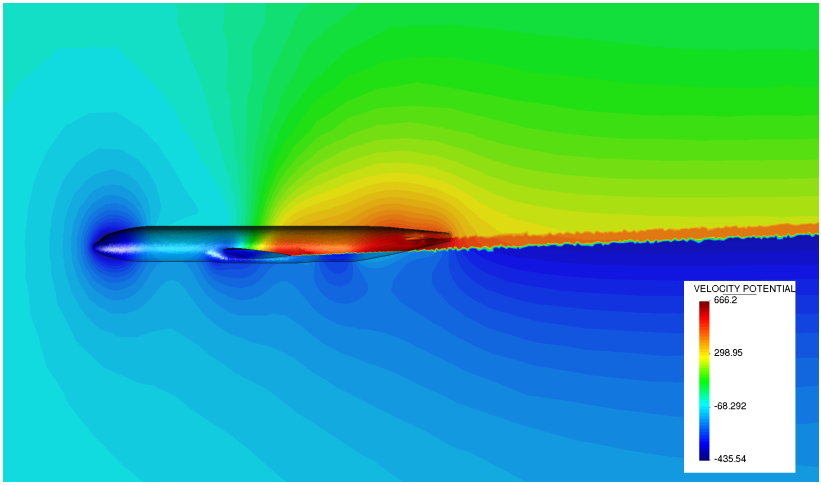

Figure 4.53: Potential jump across the embedded wakes.

Upper surface

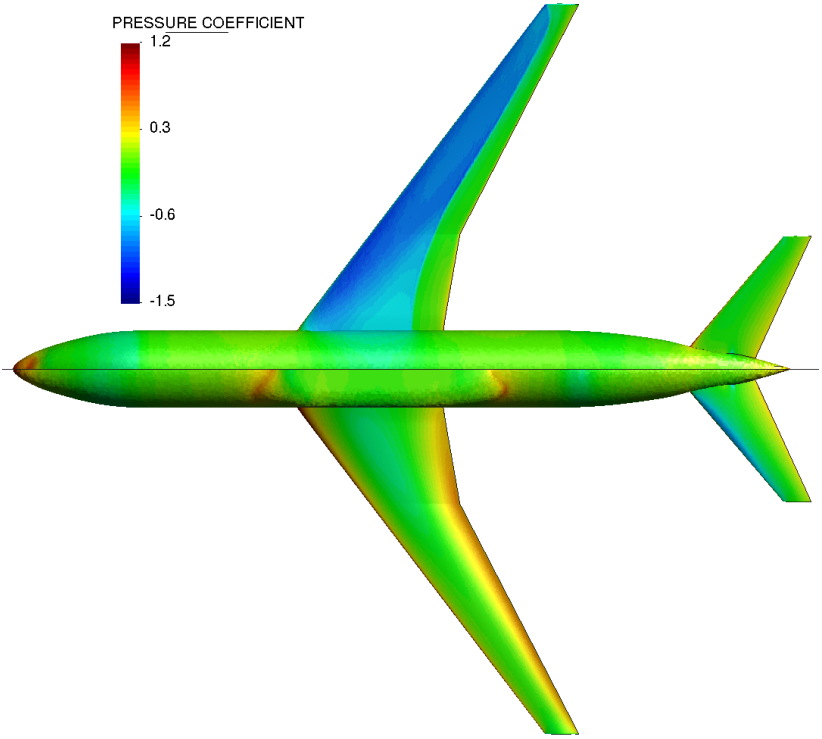

Lower surface

Figure 4.54: Isobars of the CRM wing/body/horizontal-tail ($\alpha = 2.31°$, $M_\infty = 0.85$).

Upper surface

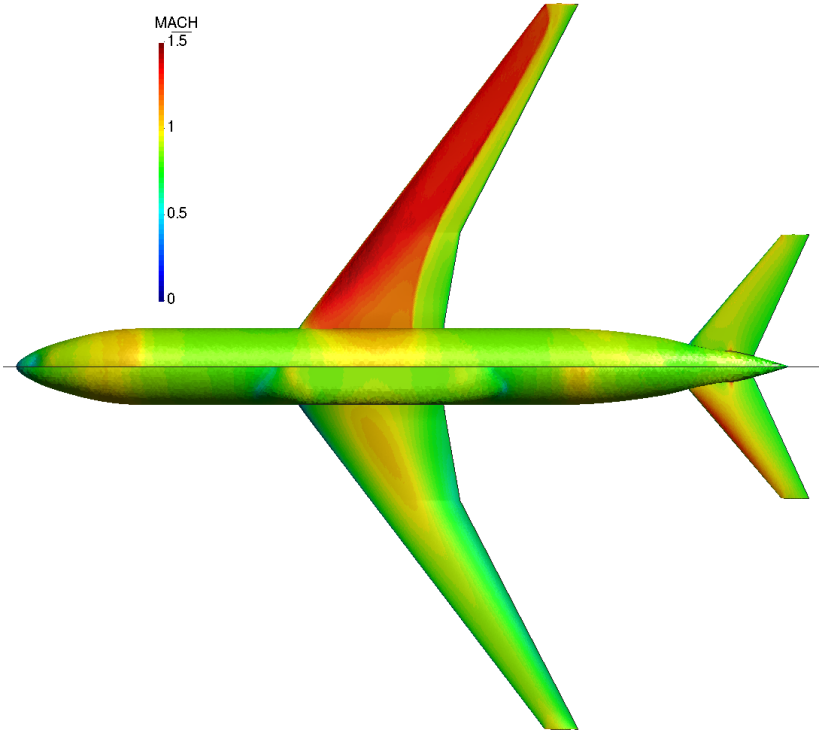

Lower surface

Figure 4.55: Local Mach number contour plot ($\alpha = 2.31°$, $M_\infty = 0.85$).

4.9.6 Contour plots and wingtip vortices

Figures 4.54 and 4.55 provide the upper and lower surface pressure coefficient and the local Mach number contour plots, respectively. The upper-surface shock system is swept along constant x/c in the mid-span area, reducing strength on the outboard. This behavior can also be observed in the detailed pressure coefficient distributions presented in the previously in Figures 4.50 to 4.52. These results are qualitatively in accordance with the findings reported in [87]. Figure 4.56 presents the resulting streamlines forming the wingtip vortices.

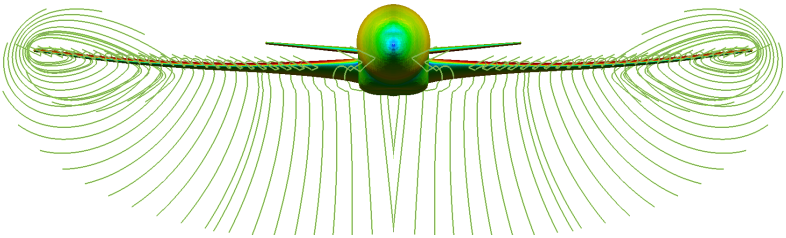

Figure 4.56: Wingtip vortices behind the CRM ($\alpha = 2.31°$, $M_\infty = 0.85$).

4.9.7 Nacelle-pylon effect

In order to show that the proposed solver can be used for more complex configurations, this section presents the effects of installing the nacelle/pylon (NP) group. A similar study is presented in [76] without the horizontal-tail. Figure 4.57 shows the full CRM wing/body/nacelle/pylon/horizontal-tail

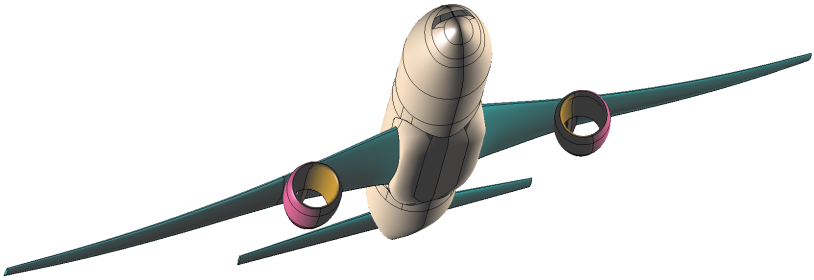

Figure 4.57: CRM wing/body/nacelle/pylon/horizontal-tail CAD model.

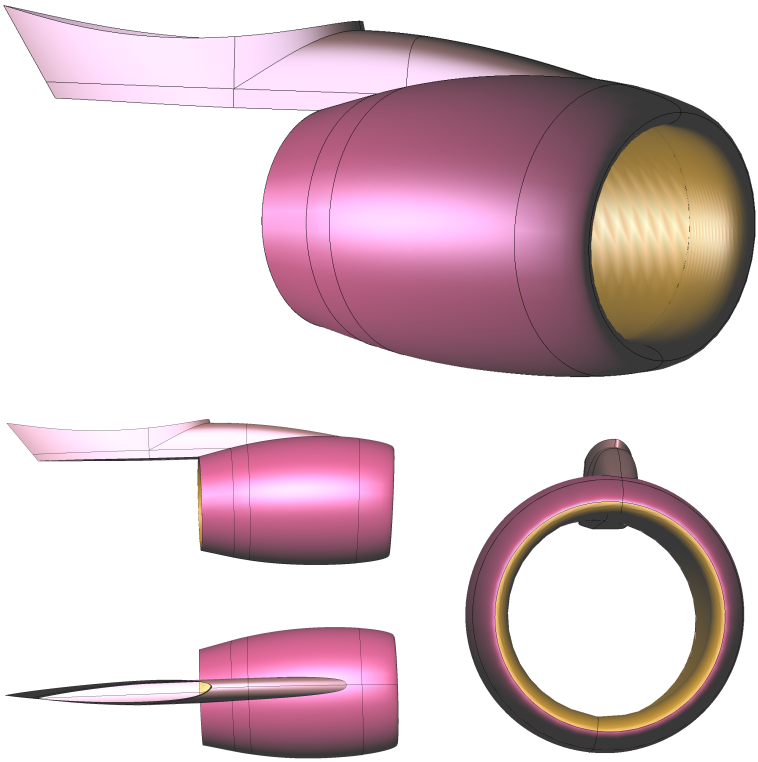

Figure 4.58: Large-diameter flow-through nacelle and pylon CAD models.

configuration and Figure 4.58 presents a detailed view of the NP group's CAD model. The CRM nacelle's design consists of a single-cowl, high by-pass ratio, flow-through concept. The exit area has been sized to achieve a natural, unforced mass-flow-ratio representative of commercial aircraft engines at cruise [76]. The nacelle/pylon (NP) group is located at $y = 9.67\,\mathrm{m}$ ($\eta = 0.33$) and has been meshed using an element size of $0.05\,\mathrm{m}$. Figure 4.59 shows the surface mesh as well as the volume mesh surrounding the nacelle.

Table 4.21 presents a comparison of the lift and drag coefficients between both configurations. The addition of the NP group yields a decrease in lift and an increase in drag. These trends are the same as the ones measured in the NTF as reported in [81]. The comparison between the pressure coefficient distribution

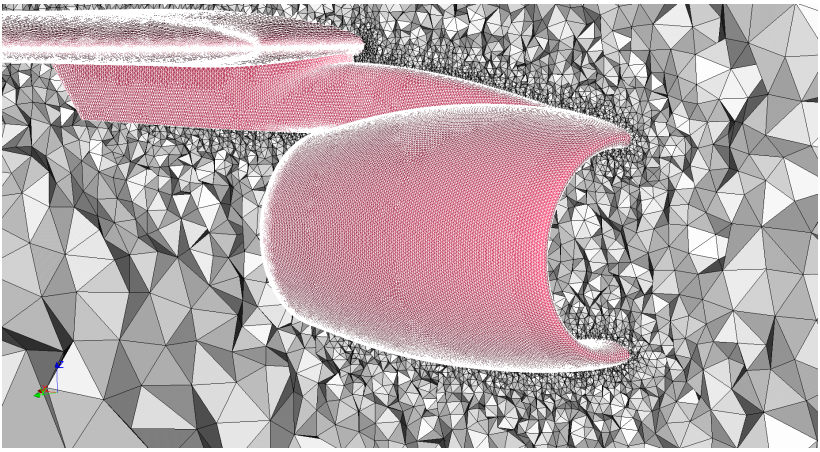

Figure 4.59: Nacelle and pylon mesh.

Configuration	C_L	C_{Dpr}
WBH	0.5117	0.0107
WBNPH	0.4850	0.0189

Table 4.21: CRM aerodynamic coefficients obtained with the proposed solver ($\alpha = 2.0°$ and $M_\infty = 0.85$). Nacelle-pylon effect.

of the wing/body/horizontal-tail (WBH) and the wing/body/nacelle/pylon/-tail (WBNPH) configuration is presented in Figures 4.60 to 4.64 for an angle of attack of $\alpha = 2.0°$ and a freestream Mach number of $M_\infty = 0.85$. Note that the NP group is located between sections 2 and 3. Consequently, the resulting pressure coefficient distributions show that the largest effect induced by the NP group occurs in the inboard section (Sections 1, 2 and 3 in Figures 4.60 and 4.61), especially on the lower surface at section 2. In this section, the NP group leads to flow acceleration, which results in the development of a shock wave on the lower surface (see Figure 4.61). The outboard sections (4, 5 and 6) are less affected by the inclusion of the NP group, decreasing its effect with increasing spanwise position. These findings are in accordance with the comparison between WB and WBNP presented in [76].

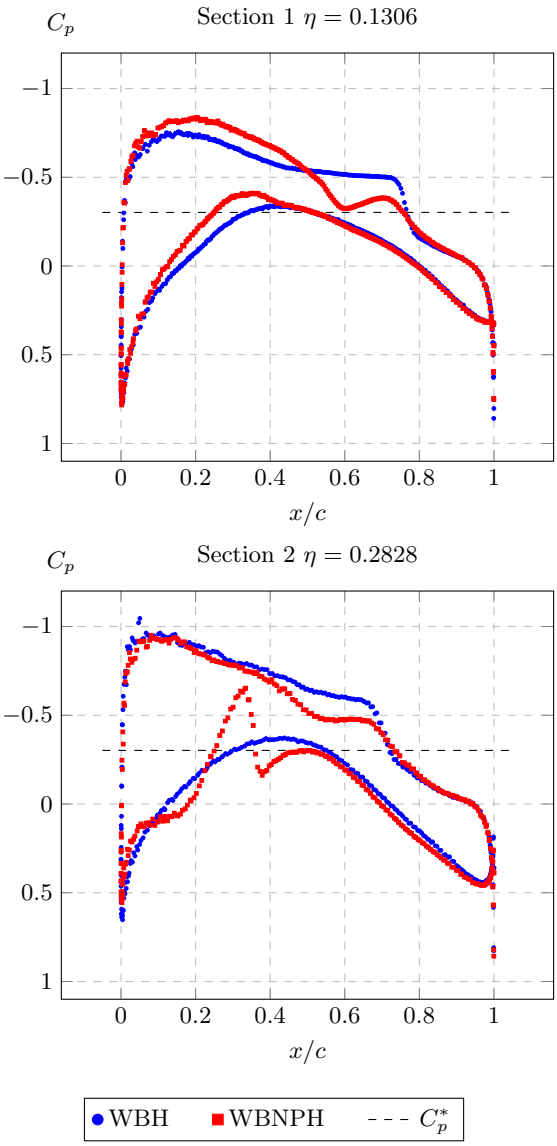

Figure 4.60: Pressure coefficient distribution at different wing sections ($\alpha = 2.31°$, $M_\infty = 0.85$).

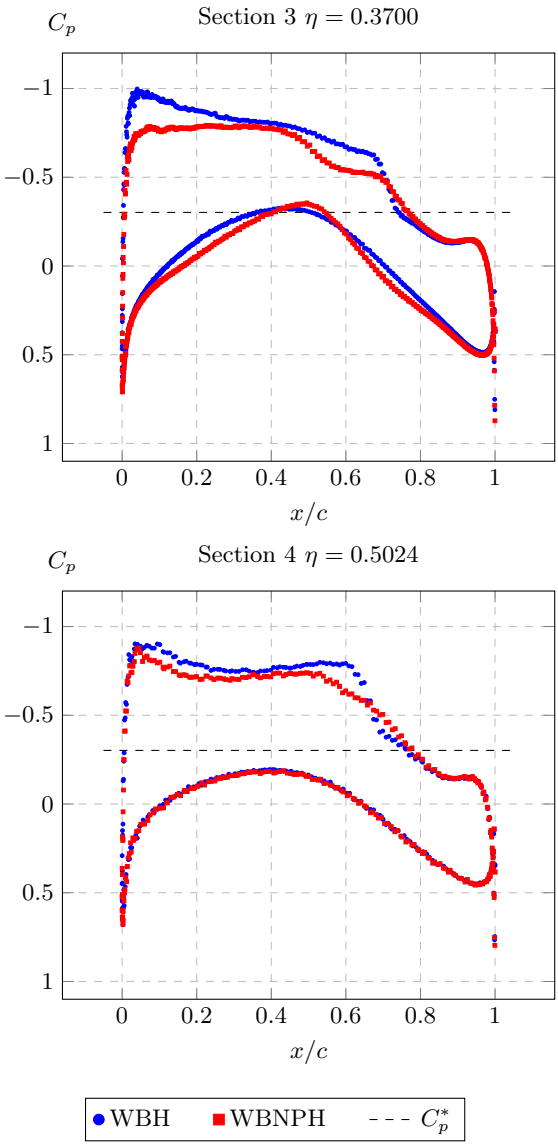

Figure 4.61: Pressure coefficient distribution at different wing sections ($\alpha = 2.31°$, $M_\infty = 0.85$).

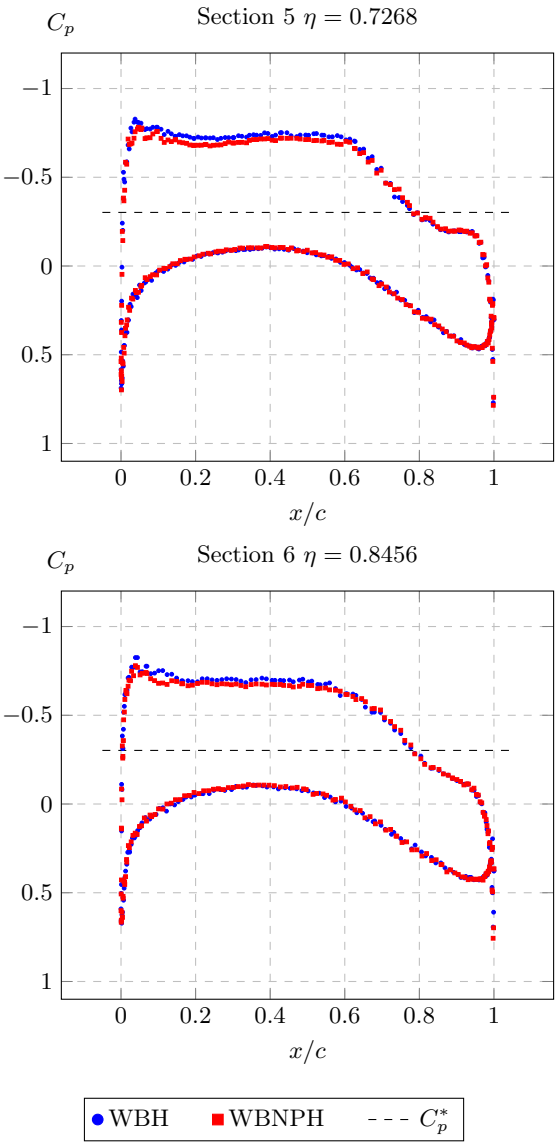

Figure 4.62: Pressure coefficient distribution at different wing sections ($\alpha = 2.31°$, $M_\infty = 0.85$).

Wing/body/horizontal-tail

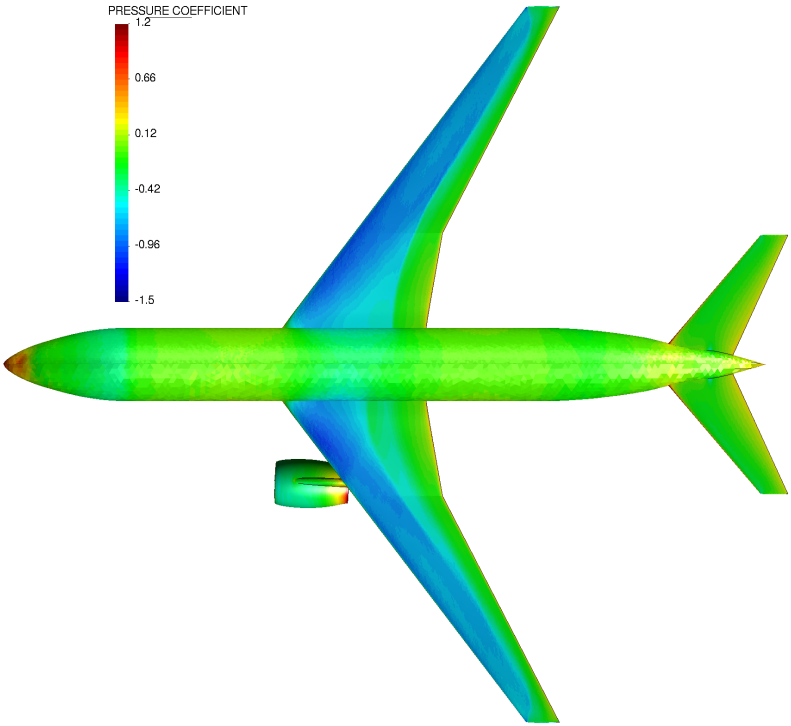

Wing/body/nacelle/pylon/horizontal-tail

Figure 4.63: Nacelle-pylon effect on wing upper surface isobars.

Wing/body/horizontal-tail

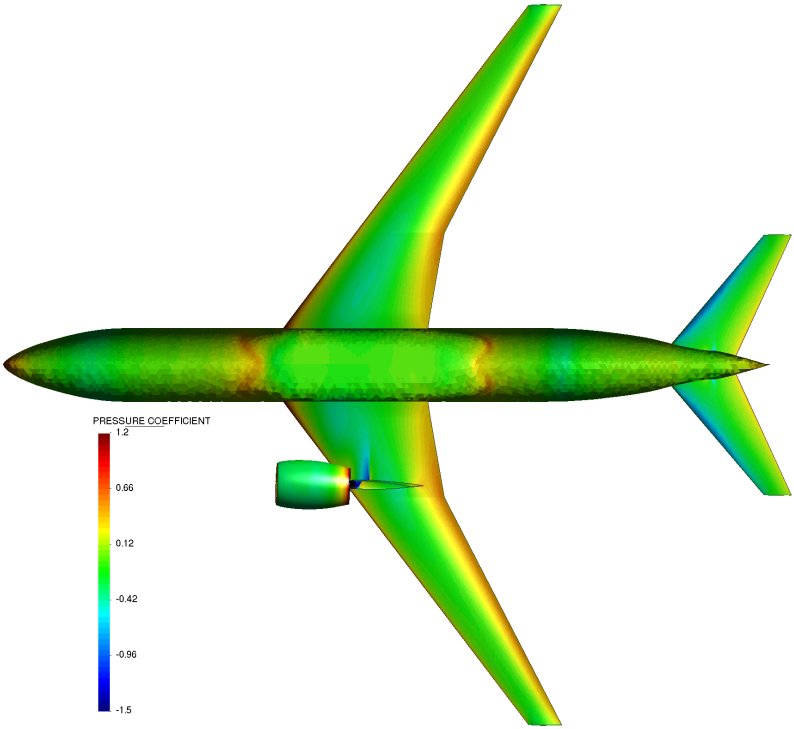

Wing/body/nacelle/pylon/horizontal-tail

Figure 4.64: Nacelle-pylon effect on wing lower surface isobars.

Chapter 5

Conclusions

5.1 Summary

This dissertation presents an embedded wake method for potential transonic solvers. The method works both in two and three dimensions. The solver is intended to be used in the context of multidisciplinary optimization at the early stages of aircraft design, where fast, fluid solutions are required due to the large number of fluid evaluations involved. To this end, the finite-element method is utilized to discretize the flow field. Unstructured meshes are employed to simplify the handling of complex geometries. The idea of using an embedded wake approach is motivated by the difficulties stemming from explicitly representing the wake within the mesh that have been reported in previous publications and that are introduced in Section 1.1. The proposed method resolves the full-potential equation, the lowest fidelity fluid model capable of capturing transonic effects without assuming slender bodies. This method can also be used to initialize the flow field and speed up the convergence of higher fidelity solvers.

A brief review of the main developments in numerical potential transonic solvers is presented in Section 1.2. This survey goes from the key breakthrough by Murman and Cole in 1970 to the recent developments published by Eller in 2012. The survey shortly discusses the different grid approaches and motivates the use of the unstructured discretization technique used in this thesis to handle complex shapes.

The aspects of the behavior of typical aerodynamic flows that allow reducing the Navier-Stokes equations to the full-potential equation are introduced in

Chapter 2. It is shown that typical aerodynamic flows are characterized by high Reynolds numbers, which allows neglecting the viscous effects outside of attached boundary layers, trailing wakes, and shock waves. With the further assumption of no heat addition due to radiation or chemical reactions, the flow can be assumed to be isentropic. Moreover, it is shown using the Helmholtz vorticity transport equation that for isentropic flows, the vorticity is confined in the boundary layer and the wake if the freestream is irrotational. This means that the outer inviscid flow can be assumed to be irrotational, and thus the velocity may be expressed as the gradient of the potential.

Furthermore, the continuity equation can be expressed as the full-potential equation considering steady-state flow. The numerical solution of the FPE is very challenging due to its mixed-type nature. The classification of the FPE according to the different flow regimes is described in Section 2.3.1. The characteristic equation and the FPE in the nonconservative form are used to derive the discriminant of the quadratic solution, which shows that the FPE is elliptic, parabolic and hyperbolic, for subsonic, sonic, and supersonic flow, respectively.

The boundary conditions are presented in Section 2.3.2. Since the FPE and the remaining boundary conditions are only defined in terms of the velocity potential derivatives, a Dirichlet condition is required to define the value of the potential. Moreover, because the wake intersects the outlet and the value of the potential jump across the wake is unknown a priori, the Dirichlet condition must be applied at the inlet. At infinity, the disturbance introduced by the body on the flow decays to zero. In practice, in the presented method, the infinity condition is applied as a Neumann condition at the outlet by imposing the outflow flux to be the freestream flux. This approximation introduces an error related to the fact that the infinity condition is applied at a finite distance from the body. Because the viscosity effects are neglected, the standard no-slip boundary condition is replaced by a slip condition where the normal velocity component to the body is set to zero, leaving the tangential component arbitrary. In this approach, the wake roll-up is not computed, and the wake is modeled as a straight line (in 2D) or surface (in 3D) extending from the trailing edge in the direction of the freestream velocity. In order to relax this assumption, flux is allowed across the wake. The wake boundary conditions then become conservation of mass and equality of pressures across the wake. The equality of pressures condition stems from the fact that the wake is thin and can thus not support pressure jumps.

Based on the theory introduced in the preceding chapter, the proposed potential transonic solver is described in Chapter 3. First, the strong form and boundary conditions are defined over the specific domains considered in this work. The finite-element discretization is introduced in Section 3.2, emphasizing the problems that appear when the flow becomes supersonic and motivating the use of the artificial compressibility method explained in Section 3.3. For large local velocities, the isentropic relations become ill-defined, and a remedy is required for the regions of large flow curvature, such

as the wingtips' trailing edge. The problem and a remedy are described in Section 3.4.

After introducing the specifics of all required methodologies required to solve transonic flow using the FPE, the proposed embedded wake approach is presented, which is the novelty of this work. The embedded wake approach uses additional degrees of freedom to enrich the finite-element space to support a jump in the potential across the wake. This approach allows efficiently representing the wake implicitly within the mesh. The wake boundary conditions are then applied using a least-squares finite-element approach. The differences between two- and three dimensions are highlighted. Several points require special attention when using this method. In particular, three problems stemming from embedding the wake and the solutions developed within this dissertation are described. The most crucial issue is probably related to the small-cut elements that deteriorate the system's conditioning. Divisions by close to zero values in the computation of the shape functions' derivatives cause the system's large condition numbers. In order to solve this problem, a full integration approach has been developed. This approach has proven to be very effective in maintaining the systems condition number well defined, increasing the method's robustness. Another issue is related to the nodes lying on the wake. This yields a zero potential jump on those nodes resulting in a wrong overall solution. In the proposed method, nodes lying on the wake are displaced a small distance to ensure the correct definition of the potential jump. Trailing edge nodes are also lying on the wake. However, these nodes require special treatment. Because these nodes are also on the surface describing the body, the slip boundary condition is applied instead of the wake boundary conditions. Still, two degrees of freedom are required in the trailing edge nodes to support the potential jump. In the course of the thesis, it has been noted that the obtained flow solution is highly sensitive to the implementation used at the trailing edge. All these aspects are described in detail in Section 3.5.

With the entire potential transonic solver methodology presented, the last part of Chapter 3 describes the implementation of the proposed method in the finite-element framework KRATOS Multiphysics. After introducing Kratos' structure, the potential flow application is presented. In total, three solvers have been implemented: an incompressible solver, a compressible subsonic solver, and a transonic solver. The incompressible solver uses a linear strategy and the implemented incompressible potential flow element. The compressible solvers use the Newton Raphson strategy and the implemented compressible subsonic and transonic elements, respectively. The embedded wake is detected and defined via a process at the initial stage of the simulation. The freestream conditions are applied via the implemented apply far-field process. The wake boundary conditions are automatically handled within the element exploiting the proposed residual formulation. The description of the implementation in KRATOS Multiphysics can be found in Section 3.6.

In order to establish confidence with the numerical results, the proposed method is validated and verified in Chapter 4. A tool has been developed using bash and python to automatically run parameter studies and compare the results with reference data. The tool uses the open-source software Salome to generate the CAD model and the triangular and tetrahedral meshes using the NETGEN algorithm. Salome's output mesh format is converted into Kratos' input mesh format using Kratos Salome Plugin's open-source software. Additionally to the validation and verification test cases, a drag divergence study and a multi-fidelity study are presented to examine the solver's capabilities. In total, two 2D models and two 3D models have been investigated: the NACA 0012 airfoil, the Korn supercritical airfoil, a rectangular wing with NACA 0012 airfoil section, and Onera M6 wing.

The flow solution about NACA 0012 airfoil is computed in three flight regimes: incompressible, compressible subsonic, and transonic. For the incompressible case, a mesh refinement study and a domain size study are presented for an angle of attack of 5°. In the mesh refinement study, the pressure, lift, and pitching moment coefficients are compared to the solution provided by XFOIL. XFOIL is a panel solver. The meshes are refined towards the leading and the trailing edge, where the solution gradients are the largest. The resulting pressure coefficient distribution presents an accurate matching with the reference data. The lift coefficient is computed in three different ways: using a near-field analysis, using the Kutta-Joukowski theorem, and using a far-field analysis.

The near-field analysis consists of integrating the pressure coefficient over the airfoil. The Kutta-Joukowski theorem makes use of the value of the potential jump across the wake. The far-field analysis uses the integral momentum theorem. The solution converges to a value close to the reference data. The relative error lies below 7% for all meshes and below 1% for the three most refined meshes. This small disagreement is associated with the fact that two different methods are being compared. On the one hand, the panel method is a singularity method in which the far-field conditions are satisfied exactly. On the other hand, the proposed approach is a grid method where the far-field boundary conditions are applied at a finite distance from the airfoil. In order to determine the impact of the far-field boundary conditions on the solution, a domain size study is presented.

In the domain size study, the size of the fluid field is gradually increased. The solution shows how the relative error drops from 0.5% to a value below 0.2% using a constant minimum element size of $h = 10^{-6}$. 0.2% is a very small error that can be related to discretization errors, the different wake models between both methods, and differences between the models' geometries. Furthermore, the far-field and potential jump analysis yield the same relative error, which is 0.02% apart from the error predicted with the near-field analysis. This difference might also be related to the discretization error. In fact, the mesh refinement study shows that this difference decreases by decreasing the minimum mesh size.

Interestingly, the results show that in 2D the proposed embedded wake approach does not require a refinement towards the wake. This property constitutes another advantage of this approach.

The value of the lift coefficient is compared with wind tunnel data for different angles of attack to validate the solution. As expected, a better matching is observed for small angles of attack, where the boundary layer is fully attached, and the potential flow assumptions are fulfilled. The same behavior is observed when looking at the pressure coefficient distribution. For an angle of attack of 0° an accurate agreement is achieved. For 10° and 15° the pressure is underestimated in the suction peak, yielding an overestimation of the lift coefficient. The pressure underestimation is related to the overestimation of the velocity magnitude because viscous effects are neglected, and the boundary layer is not resolved. Beyond 15° stall occurs, which cannot be captured with the current method.

To verify that the Jacobian is correctly implemented for the compressible subsonic and transonic solvers, the Jacobian entries obtained for a single triangular and tetrahedral elements are compared with the finite difference calculation. This comparison shows that the results match up to a tolerance of 10^{-10}, meaning that the Jacobian represents the residual's derivative.

The compressible subsonic solution around the NACA 0012 is verified by means of a mesh refinement study for two cases: a lifting case with $\alpha = 2°$ and $M_\infty = 0.63$, and a non-lifting case with $\alpha = 0°$ and $M_\infty = 0.72$. The results are compared with reference data. The resulting pressure coefficient distribution accurately matches the reference data. For the lifting case, the relative error converges to a value below 1%. For the non-lifting case, the absolute error lies below $5 \cdot 10^{-4}$. Newton Raphson's method converges quadratically when the solution is in the region of quadratic convergence, which gives further confidence that the Jacobian is correctly implemented. The solution converges within five to ten iterations with an absolute tolerance of 10^{-10}.

In order to verify the solver in the lower transonic flight regime, the flow solution around the NACA 0012 is compared to the results predicted by FLO36 for four test cases. The pressure coefficient distribution presents an accurate matching with the reference data, including the shock wave position and strength. The lift coefficient relative error converges to a value below 0.5%, and Newton's method exhibits quadratic convergence. The transonic solver is further verified by comparing the pressure coefficient distribution obtained about Korn supercritical airfoil with the solution provided by FLO36 for four test cases. In general, a good agreement with the reference solution is observed. The most significant disagreements occur in the vicinity of the shock wave, where the solution is most sensitive to the selected values of artificial dissipation.

The variation of the drag coefficient with the freestream Mach number is presented in Section 4.6 for both airfoils at a constant angle of attack for

the different flight regimes. This study allows checking whether the implemented solver is capable of capturing the phenomenon of drag divergence. As expected, the results predict a larger drag-divergence Mach number for Korn supercritical airfoil compared to the NACA 0012 airfoil. In order to compare the performance of both airfoils, the variation of the lift coefficient is also presented.

In the incompressible and compressible subsonic regime, below the critical Mach number, the lift increases slowly with the freestream Mach number due to the flow compressibility effects. In these regimes, drag values are zero, as expected from the potential flow theory. The pressure coefficient distribution shows small changes on the lower surface compared to the upper surface. On the upper surface, the expansion of the fluid yields a decrease in pressure, which explains the observed increase of the lift coefficient.

Once the critical Mach number is reached, a shock wave starts to develop on the airfoils' upper surface, indicating the transonic regime's beginning. Right after surpassing the critical Mach number, the drag coefficient starts to increase. Initially, the drag coefficient is small because the shock wave is relatively weak, so the associated wave drag is small. If the freestream Mach number is further increased, the solver predicts that the area covered by supersonic flow on top of the airfoil grows, and the shock wave moves after becoming stronger. In the beginning, this movement and strengthening of the shock wave happen slowly, explaining the slight increase of the drag coefficient. At a certain freestream Mach number, the shock's movement and strengthening accelerate, causing the drag coefficient to increase rapidly. The freestream Mach number at which this happens is the so-called drag-divergence Mach number. For the considered angles of attack, the drag-divergence Mach number is predicted to be around $M_\infty = 0.66$ for the NACA 0012 and $M_\infty = 0.75$ for the Korn airfoil. The fact that the drag-divergence Mach number is larger for the supercritical airfoil than for the conventional one shows the substantial benefit of using supercritical airfoils in the transonic regime. One could argue that this is not a fair comparison because even though the drag coefficient is larger for the NACA 0012 than for the Korn airfoil for any given Mach number in the transonic regime, the lift coefficient is also larger. However, simultaneous comparison of the lift and drag coefficients shows that for the same lift coefficient, the associated drag is much smaller for the Korn airfoil than for the NACA 0012. Supercritical airfoils are designed to have significantly better transonic performance than conventional airfoils, allowing them to fly at larger Mach numbers with less drag.

If the freestream Mach number is further increased, there is a point in which the pressure increment across the shock is high enough to produce the separation of the boundary layer at the shock's base. Typically, separation occurs when the local Mach number before the shock is between 1.25 and 1.30, and as the Reynolds number is high, separation happens when the boundary layer is already turbulent. Beyond this point, the implemented potential solver is not applicable anymore, and a solver capturing the viscous effects of the

boundary layer is required.

In order to further verify the transonic solver, the predicted critical Mach number is compared with the solution obtained via a graphical method. The method consists of plotting the critical pressure coefficient and the minimum pressure coefficient obtained with Prandtl-Glauert's transformation for a range of freestream Mach numbers. The intersection between both curves yields an estimation of the critical Mach number that can be compared with the value predicted by the solver. Both predictions are close to each other, establishing further confidence with the numerical results.

The limits of application of the incompressible, compressible subsonic, and transonic solvers are compared in a multi-fidelity analysis study. To this end, the resulting pressure coefficient distribution, aerodynamic coefficients, and computational time are contrasted at different flight regimes. Expectedly, in the incompressible regime ($M_\infty = 0.01$), all solvers predict the same result in approximately the same time. In the compressible regime ($M_\infty = 0.6$), the subsonic and transonic solvers yield the same results. The incompressible solver underestimates the value of the lift coefficient because it cannot capture the compressibility effects on the top airfoil's surface. In the transonic regime ($M_\infty = 0.73$), the transonic solver takes longer to converge but is expected to deliver more accurate results compared to the compressible and incompressible solvers. The compressible solver underpredicts the aerodynamic coefficients because it cannot capture the transonic effects. The incompressible solver yields the same result in all regimes since the aerodynamic coefficients are independent of the freestream Mach number. In conclusion, the transonic solver is preferred because it yields the same solution as the other solvers in subsonic conditions without major extra cost and can also capture transonic effects in the lower transonic regime as long as the boundary layer is still attached. If fast solutions are preferred in the transonic regime and accuracy is not essential, the subsonic solver can be used, bearing in mind that the aerodynamic coefficients are underestimated and that the solution does not represent the physics where the flow is supersonic.

The first verification case in three dimensions considers a rectangular wing with NACA 0012 airfoil section and aspect ratio 4 at an angle of attack of 5° in incompressible flow. The solution predicted with the proposed method is compared with the result provided by XFLR5. The resulting pressure coefficient at different span sections shows that the proposed solver reproduces the reference data. In contrast to the two-dimensional cases, a refinement towards the wake is necessary to capture the velocity potential spanwise variation. However, this refinement is not required due to the presented embedded approach but is a general requirement that applies to all CFD solvers. Furthermore, the results show that the embedded wake approach successfully imposes the linearized pressure equality condition. The predicted potential jump distribution shows that the nonconformity at the wake tips does not introduce large errors because the potential jump is zero. The proposed embedded wake approach can also predict the wingtip vortices,

which are highly related to induced drag.

The second three-dimensional example is ONERA M6 wing transonic validation case. In this case, the wing is at an angle of attack of $\alpha = 3.06°$ and a freestream Mach number of $M_\infty = 0.84$. Since this case is highly nonlinear, a load control approach is necessary to achieve the convergence of Newton Raphson's method. The pressure coefficient and local Mach number contour plots show that the proposed solver predicts the double-shock pattern on the wing's upper surface. The pressure coefficient distribution is compared at six different sections with reference data from another finite volume potential transonic solver, a RANS solver, and wind tunnel measurements. The solution predicted with the proposed approach lies close to the RANS data over most of the surface. The stronger shock is predicted at the same position as the other full-potential solver, which is further downstream than the position predicted by the RANS and experimental data. The reason for this result is that the potential solvers cannot capture the viscous effects. The aerodynamic coefficients are obtained by integrating the pressure coefficient over the wing's surface, and they are compared with the solution provided by other solvers using different fidelity levels. The predicted coefficients are close to the other full-potential solvers' predictions.

Compared to Tranair's solution, the value of the lift coefficient is the same up to the precision used, and the drag and moment coefficients relative errors lay within 1% and 2%, respectively. The predicted solution is closer to the RANS solution compared to the linear inviscid solvers, which underestimate the lift and moment coefficients because they cannot capture the transonic effects. However, the FPSs overestimate the values of lift and moment coefficient compared to the RANS solver. This lift overestimation is related to the delayed predicted shock wave position mentioned above, which yields a larger area enclosed by the pressure coefficient distribution for the FPSs. The drag coefficient is underestimated compared to the RANS prediction because the FPSs do not capture the viscous effects. When comparing the computational cost, it is observed that the potential linear solvers are the cheapest, followed by the full-potential solvers. The Euler solver comes in third place, and the most expensive solution is provided by the RANS solver. This comparison shows that the FPSs are still an attractive alternative to provide fast flow solutions capturing nonlinear transonic effects at the early stages of aircraft design, where a large number of fluid evaluations are required.

The last three-dimensional example is NASA Common Research Model (CRM). NASA CRM is a modern commercial aircraft geometry. In this case, the aircraft is at an angle of attack of $\alpha = 2.31°$ and a freestream Mach number of $M_\infty = 0.85$. This study aims to validate and verify that the solver also works for a complete aircraft configuration with two trailing wakes and that it can cope with blunt and curved trailing edges. The pressure coefficient and local Mach number contour plots show that the proposed embedded solver can capture the swept-shock pattern on the wing's upper surface. As for the ONERA M6 wing, the pressure coefficient distribution is compared at

six wing sections with reference data from a RANS solver and wind tunnel measurements. The most significant differences between the data appear in the vicinity of the shock wave, which is predicted further downstream with the proposed solver compared to the reference data. As for the previous validation case, this explains the overestimation of the lift coefficient. The total drag coefficient is underestimated because the skin friction is neglected in the potential flow theory. However, the resulting pressure drag coefficient lies close to the reference values with a relative error of 2.1% compared to the CFL3D reference value and of 6.8% compared to the average value provided in the 4th DPW. The error related to the pitching moment coefficient is very large compared to the CFL3D and wind tunnel test's reference values, but it lies within a 6.7% relative error with respect to the lower bound provided by 4th DPW. Taking into account that the agreement between the RANS and wind tunnel data is very poor, and that the spread among the values predicted with different RANS solvers is very large, the suitability of this comparison is questionable. Still, this validation and verification case shows that the proposed solver can capture nonlinear transonic effects for a full aircraft configuration with blunt and curved trailing edges, making it a tool that could potentially be used at the early stages of aircraft design.

The resulting potential contour plot around NASA CRM demonstrates the substantial benefit of using the proposed embedded wake approach, which can successfully capture the discontinuity across both trailing wakes. Furthermore, a nacelle-pylon effect study shows that the solver can be used for more complex configurations.

In conclusion, this thesis treated the problem of developing a method to embed trailing wakes within unstructured grids for the effective application of finite-element transonic potential solvers in the context of aircraft aeroelastic optimization during the conceptual stages of design. The method works both in two and three dimensions. The jump in the potential across the wake is enabled by enriching the finite-element space with auxiliary degrees of freedom in the wake elements. These auxiliary degrees of freedom are also used to impose the wake boundary conditions. A full-integration approach is proposed to avoid the bad system conditioning stemming from the small-cut elements. The validation and verification cases show that the method yields a similar accuracy compared to other potential solvers without requiring an additional refinement to capture the embedded wake. Thus, the proposed embedded wake approach does not entail extra computational cost compared to the standard wake-mesh-fitted approaches.

5.2 Outlook

This section makes several suggestions on how the work presented in this thesis could be continued. The suggestions can be summarized in four points:

- Aeroelastic analysis validation and verification by coupling the presented solver with a structural solver.
- Development, implementation, and verification of aerodynamic and coupled sensitivities for aircraft aeroelastic optimization.
- Embed the complete aircraft's geometry within the grid to further simplify the mesh generation process.
- Coupling of the full-potential equation and the boundary layer equations to include viscous effects.

In order to perform aeroelastic analysis with the proposed approach, a multi-physics tool can be used to couple the FPS with a structural solver. The most straightforward way to do the coupling is directly using KRATOS Multi-physics. Kratos counts with a library called CoSimIO to perform interprocess communication in CoSimulation contexts [88, 89]. Furthermore, Kratos has a co-simulation and a structural mechanics application. The co-simulation application allows coupling solvers within Kratos Multi-physics [90]. Both CoSimIO and co-simulation application are mainly being developed by Philipp Bucher. These tools have already been validated and verified for the aeroelastic analysis of flexible lifting surfaces [91]. Sill, there exist other open-source tools for coupling numerical solvers such as OpenMDAO [92, 93].

Special care is required to define the wake within an aeroelastic analysis. Since the trailing edge position may change from iteration to iteration, the wake elements need to be newly defined. Moreover, there are two possibilities to achieve the mesh refinement required to capture the solution gradients in the span direction along the wake. One option is to automatically refine the mesh using a metric-based technique [50]. Another option is to move the wake elements along with the trailing edge. This operation can be easily implemented by searching for the closest trailing edge node to each wake element and assigning the node's computed displacement. The second option is expected to be faster but cannot be applied to the wake elements in the fuselage's vicinity, which are typically fixed. Still, since the fuselage is already typically refined, this can be easily overcome by defining a threshold distance to the fuselage where wake elements are not explicitly moved.

In order to use the proposed solver in the context of aeroelastic optimization, aerodynamic and coupled sensitivities need to be developed, implemented, and verified using, for example, the discrete adjoint method. However, in industrial aircraft optimization, it is still challenging to apply trim constraints using the ailerons, elevators, or rudder when employing grid methods without excessive

mesh distortion. A possible approach could be to use a hybrid method in which ailerons, elevators, and rudders are embedded within the mesh while the rest of the aircraft is body-fitted or to completely embed the aircraft's geometry within the mesh [94, 95]. A further approach could be to use a chimera approach for these parts.

Finally, the proposed FPS can be coupled to a boundary layer solver. Although this approach still would not be as general as a RANS solver, it would allow accounting for viscous effects to compute more accurate solutions than the single FPS at a lower cost [23].

Appendix A

Helmholtz Vorticity Transport Equation

In this appendix the equation governing the change of vorticity is derived. Taking the curl of the momentum equation (Eq. (2.3)) yields:

$$\frac{\partial \boldsymbol{\omega}}{\partial t} - \nabla \times (\boldsymbol{u} \times \boldsymbol{\omega}) = -\nabla \left(\frac{1}{\rho}\right) \times \nabla p + \nabla \times \left(\frac{\nabla \cdot \bar{\bar{\boldsymbol{\tau}}}}{\rho}\right) \tag{A.1}$$

where the following identities have been used:

$$\boldsymbol{u} \cdot \nabla \boldsymbol{u} \equiv \frac{\nabla u^2}{2} - \boldsymbol{u} \times \boldsymbol{\omega} \tag{A.2}$$

$$\nabla \times \nabla u^2 \equiv 0 \tag{A.3}$$

and the body force is assumed to be conservative $\nabla \times \boldsymbol{f} = 0$. Also, note that the curl commutes with the partial time derivative operation $\partial/\partial(\ )$. To simplify Eq. (A.1), the following vector identity is used:

$$\nabla \times (\boldsymbol{u} \times \boldsymbol{\omega}) = \boldsymbol{u} \nabla \cdot \boldsymbol{\omega} - \boldsymbol{u} \cdot \nabla \boldsymbol{\omega} + \boldsymbol{\omega} \cdot \boldsymbol{u} - \boldsymbol{\omega} \nabla \cdot \boldsymbol{u} \tag{A.4}$$

where the first term of the right-hand side $(\boldsymbol{u} \nabla \cdot \boldsymbol{\omega})$ vanishes due to the vector identity $\nabla \cdot \nabla \boldsymbol{\omega} = 0$. The last term in Eq. (A.4) can be written as:

$$\boldsymbol{\omega} \nabla \cdot \boldsymbol{u} = \rho \boldsymbol{\omega} \frac{D(1/\rho)}{Dt} \tag{A.5}$$

by using the continuity equation (Eq. (2.2)):

$$\frac{1}{\rho}\frac{D\rho}{Dt} = -\rho\frac{D(1/\rho)}{Dt} = -\nabla \cdot \boldsymbol{u} \tag{A.6}$$

which gives:

$$\nabla \times (\boldsymbol{u} \times \boldsymbol{\omega}) = \boldsymbol{u} \cdot \nabla\boldsymbol{\omega} + \boldsymbol{\omega} \cdot \boldsymbol{u} - \rho\boldsymbol{\omega}\frac{D(1/\rho)}{Dt} \tag{A.7}$$

Substituting Eq. (A.7) in Eq. (A.1), dividing by ρ, and combining and rearranging terms yields:

$$\frac{D}{Dt}\left(\frac{\boldsymbol{\omega}}{\rho}\right) = \frac{\boldsymbol{\omega}}{\rho} \cdot \nabla\boldsymbol{u} + \frac{\nabla\rho \times \nabla p}{\rho^3} + \frac{1}{\rho}\nabla \times \left(\frac{\nabla\bar{\bar{\boldsymbol{\tau}}}}{\rho}\right) \tag{A.8}$$

which is Helmholtz vorticity transport equation.

Appendix B

Transonic Full-potential Solver Sensitivities

This appendix presents the sensitivities required to implement the transonic full-potential solver in KRATOS Multi-physics.

B.1 Residual

As derived in Section 3.3, the full-potential solver residual and Jacobian are:

$$R^i = \sum_e \int_{\Omega_e} \frac{\partial N^i}{\partial x^a} \tilde{\rho} u^a \; d\Omega_e - \sum_c \int_{\Gamma_c} N^i q \; d\Gamma_c = 0 \qquad \text{(3.23 revisited)}$$

$$J^{ij} = \frac{\partial R^i}{\partial \phi^j} = \sum_e \int_{\Omega_e} \frac{\partial N^i}{\partial x^a} \left(\tilde{\rho} \frac{\partial u^a}{\partial \phi^j} + \frac{\partial \tilde{\rho}}{\partial \phi^j} u^a \right) d\Omega_e \qquad \text{(3.24 revisited)}$$

B.2 Upwind density

The upwind density is defined as:

$$\tilde{\rho} = \rho - \mu_s(\rho - \rho_{\text{up}}) \qquad \text{(3.19 revisited)}$$

Note that since the upwind density depends on the upstream density, it does not only depend on the degrees of freedom of the current element ϕ^j, but also on the ones of the upstream element, which will be denoted in the following

as ϕ^j_{up}. Furthermore, because of the switching function, the upwind density sensitivities depend on the type of flow:

Subsonic flow ($M < M_{\text{crit}}$)

$$\frac{\partial \tilde{\rho}}{\partial \phi^j} = \frac{\partial \rho}{\partial \phi^j} \tag{B.1}$$

$$\frac{\partial \tilde{\rho}}{\partial \phi^j_{\text{up}}} = 0 \tag{B.2}$$

Supersonic and accelerating flow ($M > M_{\text{crit}}$ and $M > M_{\text{up}}$)

$$\frac{\partial \tilde{\rho}}{\partial \phi^j} = \frac{\partial \rho}{\partial \phi^j} - \left[\frac{\partial \mu}{\partial \phi^j}(\rho - \rho_{\text{up}}) + \mu \frac{\partial \rho}{\partial \phi^j} \right] \tag{B.3}$$

$$\frac{\partial \tilde{\rho}}{\partial \phi^j_{\text{up}}} = 0 - \left[0 - \mu \frac{\partial \rho_{\text{up}}}{\partial \phi^j_{\text{up}}} \right] \tag{B.4}$$

Supersonic and decelerating flow ($M > M_{\text{crit}}$ and $M < M_{\text{up}}$)

$$\frac{\partial \tilde{\rho}}{\partial \phi^j} = \frac{\partial \rho}{\partial \phi^j} - \left[0 + \mu_{\text{up}} \frac{\partial \rho}{\partial \phi^j} \right] \tag{B.5}$$

$$\frac{\partial \tilde{\rho}}{\partial \phi^j_{\text{up}}} = 0 - \left[\frac{\partial \mu_{\text{up}}}{\partial \phi^j_{\text{up}}}(\rho - \rho_{\text{up}}) - \mu_{\text{up}} \frac{\partial \rho_{\text{up}}}{\partial \phi^j_{\text{up}}} \right] \tag{B.6}$$

B.3 Density

The density can be derived from the isentropic relation for calorically perfect gases (Eq. (2.31)) and the compressible Bernoulli equation (Eq. (2.34)):

$$\rho = \rho_\infty \left[1 + \frac{\gamma - 1}{2} M_\infty^2 \left(1 - \frac{u^2}{u_\infty^2} \right) \right]^{\frac{1}{\gamma - 1}} \tag{2.41 revisited}$$

And its sensitivities are:

$$\frac{\partial \rho}{\partial \phi^j} = \frac{\partial \rho}{\partial u^2} \frac{\partial u^2}{\partial \phi^j} \tag{B.7}$$

$$\frac{\partial \rho}{\partial u^2} = -\frac{\rho_\infty}{2 a_\infty^2} \left[1 + \frac{\gamma - 1}{2} M_\infty^2 \left(1 - \frac{u^2}{u_\infty^2} \right) \right]^{\frac{2 - \gamma}{\gamma - 1}} \tag{B.8}$$

B.4 Upwinding factor

The upwinding factor is:

$$\mu = 1 - \frac{M_{\text{crit}}^2}{M^2} \tag{3.21}$$

Deriving with respect to the degrees of freedom and applying the chain rule yields:

$$\frac{\partial \mu}{\partial \phi^j} = \frac{\partial \mu}{\partial M^2} \frac{\partial M^2}{\partial u^2} \frac{\partial u^2}{\partial \phi^j} \tag{B.9}$$

$$\frac{\partial \mu}{\partial M^2} = -\frac{M_{\text{crit}}^2}{M^4} \tag{B.10}$$

B.5 Mach number squared

As for the density, the expression from the local Mach number can also be derived from the isentropic relation (Eq. (2.31)) and the compressible Bernoulli equation (Eq. (2.34)):

$$M^2 = \frac{u^2}{a_\infty^2} \left[1 + \frac{\gamma - 1}{2} M_\infty^2 \left(1 - \frac{u^2}{u_\infty^2} \right) \right]^{-1} \tag{B.11}$$

Its derivative with respect to the velocity squared is:

$$\frac{\partial M^2}{\partial u^2} = M^2 \left\{ \frac{1}{u^2} + \frac{\gamma - 1}{2} \frac{1}{a_\infty^2} \left[1 + \frac{\gamma - 1}{2} M_\infty^2 \left(1 - \frac{u^2}{u_\infty^2} \right) \right]^{-1} \right\} \tag{B.12}$$

B.6 Velocity squared

The velocity squared is:

$$u^2 = \boldsymbol{u} \cdot \boldsymbol{u} = u^a u^a \tag{B.13}$$

and its derivative with respect to the degrees of freedom can be written as:

$$\frac{\partial u^2}{\partial \phi^j} = \frac{\partial u^2}{\partial u^a} \frac{\partial u^a}{\partial \phi^j} \tag{B.14}$$

$$\frac{\partial u^2}{\partial u^a} = 2u^a \tag{B.15}$$

B.7 Velocity vector

The velocity vector is:

$$\boldsymbol{u} = u^a = u^a_\infty + \frac{\partial N^j}{\partial x^a}\phi^j \tag{B.16}$$

and its sensitivity with respect to ϕ^j is:

$$\frac{\partial u^a}{\partial \phi^j} = \frac{\partial N^j}{\partial x^a} \tag{B.17}$$

Appendix C

Verification of the Embedded Wake Approach for Incompressible Flow

In order to verify that the proposed embedded wake approach delivers robust results for arbitrary angles of attack, the mesh refinement study presented in Section 4.1.2 has been performed for eight additional angles of attack for the NACA 0012 airfoil. The results are summarized in Tables C.1 and C.2. To visualize the convergence of the solution, the lift and pitching moment coefficients are plotted in Figures C.1 to C.16 along with their relative errors. As in Section 4.1.2 a domain size of 100 m and a chord of length of 1 m are considered. The lift coefficient relative error lays below 7% for all meshes. The maximum error is 6.2% and occurs for the coarsest mesh using the near-field analysis for an angle of attack of 3°. Furthermore, for all angles of attack the relative error lays below 2.3% and 1% for a minimum element size smaller than 10^{-3} m and 10^{-4} m, respectively. For all cases the relative error converges to a value of about 0.4%. This error is mostly related to the approximation introduced by applying the far-field boundary conditions at a finite distance and can be decreased by making the domain size larger as shown in Section 4.1.4. For a further discussion regarding the possible sources of error see Section 4.1.4. Moreover, note that the difference between the values yielded by the different approaches decreases with the element size for all angles of attack.

Similar results are observed for the pitching moment coefficient. For all cases, the error converges to a value below 0.4%. These results show that the embedded wake approach accurately matches the reference data.

Minimum mesh size h [m]	Lift: Near-field c_l [-]	Lift: Near-field δ_{c_l} [%]	Lift: Potential jump c_l [-]	Lift: Potential jump δ_{c_l} [%]	Lift: Far-field c_l [-]	Lift: Far-field δ_{c_l} [%]	Pitching moment: Near-field c_m [-]	Pitching moment: Near-field δ_{c_m} [%]
Angle of attack $\alpha = 1.0°$								
10^{-2}	0.1153	4.5544	0.1154	4.4575	0.1154	4.4568	-0.0292	7.2334
10^{-3}	0.1182	2.1225	0.1183	2.0900	0.1183	2.0893	-0.0305	3.2726
10^{-4}	0.1197	0.9174	0.1197	0.8954	0.1197	0.8947	-0.0312	1.0553
10^{-5}	0.1201	0.5391	0.1202	0.5177	0.1202	0.5169	-0.0314	0.3523
10^{-6}	0.1203	0.4385	0.1203	0.4128	0.1203	0.4121	-0.0314	0.1589
10^{-7}	0.1203	0.4298	0.1203	0.4078	0.1203	0.4071	-0.0315	0.1488
Reference	0.1208	0.0	0.1208	0.0	0.1208	0.0	-0.0315	0.0
Angle of attack $\alpha = 2.0°$								
10^{-2}	0.2297	4.9105	0.2300	4.8142	0.2300	4.8135	-0.0580	8.1336
10^{-3}	0.2367	2.0319	0.2368	2.0003	0.2368	1.9996	-0.0610	3.2768
10^{-4}	0.2398	0.7533	0.2398	0.7307	0.2398	0.7300	-0.0625	0.9375
10^{-5}	0.2403	0.5336	0.2404	0.5105	0.2404	0.5098	-0.0628	0.5346
10^{-6}	0.2405	0.4606	0.2405	0.4382	0.2405	0.4375	-0.0628	0.3969
10^{-7}	0.2405	0.4499	0.2406	0.4297	0.2406	0.4290	-0.0629	0.3867
Reference	0.2416	0.0	0.2416	0.0	0.2416	0.0	-0.0631	0.0
Angle of attack $\alpha = 3.0°$								
10^{-2}	0.3399	6.1779	0.3403	6.0600	0.3403	6.0593	-0.0847	10.3848
10^{-3}	0.3556	1.8465	0.3557	1.8120	0.3557	1.8112	-0.0918	2.8687
10^{-4}	0.3594	0.7896	0.3595	0.7682	0.3595	0.7675	-0.0936	0.9594
10^{-5}	0.3603	0.5605	0.3604	0.5381	0.3604	0.5374	-0.0940	0.5304
10^{-6}	0.3606	0.4760	0.3607	0.4551	0.3607	0.4544	-0.0941	0.3785
10^{-7}	0.3607	0.4460	0.3608	0.4249	0.3608	0.4242	-0.0942	0.3229
Reference	0.3623	0.0	0.3623	0.0	0.3623	0.0	-0.0945	0.0
Angle of attack $\alpha = 4.0°$								
10^{-2}	0.4536	6.0652	0.4542	5.9478	0.4542	5.9471	-0.1130	10.1687
10^{-3}	0.4734	1.9681	0.4735	1.9379	0.4735	1.9372	-0.1219	3.0868
10^{-4}	0.4790	0.8139	0.4791	0.7911	0.4791	0.7903	-0.1246	0.9783
10^{-5}	0.4801	0.5795	0.4802	0.5593	0.4802	0.5585	-0.1251	0.5532
10^{-6}	0.4806	0.4744	0.4807	0.4527	0.4807	0.4519	-0.1253	0.3616
10^{-7}	0.4807	0.4496	0.4808	0.4281	0.4808	0.4274	-0.1254	0.3058
Reference	0.4829	0.0	0.4829	0.0	0.4829	0.0	-0.1258	0.0

Table C.1: Mesh refinement studies.

Angle of attack $\alpha = 6.0°$								
Minimum	Lift						Pitching moment	
mesh size	Near-field		Potential jump		Far-field		Near-field	
h [m]	c_l [-]	δ_{c_l} [%]	c_l [-]	δ_{c_l} [%]	c_l [-]	δ_{c_l} [%]	c_m [-]	δ_{c_m} [%]
10^{-2}	0.6811	5.8594	0.6822	5.7033	0.6822	5.7026	-0.1696	9.7205
10^{-3}	0.7095	1.9330	0.7098	1.9000	0.7098	1.8992	-0.1822	3.0310
10^{-4}	0.7175	0.8242	0.7177	0.8032	0.7177	0.8024	-0.1860	1.0158
10^{-5}	0.7196	0.5401	0.7197	0.5190	0.7198	0.5182	-0.1870	0.4842
10^{-6}	0.7201	0.4651	0.7203	0.4418	0.7203	0.4411	-0.1873	0.3434
10^{-7}	0.7204	0.4321	0.7205	0.4103	0.7205	0.4096	-0.1874	0.2839
Reference	0.7235	0.0	0.7235	0.0	0.7235	0.0	-0.1879	0.0
Angle of attack $\alpha = 7.0°$								
10^{-2}	0.7981	5.3987	0.8003	5.1359	0.8003	5.1351	-0.1997	8.6756
10^{-3}	0.8287	1.7682	0.8289	1.7369	0.8290	1.7361	-0.2127	2.7382
10^{-4}	0.8365	0.8393	0.8367	0.8188	0.8367	0.8180	-0.2164	1.0519
10^{-5}	0.8385	0.6059	0.8387	0.5848	0.8387	0.5840	-0.2173	0.6269
10^{-6}	0.8396	0.4685	0.8398	0.4467	0.8398	0.4459	-0.2179	0.3629
10^{-7}	0.8399	0.4377	0.8401	0.4168	0.8401	0.4160	-0.2180	0.3098
Reference	0.8436	0.0	0.8436	0.0	0.8436	0.0	-0.2187	0.0
Angle of attack $\alpha = 8.0°$								
10^{-2}	0.9167	4.8439	0.9190	4.6106	0.9190	4.6098	-0.2301	7.6770
10^{-3}	0.9421	2.2089	0.9424	2.1749	0.9425	2.1741	-0.2403	3.5550
10^{-4}	0.9559	0.7797	0.9561	0.7575	0.9561	0.7567	-0.2468	0.9433
10^{-5}	0.9579	0.5663	0.9581	0.5463	0.9581	0.5455	-0.2478	0.5547
10^{-6}	0.9589	0.4687	0.9591	0.4498	0.9591	0.4490	-0.2483	0.3790
10^{-7}	0.9591	0.4456	0.9593	0.4246	0.9593	0.4238	-0.2484	0.3305
Reference	0.9634	0.0	0.9634	0.0	0.9634	0.0	-0.2492	0.0
Angle of attack $\alpha = 9.0°$								
10^{-2}	1.0329	4.6057	1.0355	4.3670	1.0355	4.3662	-0.2591	7.2224
10^{-3}	1.0642	1.7179	1.0646	1.6854	1.0646	1.6845	-0.2719	2.6327
10^{-4}	1.0738	0.8299	1.0740	0.8081	1.0741	0.8072	-0.2764	1.0209
10^{-5}	1.0767	0.5674	1.0769	0.5469	1.0769	0.5460	-0.2778	0.5354
10^{-6}	1.0779	0.4545	1.0781	0.4340	1.0781	0.4331	-0.2784	0.3367
10^{-7}	1.0781	0.4301	1.0784	0.4092	1.0784	0.4084	-0.2785	0.2862
Reference	1.0828	0.0	1.0828	0.0	1.0828	0.0	-0.2793	0.0

Table C.2: Mesh refinement studies.

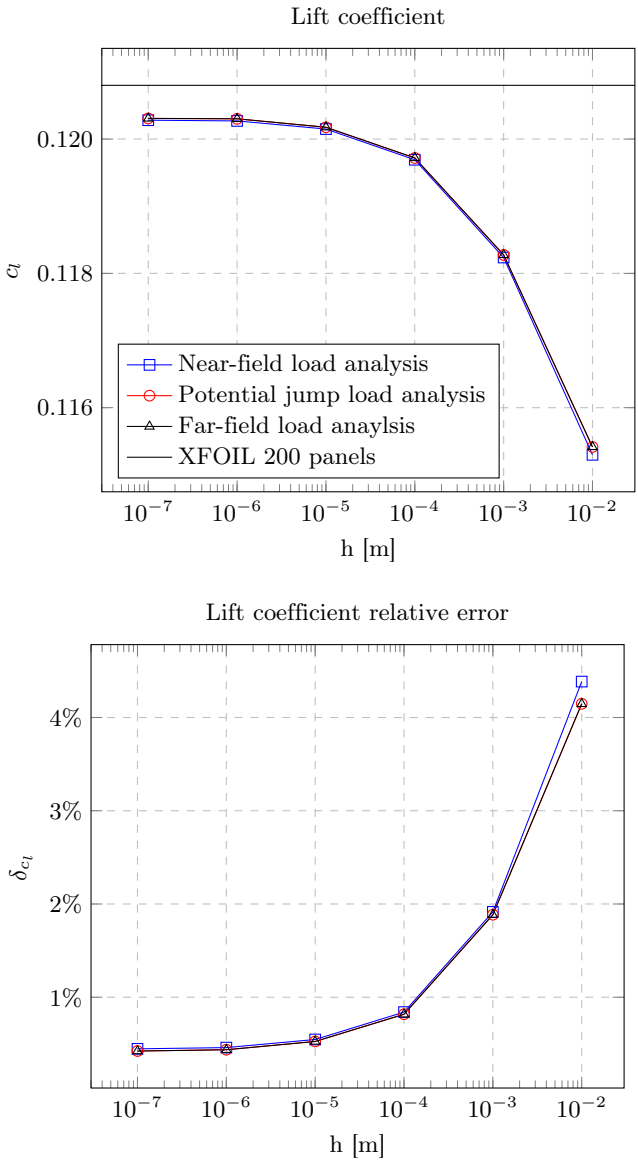

Figure C.1: NACA 0012 mesh refinement study ($\alpha = 1.0°$).

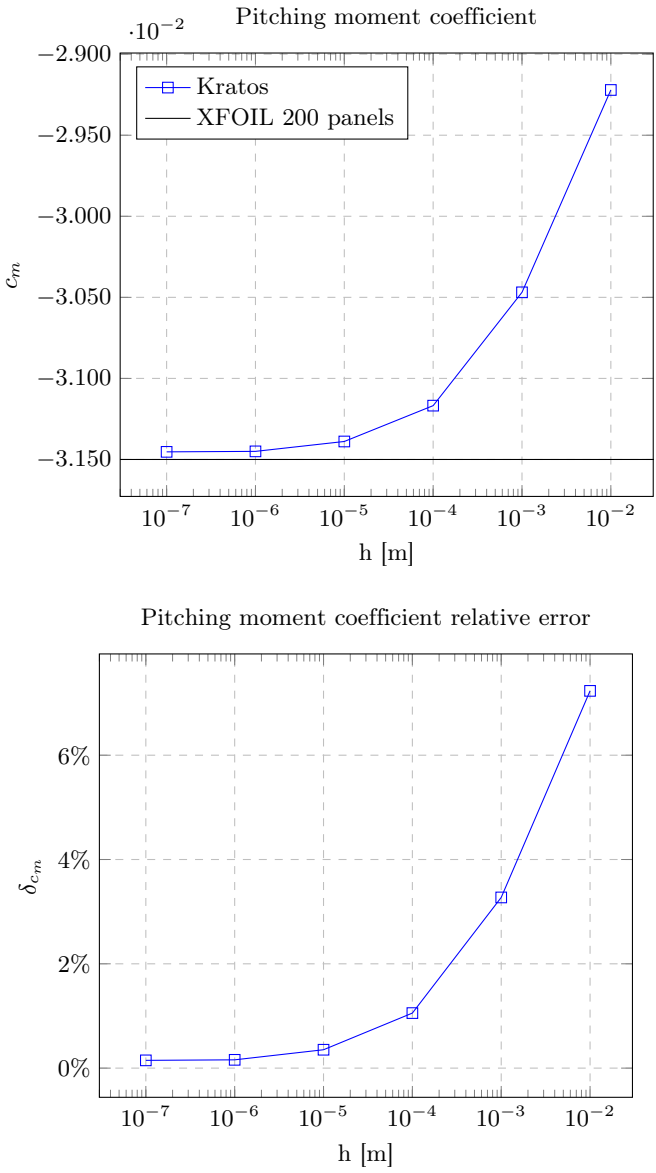

Figure C.2: NACA 0012 mesh refinement study ($\alpha = 1.0°$).

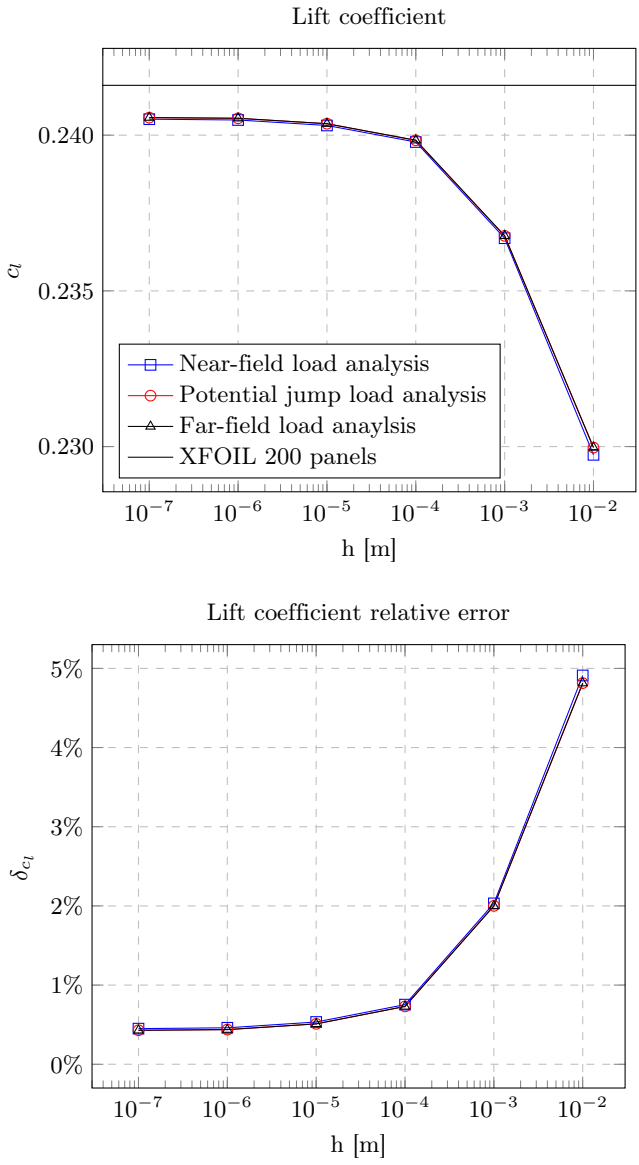

Figure C.3: NACA 0012 mesh refinement study ($\alpha = 2.0°$).

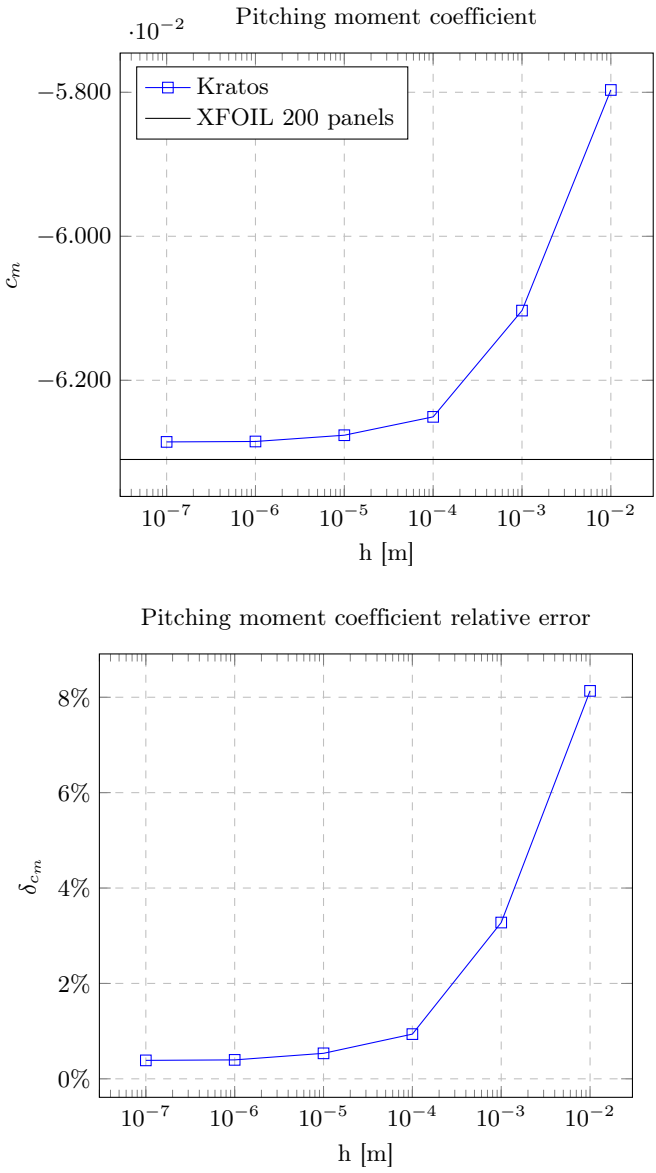

Figure C.4: NACA 0012 mesh refinement study ($\alpha = 2.0°$).

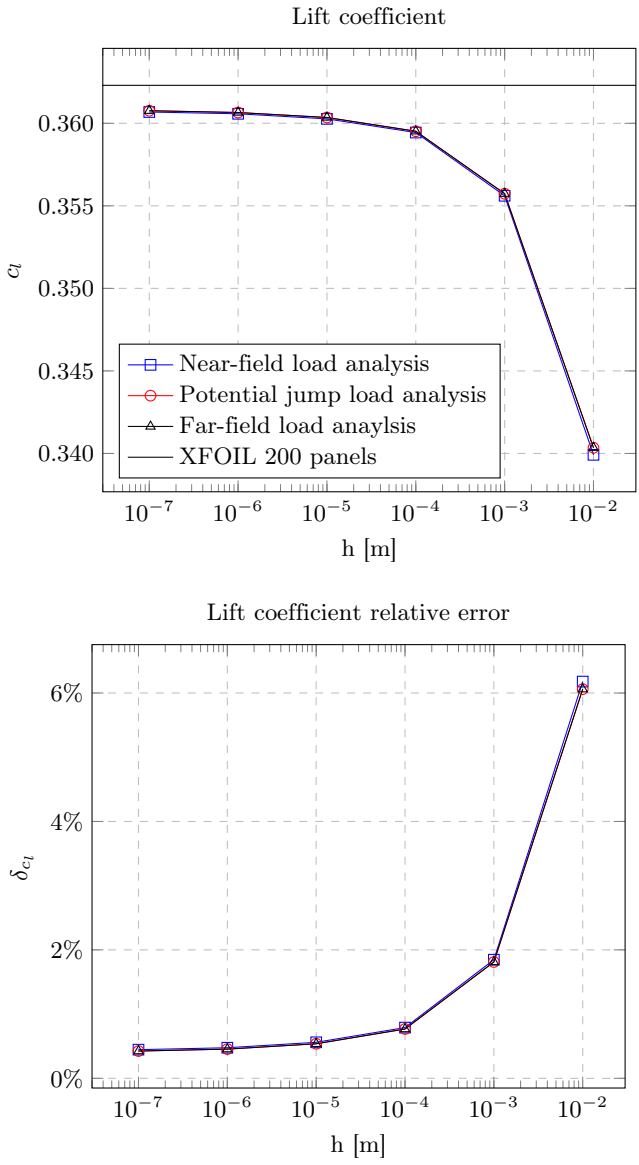

Figure C.5: NACA 0012 mesh refinement study ($\alpha = 3.0°$).

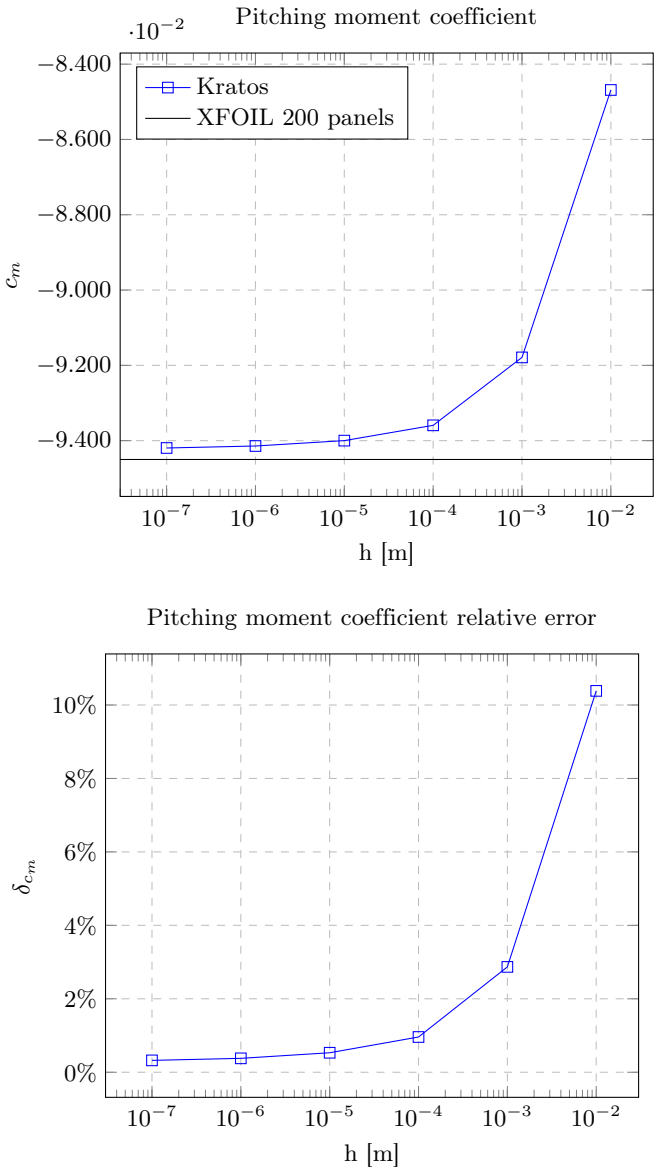

Figure C.6: NACA 0012 mesh refinement study ($\alpha = 3.0°$).

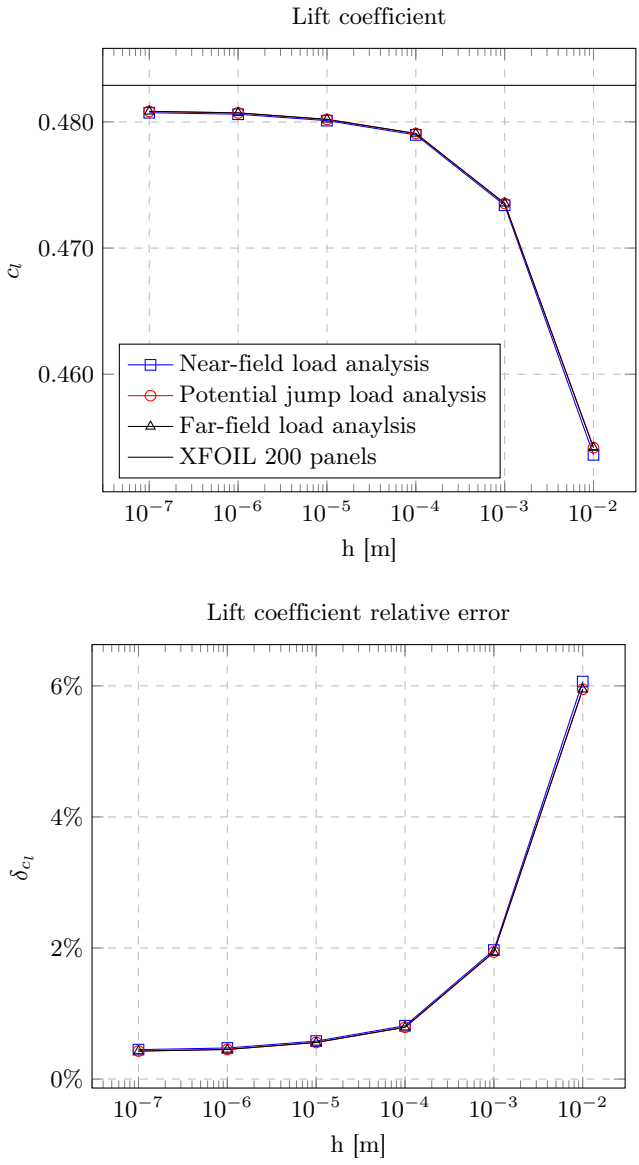

Figure C.7: NACA 0012 mesh refinement study ($\alpha = 4.0°$).

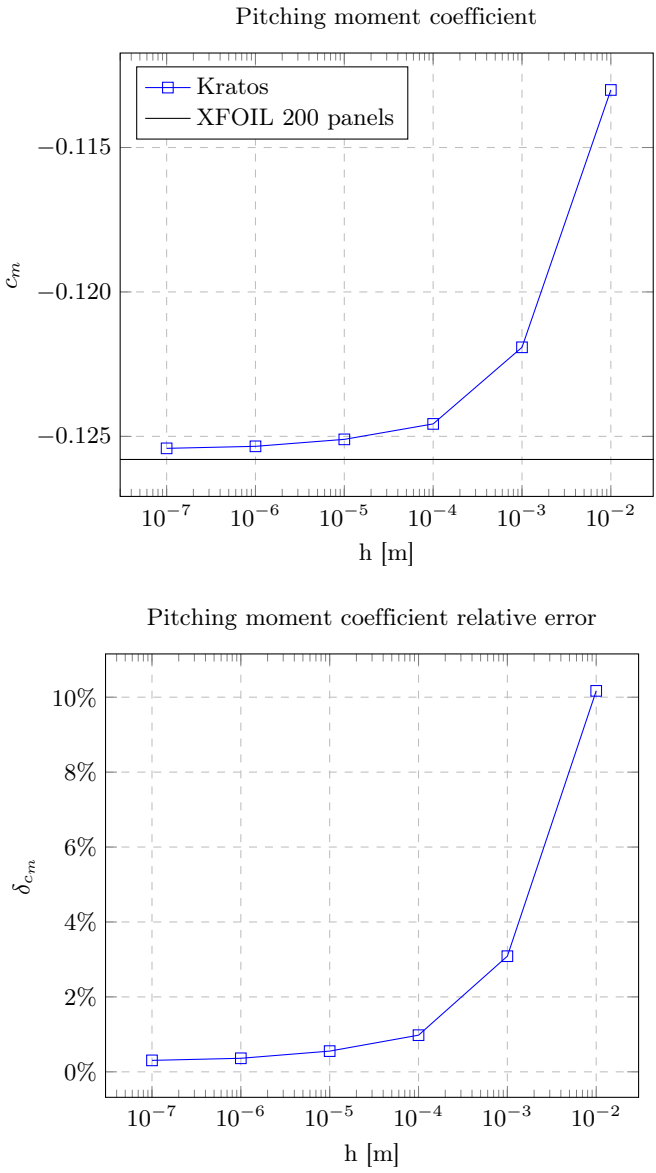

Figure C.8: NACA 0012 mesh refinement study ($\alpha = 4.0°$).

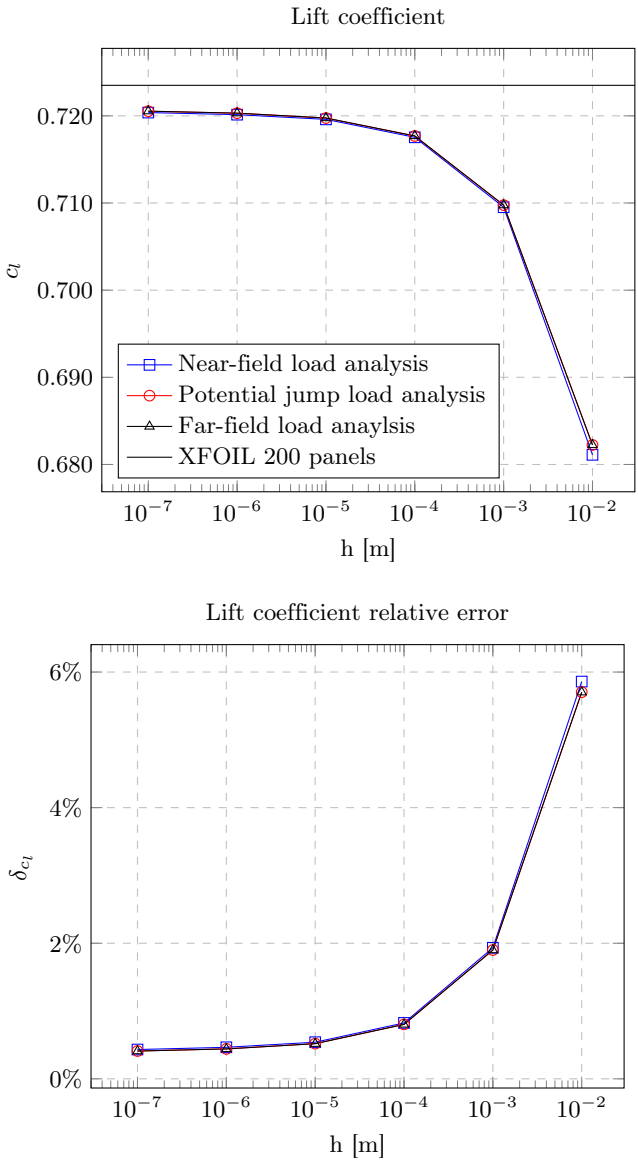

Figure C.9: NACA 0012 mesh refinement study ($\alpha = 6.0°$).

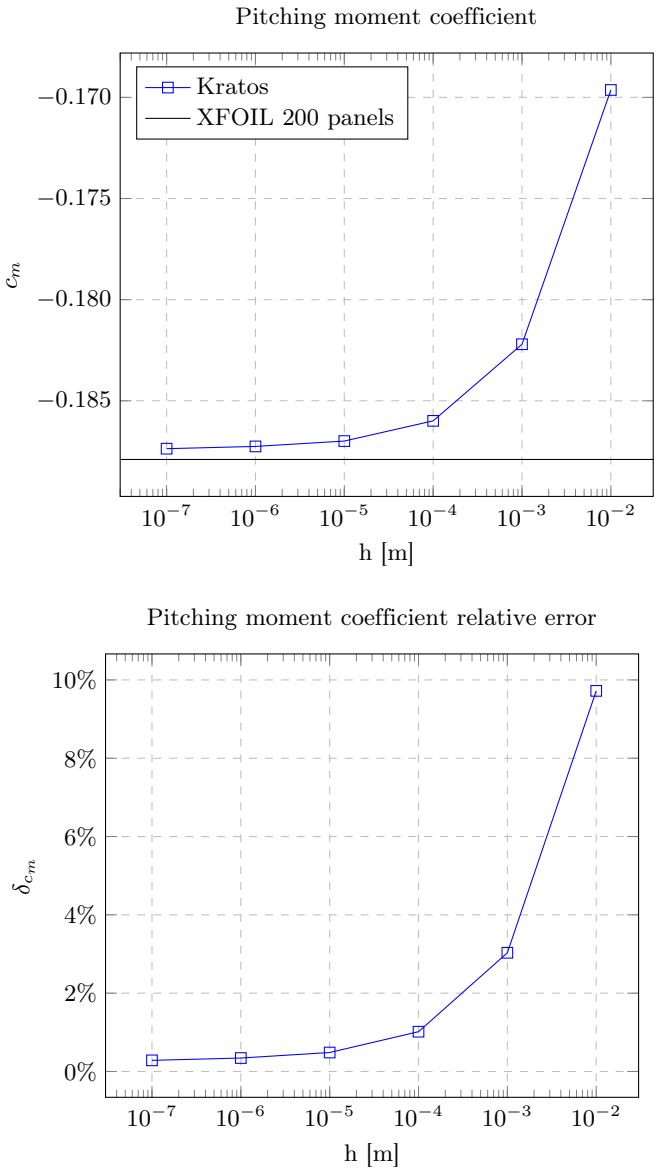

Figure C.10: NACA 0012 mesh refinement study ($\alpha = 6.0°$).

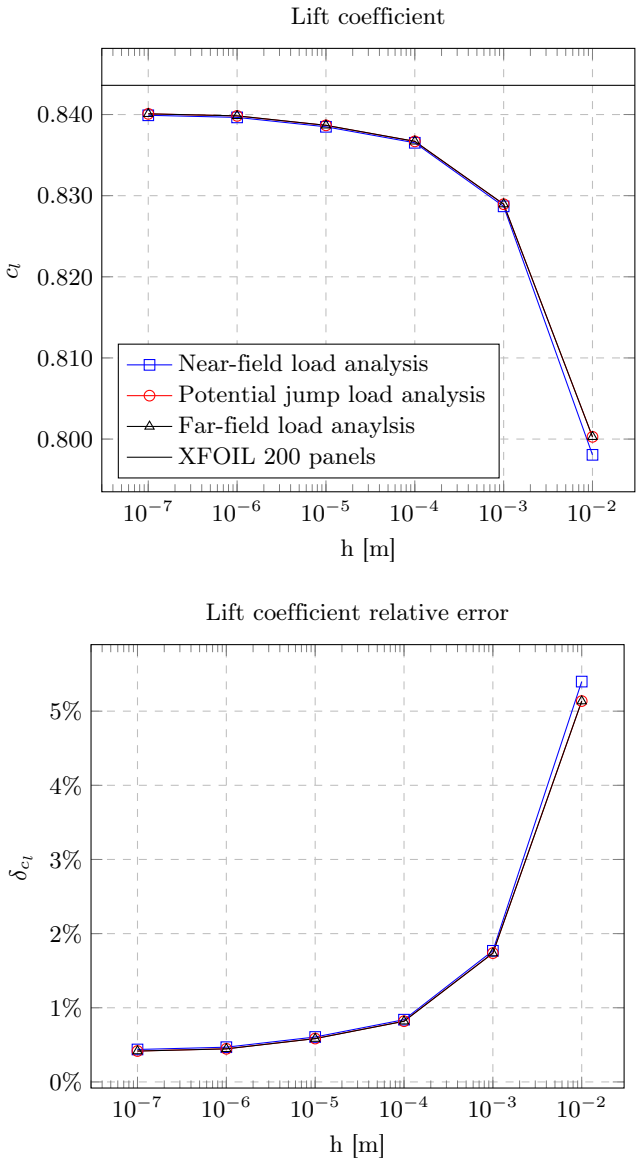

Figure C.11: NACA 0012 mesh refinement study ($\alpha = 7.0°$).

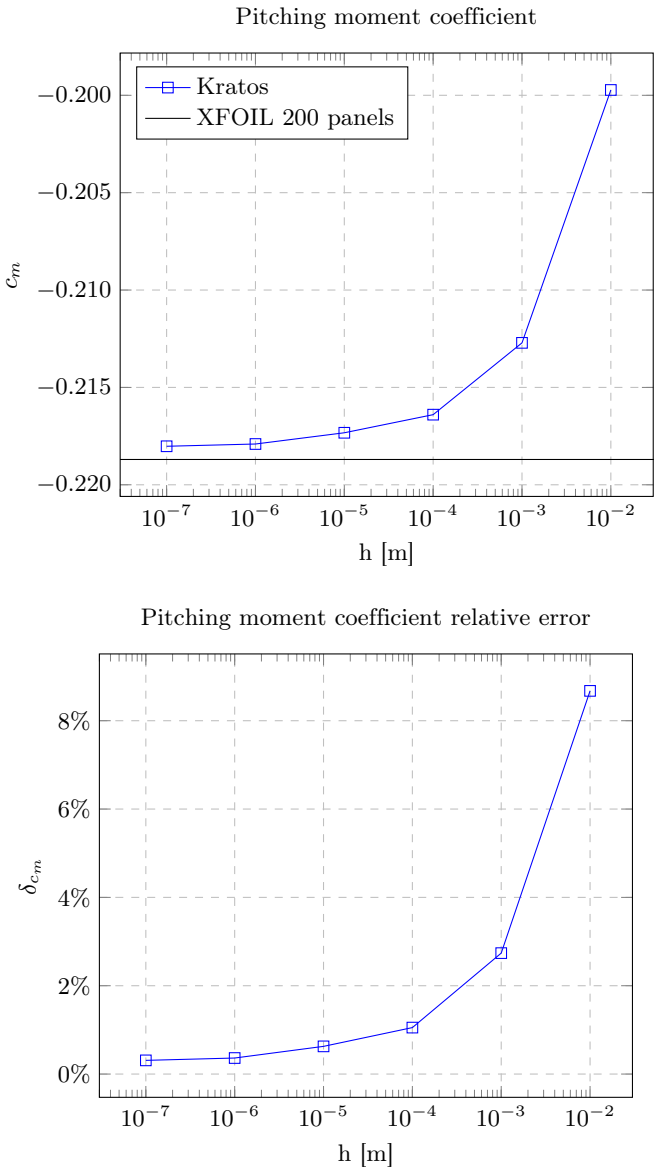

Figure C.12: NACA 0012 mesh refinement study ($\alpha = 7.0°$).

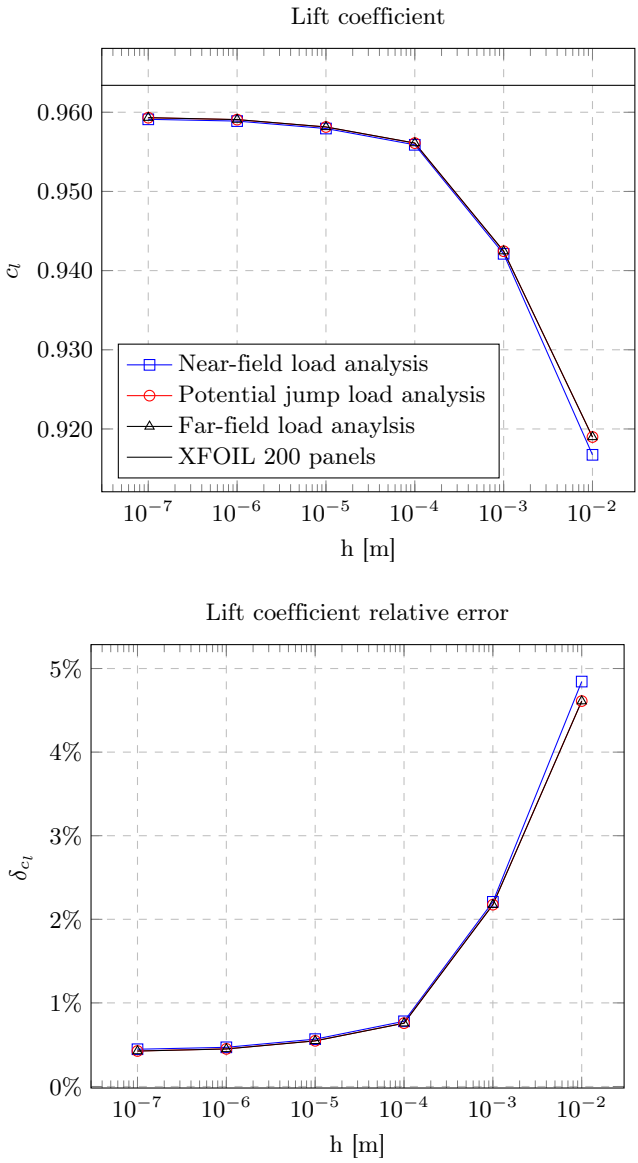

Figure C.13: NACA 0012 mesh refinement study ($\alpha = 8.0°$).

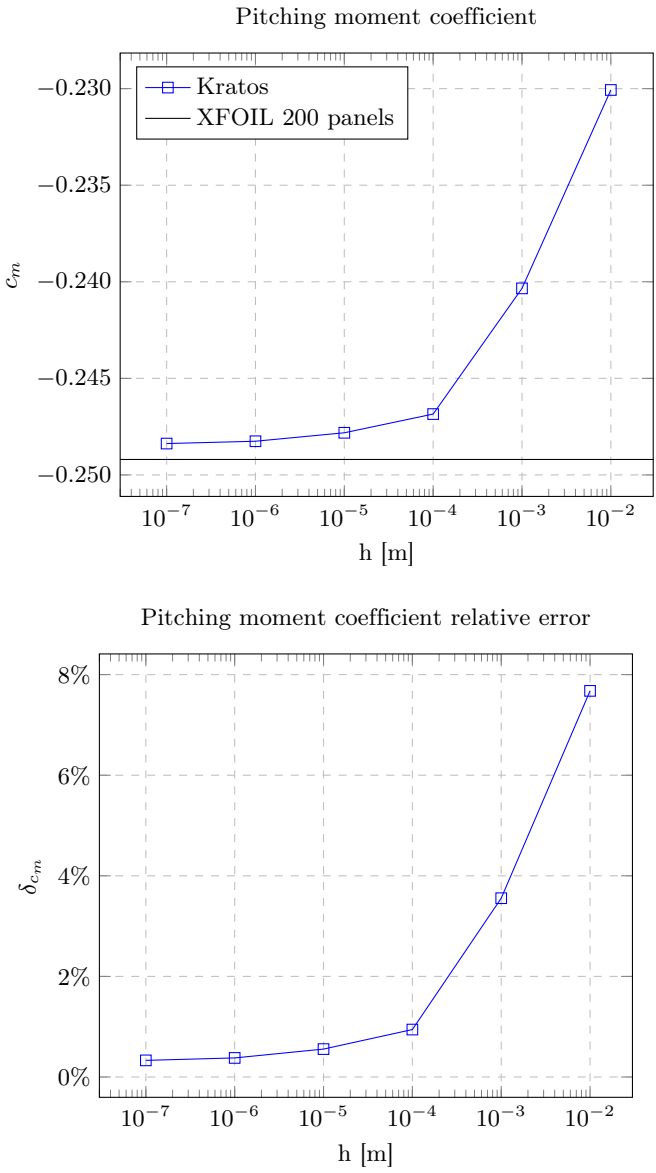

Figure C.14: NACA 0012 mesh refinement study ($\alpha = 8.0°$).

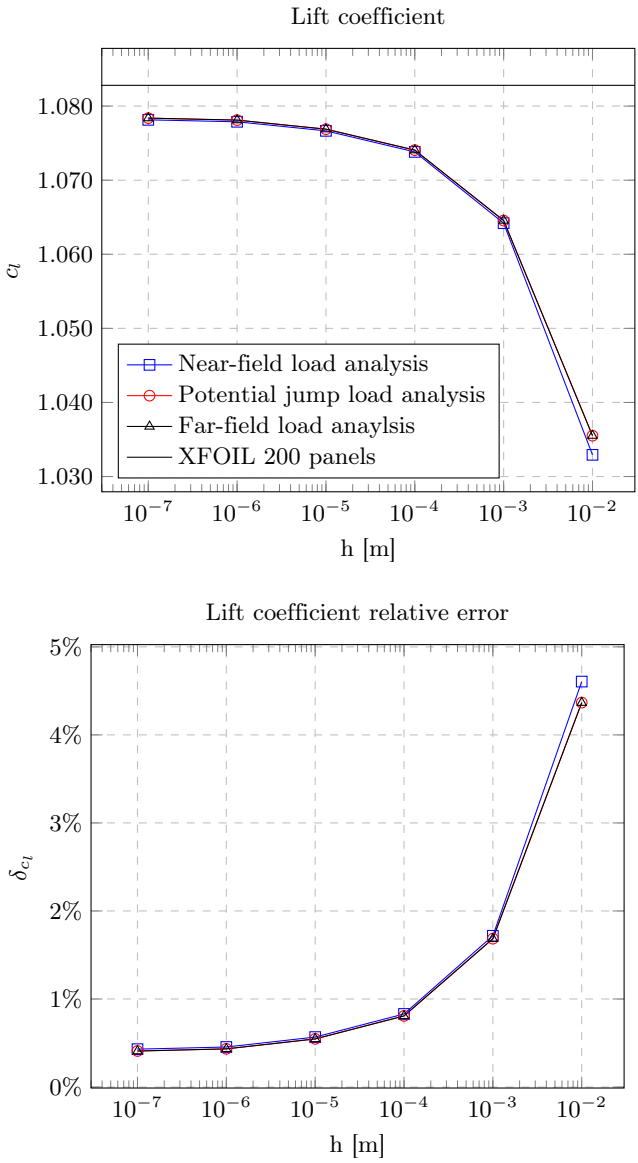

Figure C.15: NACA 0012 mesh refinement study ($\alpha = 9.0°$).

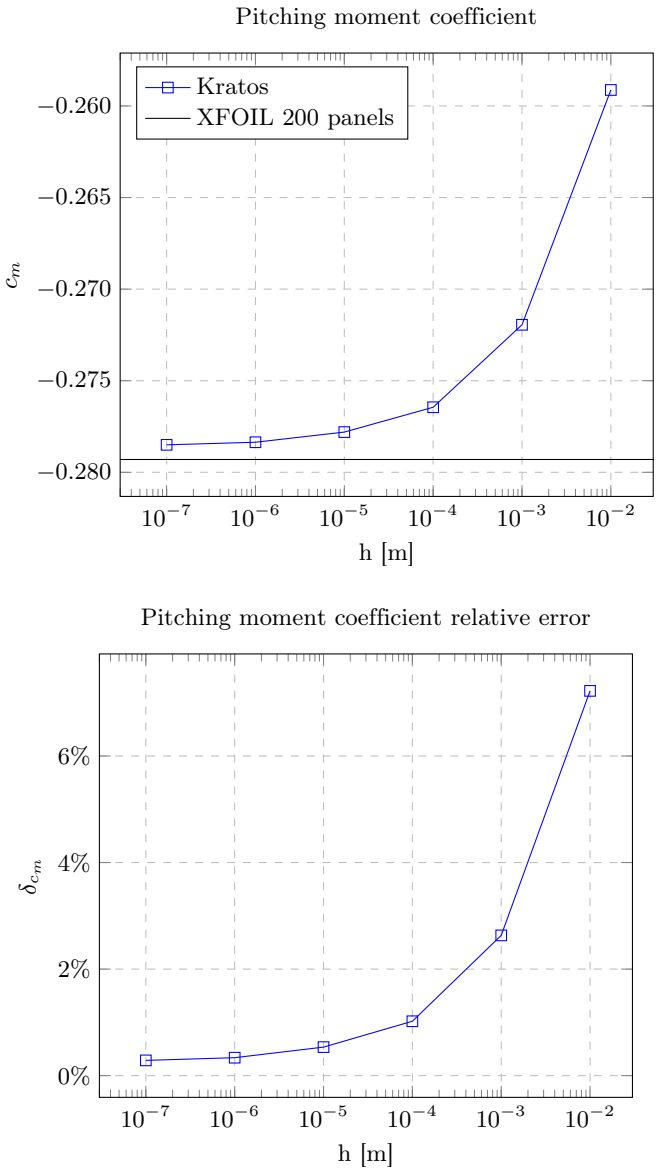

Figure C.16: NACA 0012 mesh refinement study ($\alpha = 9.0°$).

Bibliography

[1] S. Moritz. "Shape and Sizing Optimization of Aircraft Structures with Aeroelastic and Induced Drag Requirements." PhD thesis. München: Technische Universität München, 2016 (cit. on p. 1).

[2] E. Stein, R. de Borst, and T.J.R. Hughes, eds. *Encyclopedia of Computational Mechanics*. John Wiley & Sons, Ltd, Aug. 2004. DOI: 10.1002/0470091355 (cit. on p. 4).

[3] E. Stein, R. de Borst, and T.J.R. Hughes, eds. *Encyclopedia of Computational Mechanics Second Edition*. John Wiley & Sons, Ltd, Aug. 2017. DOI: 10.1002/9781119176817 (cit. on p. 4).

[4] T.L. Holst. "Transonic flow computations using nonlinear potential methods." In: *Progress in Aerospace Sciences* 36.1 (2000), pp. 1–61. DOI: https://doi.org/10.1016/S0376-0421(99)00010-X (cit. on p. 4).

[5] W.H. Mason. *Lecture notes in Configuration Aerodynamics*. http://www.dept.aoe.vt.edu/~mason/Mason_f/ConfigAeroTransonics.pdf. Virginia Polytechnic Institute and State University. 2006 (cit. on p. 4).

[6] E.M. Murman and J.D. Cole. "Calculation of plane steady transonic flows." In: *AIAA Journal* 9.1 (1971), pp. 114–121. DOI: 10.2514/3.6131 (cit. on p. 4).

[7] A. Jameson. "Iterative solution of transonic flows over airfoils and wings, including flows at mach 1." In: *Communications on Pure and Applied Mathematics* 27.3 (1974), pp. 283–309. DOI: https://doi.org/10.1002/cpa.3160270302 (cit. on p. 4).

[8] A. Jameson and D. Caughey. "A finite volume method for transonic potential flow calculations." In: *3rd Computational Fluid Dynamics Conference*. American Institute of Aeronautics and Astronautics, 1977. DOI: 10.2514/6.1977-635 (cit. on p. 5).

[9] M. Hafez, J. South, and E. Murman. "Artificial Compressibility Methods for Numerical Solutions of Transonic Full Potential Equation." In: *AIAA Journal* 17.8 (1979), pp. 838–844. DOI: 10.2514/3.61235 (cit. on pp. 5, 33).

[10] A. Eberle. *Eine Methode finiter Elemente zur Berechnung der transsonischen Potential-Strömung um Profile*. Tech. rep. Messerschmidt-Boelkow G.m.b.H. Munich (West Germany), Report No. MBB-UFE-1352-0 23 Sept. 1977, pp 1-63 (cit. on p. 5).

[11] E.H. Atta. "Component-adaptive grid interfacing." In: *19th Aerospace Sciences Meeting*. American Institute of Aeronautics and Astronautics, Jan. 1981. DOI: 10.2514/6.1981-382 (cit. on p. 6).

[12] T.H. Lê. "Transonic potential flow calculation about complex bodies by a technique of overlapping subdomains." In: *Eighth International Conference on Numerical Methods in Fluid Dynamics*. Springer Berlin Heidelberg, 1982, pp. 308–314. DOI: 10.1007/3-540-11948-5_36 (cit. on p. 6).

[13] E.H. Atta and J. Vadyak. "A grid overlapping scheme for flowfield computations about multicomponent configurations." In: *AIAA Journal* 21.9 (Sept. 1983), pp. 1271–1277. DOI: 10.2514/3.8239 (cit. on p. 6).

[14] T.L. Holst. "A chimera donor cell search algorithm suitable for solving the full potential equation." In: *15th Applied Aerodynamics Conference*. American Institute of Aeronautics and Astronautics, June 1997. DOI: 10.2514/6.1997-2259 (cit. on p. 6).

[15] T.L. Holst. "Multizone Chimera Algorithm for Solving the Full-Potential Equation." In: *Journal of Aircraft* 35.3 (1998), pp. 412–421. DOI: 10.2514/2.2339 (cit. on p. 6).

[16] T.L. Holst. "Fast transonic aerodynamic analysis suitable for the preliminary design environment." In: *17th Applied Aerodynamics Conference*. American Institute of Aeronautics and Astronautics, June 1999. DOI: 10.2514/6.1999-3133 (cit. on p. 6).

[17] A.K. Bangalore, M.A. Moulton, and F.X. Caradonna. *The development of an overset/hybrid method for rotorcraft applications*. Tech. rep. AHS Technical Special Meeting for Rotorcraft Aeronautics and Aeroacoustics, Williamsburg, VA, 1997 (cit. on p. 6).

[18] M.A. Moulton, J.O. Bridgeman, and F. Caradonna. "Development of an overset/hybrid CFD method for the prediction of hovering performance." In: *53th AHS Annual Forum, Virgina Beach, VA*. American Helicopter Society, 1997 (cit. on p. 6).

[19] A. Ecer and J. Spyropoulos. "Block-structured solution scheme for analyzing three-dimensional transonic potential flows." In: *24th Aerospace Sciences Meeting*. American Institute of Aeronautics and Astronautics, Jan. 1986. DOI: 10.2514/6.1986-510 (cit. on p. 7).

[20] B. Epstein, A. L. Luntz, and A. Nachshon. "Multigrid transonic computations about arbitrary aircraft configurations." In: *Journal of Aircraft* 26.8 (1989), pp. 751–759. DOI: 10.2514/3.45835 (cit. on p. 7).

[21] L.N. Sankar, B.K. Bharadvaj, and F.L. Tsung. "Three-dimensional Navier-Stokes/full-potential coupled analysis for viscous transonic flow." In: *AIAA Journal* 31.10 (Oct. 1993), pp. 1857–1862. DOI: 10.2514/3.11859 (cit. on p. 7).

[22] M.E. Berkman, L.N. Sankar, C.R. Berezin, and M.S. Torok. "Navier-Stokes/Full Potential/Free-Wake Method for Rotor Flows." In: *Journal of Aircraft* 34.5 (Sept. 1997), pp. 635–640. DOI: 10.2514/2.2240 (cit. on p. 7).

[23] B. Nishida and M. Drela. "Fully simultaneous coupling for three-dimensional viscous/inviscid flows." In: *13th Applied Aerodynamics Conference*. American Institute of Aeronautics and Astronautics, 1997. DOI: 10.2514/6.1995-1806 (cit. on pp. 7, 33, 36, 37, 62, 135).

[24] P. Rubbert, J. Bussoletti, F. Johnson, K. Sidwell, W. S. Rowe, S. Samant, G. Sengupta, W. Weatherill, Richard H. Burkhart, and A. Woo. "A new approach to the solution of boundary value problems involving complex configurations." In: 1986 (cit. on p. 7).

[25] D.P. Young, R.G. Melvin, M.B. Bieterman, F.T. Johnson, S.S. Samant, and J.E. Bussoletti. "A locally refined rectangular grid finite element method: Application to computational fluid dynamics and computational physics." In: *Journal of Computational Physics* 92.1 (Jan. 1991), pp. 1–66. DOI: 10.1016/0021-9991(91)90291-r (cit. on p. 7).

[26] M.B. Bieterman, J.E. Bussoletti, C.L. Hilmes, F.T. Johnson, R.G. Melvin, and D.P. Young. "An adaptive grid method for analysis of 3D aircraft configurations." In: *Computer Methods in Applied Mechanics and Engineering* 101.1-3 (Dec. 1992), pp. 225–249. DOI: 10.1016/0045-7825(92)90024-e (cit. on p. 7).

[27] A. Cenko and A. Piranian. "Potential flow applications to the prediction of the F-18E aircraft flowfield." In: *12th Applied Aerodynamics Conference*. American Institute of Aeronautics and Astronautics, June 1994. DOI: 10.2514/6.1994-1842 (cit. on p. 7).

[28] S. Ridlon, C. Hilmes, A. Dusto, R. Melvin, F. Johnson, and D. Young. *Directly coupled aeroelastic analysis capability applied to wind tunnel models.* Tech. rep. The Boeing Company, SSGTECH-97-028, 1997 (cit. on p. 7).

[29] G. SenGupta, C. Borland, F. Johnson, J. Bussoletti, R. Melvin, D. Young, M. Bieterman, and P. Palotas. "Analysis of unsteady aerodynamic and flutter characteristics of an aeroelastic model in transonic flow." In: *AGARD Special Meeting on Tran. Unsteady Aero. and Aeroelas., San Diego, CA*. 1991 (cit. on p. 7).

[30] M.D. Madson. "Transonic analysis of the F-16A with under-wing fuel tanks - An application of the TranAir full-potential code." In: *19th AIAA, Fluid Dynamics, Plasma Dynamics, and Lasers Conference*. American Institute of Aeronautics and Astronautics, June 1987. DOI: 10.2514/6.1987-1198 (cit. on p. 7).

[31] A. Goodsell, M.D. Madson, and J. Melton. "TranAir and Euler computations of a generic fighter including comparisons with experimental data." In: *27th Aerospace Sciences Meeting*. American Institute of Aeronautics and Astronautics, Jan. 1989. DOI: 10.2514/6.1989-263 (cit. on p. 7).

[32] A.W. Chen, M.M. Curtin, R.B. Carlson, and E.N. Tinoco. "TRANAIR applications to engine/airframe integration." In: *Journal of Aircraft* 27.8 (Aug. 1990), pp. 716–721. DOI: 10.2514/3.25345 (cit. on p. 7).

[33] M.D. Madson. "Sonic boom predictions using a solution-adaptive full-potential code." In: *Journal of Aircraft* 31.1 (Jan. 1994), pp. 57–63. DOI: 10.2514/3.46455 (cit. on p. 7).

[34] W. Jou, W. Huffman, D. Young, R. Melvin, M. Bieterman, C. Hilmes, and F. Johnson. "Practical considerations in aerodynamic design optimization." In: *12th Computational Fluid Dynamics Conference*. American Institute of Aeronautics and Astronautics, June 1995. DOI: 10.2514/6.1995-1730 (cit. on p. 7).

[35] A Ecer and HU Akay. "Application of finite element method for the solution of transonic flow." In: *International Symposium on Finite Element Methods in Flow Problems, 2 nd, Santa Margherita Ligure, Italy*. 1976, pp. 191–201 (cit. on p. 7).

[36] R. Glowinski, J. Periaux, and O. Pironneau. "Transonic flow simulation by the finite-element method via optimal control." In: *Finite Elements in Fluis* 3 (1976), pp. 249–259 (cit. on p. 7).

[37] H. Deconinck and C. Hirsch. "Finite Element Methods for Transonic Blade-to-Blade Calculation in Turbomachines." In: *Journal of Engineering for Power* 103.4 (Oct. 1981), pp. 665–677. DOI: 10.1115/1.3230789 (cit. on p. 7).

[38] H. Deconinck and C. Hirsch. "A multigrid method for the transonic full potential equation discretized with finite elements on an arbitrary body fitted mesh." In: *Journal of Computational Physics* 48.3 (Dec. 1982), pp. 344–365. DOI: 10.1016/0021-9991(82)90056-0 (cit. on p. 7).

[39] H.U. Akay and A. Ecer. "Transonic Flow Computations in Cascades Using Finite Element Method." In: *Journal of Engineering for Power* 103.4 (Oct. 1981), pp. 657–664. DOI: 10.1115/1.3230788 (cit. on p. 7).

[40] D. Eller. "Fast, Unstructured-Mesh Finite-Element Method for Nonlinear Subsonic Flow." In: *Journal of Aircraft* 49.5 (2012), pp. 1471–1479. DOI: 10.2514/1.c031738 (cit. on pp. 7, 36, 37, 46).

[41] I. López, E. Jones, M. Nuñez, R. Zorrilla, R. Rossi, K. Bletzinger, and R. Wüchner. "A transonic potential solver with an embedded wake approach using multivalued finite elements." In: *9th edition of the International Conference on Computational Methods for Coupled Problems in Science and Engineering (COUPLED PROBLEMS 2021)* (Chia Laguna (online conference)). Ed. by A. Larese. Vol. IS06 Advances in Unfitted Mesh Methods for the Resolution of Computational Fluid Dynamics and Fluid-Structure Interaction Problems. CIMNE, July 2021. DOI: 10.23967/coupled.2021.007 (cit. on p. 9).

[42] I. López, M. Nuñez, A. Geiser, R. Rossi, R. Wüchner, and K. Bletzinger. "A finite-element transonic potential solver with an embedded wake approach for aircraft aeroelastic optimization." In: *AeroBest 2021, International Conference on Multidisciplinary Design Optimization of Aerospace Systems* (Lisbon, Portugal (online conference)). Ed. by A.C. Marta and A. Suleman. Instituto Superior Técnico, Universidade de Lisboa, Portugal: IDMEC, July 2021, pp. 708–722. ISBN: 978-989-99424-8-6 URL https://aerobest2021.idmec.tecnico.ulisboa.pt/wp-content/uploads/2021/10/AeroBest2021_proceedings.pdf (cit. on p. 9).

[43] I. López, R. Rossi, P. Dadvand, K. Bletzinger, and R. Wüchner. "A cut finite-element method for compressible subsonic flow with an embedded wake approach for coupled aeroelastic optimization of flexible wing structures." In: *8th edition of the International Conference on Computational Methods for Coupled Problems in Science and Engineering (COUPLED PROBLEMS 2019)* (Sitges, Barcelona, Spain). CIMNE, June 2019 (cit. on p. 9).

[44] M. Davari, R. Rossi, P. Dadvand, I. López, and R. Wüchner. "A cut finite element method for the solution of the full-potential equation with an embedded wake." In: *Computational Mechanics* 63.8 (2019), pp. 821–833. DOI: 10.1007/s00466-018-1624-3 (cit. on pp. 9, 42).

[45] G. K. Batchelor. *An Introduction to Fluid Dynamics*. Cambridge University Press, Feb. 1967. DOI: 10.1017/cbo9780511800955 (cit. on p. 15).

[46] T.L. Holst. *Numerical Computation of Transonic Flow Governed by the Full-Potential Equation*. Tech. rep. NASA TM 84310, 1983 (cit. on p. 20).

[47] J. Katz and A. Plotkin. *Low-Speed Aerodynamics*. Cambridge Aerospace Series, 1991 (cit. on pp. 22, 58).

[48] M. Drela. *Flight Vehicle Aerodynamics*. Cambridge, Massachusetts: The MIT Press, 2014. ISBN: 978-0-262-52644-9 (cit. on pp. 24, 26, 62).

[49] J. Délery. *Handbook of Compressible Aerodynamics*. 111 River Street, Hoboken, NJ 07030, USA: Wiley, 2010. ISBN: 978-1-848-21141-4 (cit. on p. 36).

[50] V. Mataix. "Innovative mathematical and numerical models for studying the deformation of shells during industrial forming processes with the Finite Element Method." PhD thesis. Universitat Politècnica de Catalunya, 2020 (cit. on pp. 40, 134).

[51] P. Dadvand, R. Rossi, and E. Oñate. "An Object-oriented Environment for Developing Finite Element Codes for Multi-disciplinary Applications." In: *Archives of Computational Methods in Engineering* 17.3 (July 2010), pp. 253–297. DOI: 10.1007/s11831-010-9045-2 (cit. on pp. 43, 44).

[52] *KRATOS Multi-Physics*. https://github.com/KratosMultiphysics (cit. on p. 43).

[53] P. Dadvand and E. Oñate. "A Framework for Developing Finite Element Codes for Multi-Disciplinary Applications." URL https://www.scipedia.com/public/Dadvand_Onate_2019a. PhD thesis. Universitat Politècnica de Catalunya, CIMNE, 2008 (cit. on pp. 43, 44).

[54] C. Caremoli and A. Ribes. "Salome platform component model for numerical simulation." In: *2013 IEEE 37th Annual Computer Software and Applications Conference*. Vol. 2. Los Alamitos, CA, USA: IEEE Computer Society, 2007, pp. 553–564. DOI: 10.1109/COMPSAC.2007.185 (cit. on p. 48).

[55] J. Schoeberl. "NETGEN An advancing front 2D/3D-mesh generator based on abstract rules." In: *Computing and Visualization in Science* 1 (July 1997), pp. 41–52. DOI: 10.1007/s007910050004 (cit. on p. 48).

[56] P. Bucher. *KratosSalomePlugin*. https://github.com/KratosMultiphysics/KratosSalomePlugin. 2020 (cit. on p. 48).

[57] M. Drela. "XFOIL: An Analysis and Design System for Low Reynolds Number Airfoils." In: *Low Reynolds Number Aerodynamics*. Ed. by Thomas J. Mueller. Berlin, Heidelberg: Springer Berlin Heidelberg, 1989, pp. 1–12 (cit. on p. 48).

[58] S. Nadarajah. "Adjoint-Based Aerodynamic Optimization of Benchmark Problems." In: *53rd AIAA Aerospace Sciences Meeting*. DOI: 10.2514/6.2015-1948. eprint: https://arc.aiaa.org/doi/pdf/10.2514/6.2015-1948 (cit. on p. 48).

[59] I. H. Abbott and A. E. von Doenhoff. *Theory of Wing Sections*. Duber Publications, New York, 1959 (cit. on p. 59).

[60] N. Gregory and C. L. O'Reilly. *Low-Speed Aerodynamic Characteristics of NACA 0012 Aerofoil Sections, including the Effects of Upper-Surface Roughness Simulation Hoar Frost*. Tech. rep. NASA R&M 3726, 1970 (cit. on p. 59).

[61] C. L. Ladson. *Pressure Distributions from High Reynolds Number Transonic Tests of an NACA 0012 Airfoil in the Langley 0.3-Meter Transonic Cryogenic Tunnel*. Tech. rep. NASA TM 100526, 1987 (cit. on p. 59).

[62] B. Nishida and M. Drela. "Fully simultaneous coupling of the full potential equation and the integral boundary layer equations in three dimensions." PhD thesis. Massachusetts Institute of Technology, 1996 (cit. on p. 62).

[63] R. C. Lock. *Test Cases for Numerical Methods in Two-Dimensional Transonic Flows*. Tech. rep. AGARD REPORT No. 575., 1970 (cit. on p. 63).

[64] C. C. L. Sells. *Plane subcritical flow past a lifting airfoil*. Tech. rep. R.A.E. Tech. Rep. 67146., 1967 (cit. on p. 63).

[65] G. Volpe and A. Jameson. "Transonic potential flow calculations by two artificial density methods." In: *AIAA Journal* 26.4 (1988), pp. 425–429. DOI: 10.2514/3.9910 (cit. on pp. 72, 78).

[66] J. D. Anderson. "Fundamentals of aerodynamics." In: (1984). DOI: 10.2514/152157 (cit. on pp. 76, 82).

[67] Richard Whitcomb. *Review of NASA Supercritical Airfoils*. Tech. rep. ICAS Paper 74-10, 1974 (cit. on p. 77).

[68] W. H. Mason. *Transonic Aerodynamics of Airfoils and Wings*. Tech. rep. 2000 (cit. on p. 78).

[69] *XFLR5*. http://www.xflr5.tech/xflr5.htm. Accessed: 2021-03-30 (cit. on p. 88).

[70] V. Schmitt and F. Charpin. *Pressure Distributions on the ONERA-M6-Wing at Transonic Mach Numbers, Experimental Data Base for Computer Program Assessment*. Tech. rep. Report of the Fluid Dynamics Panel Working Group 04, AGARD AR 138, 1979 (cit. on pp. 90–93).

[71] C. Rumsey. *3D ONERA M6 Wing Validation Case*. https://turbmodels.larc.nasa.gov/onerawingnumerics_val.html. Accessed: 2021-03-30. 2018 (cit. on p. 92).

[72] J. Mayeur, A. Dumont, V. Gleize, and D. Destarac. "RANS simulations on TMR 3D test cases with the Onera elsA flow solver." In: *54th AIAA Aerospace Sciences Meeting*. DOI: 10.2514/6.2016-1357. eprint: https://arc.aiaa.org/doi/pdf/10.2514/6.2016-1357 (cit. on p. 92).

[73] F. Lyu, T. Xiao, and X. Yu. "A fast and automatic full-potential finite volume solver on Cartesian grids for unconventional configurations." In: *Chinese Journal of Aeronautics* 30.3 (2017), pp. 951–963. DOI: https://doi.org/10.1016/j.cja.2017.03.001 (cit. on p. 93).

[74] B. Diskin, W.K. Anderson, M.J. Pandya, C.L. Rumsey, J. Thomas, Y. Liu, and H. Nishikawa. "Grid Convergence for Three Dimensional Benchmark Turbulent Flows." In: *2018 AIAA Aerospace Sciences Meeting*. DOI: 10.2514/6.2018-1102. eprint: https://arc.aiaa.org/doi/pdf/10.2514/6.2018-1102 (cit. on p. 93).

[75] A. Crovato et al. "Effect of Levels of Fidelity on Steady Aerodynamic and Static Aeroelastic Computations." In: *Aerospace* 7.4 (2020). DOI: 10.3390/aerospace7040042 (cit. on pp. 98–100).

[76] J. Vassberg, M. Dehaan, M. Rivers, and R. Wahls. "Development of a Common Research Model for Applied CFD Validation Studies." In: American Institute of Aeronautics and Astronautics, June 2008. DOI: 10.2514/6.2008-6919 (cit. on pp. 102, 104, 105, 116–118).

[77] J.H. Morrison. *7th AIAA CFD Drag Prediction Workshop*. https://aiaa-dpw.larc.nasa.gov/. Sponsored by the Applied Aerodynamics TC. 2021 (cit. on p. 102).

[78] M. Rivers. *NASA Common Research Model*. https://commonresearchmodel.larc.nasa.gov/. Sponsored by NASA. 2012 (cit. on p. 102).

[79] J.H. Morrison. *4th AIAA CFD Drag Prediction Workshop*. https://aiaa-dpw.larc.nasa.gov/Workshop4/workshop4.html. Sponsored by the Applied Aerodynamics TC. 2011 (cit. on pp. 102, 106).

[80] A.J. Sclafani, M.A. DeHaan, J.C. Vassberg, C.L. Rumsey, and T.H. Pulliam. "Drag Prediction for the Common Research Model Using CFL3D and OVERFLOW." In: *Journal of Aircraft* 51.4 (July 2014), pp. 1101–1117. DOI: 10.2514/1.c032571 (cit. on pp. 102, 108, 112).

[81] M. Rivers and A. Dittberner. "Experimental Investigations of the NASA Common Research Model (Invited)." In: *28th AIAA Applied Aerodynamics Conference*. American Institute of Aeronautics and Astronautics, June 2010. DOI: 10.2514/6.2010-4218 (cit. on pp. 103, 117).

[82] A. Jameson and J. Vassberg. "Computational fluid dynamics for aerodynamic design - Its current and future impact." In: American Institute of Aeronautics and Astronautics, Jan. 2001. DOI: 10.2514/6.2001-538 (cit. on p. 105).

[83] A. Melendo, A. Coll, M. Pasenau, E. Escolano, and A. Monros. *www.gidhome.com*. [Online; accessed Jun-2018]. 2018 (cit. on p. 106).

[84] B.J. Rider and E.N. Tinoco. "CFL3D Analysis of the NASA Common Research Model for the 4thDrag Prediction Workshop." In: *4th AIAA CFD Drag Prediction Workshop*. June 2009 (cit. on pp. 108, 112).

[85] M.B. Rivers, R. Rudnik, and J. Quest. "Comparison of the NASA Common Research Model European Transonic Wind Tunnel Test Data to NASA Test Data (Invited)." In: American Institute of Aeronautics and Astronautics, Jan. 2015. DOI: 10.2514/6.2015-1093 (cit. on p. 108).

[86] M. Rivers, C. Hunter, and R. Campbell. "Further Investigation of the Support System Effects and Wing Twist on the NASA Common Research Model." In: American Institute of Aeronautics and Astronautics, June 2012. DOI: 10.2514/6.2012-3209 (cit. on pp. 112, 113).

[87] J. Vassberg et al. "Summary of the Fourth AIAA CFD Drag Prediction Workshop." In: *28th AIAA Applied Aerodynamics Conference*. American Institute of Aeronautics and Astronautics, June 2010. DOI: 10.2514/6.2010-4547 (cit. on pp. 112, 113, 116).

[88] P. Bucher, A. Ghantasala, P. Dadvand, R. Wüchner, and K. Bletzinger. "Realizing CoSimulation in and with a multiphysics framework." In: CIMNE, 2021. DOI: 10.23967/coupled.2021.048 (cit. on p. 134).

[89] P. Bucher. *CoSimIO*. https://github.com/KratosMultiphysics/CoSimIO. 2021 (cit. on p. 134).

[90] P. Bucher. *Co-Simulation Application*. https://github.com/KratosMultiphysics/Kratos/tree/master/applications/CoSimulationApplication. 2021 (cit. on p. 134).

[91] I. López, J. Piquee, P. Bucher, K.-U. Bletzinger, C. Breitsamter, and R. Wüchner. "Numerical analysis of an elasto-flexible membrane blade using steady-state fluid–structure interaction simulations." In: 106 (Oct. 2021), p. 103355. DOI: 10.1016/j.jfluidstructs.2021.103355 (cit. on p. 134).

[92] J.S. Gray, J.T. Hwang, J.R.R.A. Martins, K.T. Moore, and B.A. Naylor. "OpenMDAO: an open-source framework for multidisciplinary design, analysis, and optimization." In: *Structural and Multidisciplinary Optimization* 59.4 (Mar. 2019), pp. 1075–1104. DOI: 10.1007/s00158-019-02211-z (cit. on p. 134).

[93] J.R.R.A. Martins. *OpenMDAO*. https://github.com/OpenMDAO. Aug. 2021 (cit. on p. 134).

[94] M. Núñez, I. López, J. Baiges, and R. Rossi. "An embedded approach for the solution of the full potential equation with finite elements." In: *Computer Methods in Applied Mechanics and Engineering* 388 (2022), p. 114244. DOI: 10.1016/j.cma.2021.114244 (cit. on p. 135).

[95] M. Núñez, I. López, J. Baiges, and R. Rossi. "Adjoint based airfoil shape optimization using the full-potential equation on unfitted meshes." In: *9th edition of the International Conference on Computational Methods for Coupled Problems in Science and Engineering (COUPLED PROBLEMS 2021)* (Chia Laguna (online conference)). Ed. by A. Larese. Vol. IS06 Advances in Unfitted Mesh Methods for the Resolution of Computational Fluid Dynamics and Fluid-Structure Interaction Problems. CIMNE, July 2021 (cit. on p. 135).

Bisherige Titel der Schriftenreihe

Band	Titel
1	Frank Koschnick, *Geometrische Lockingeffekte bei Finiten Elementen und ein allgemeines Konzept zu ihrer Vermeidung*, 2004.
2	Natalia Camprubi, *Design and Analysis in Shape Optimization of Shells*, 2004.
3	Bernhard Thomee, *Physikalisch nichtlineare Berechnung von Stahlfaserbetonkonstruktionen*, 2005.
4	Fernaß Daoud, *Formoptimierung von Freiformschalen - Mathematische Algorithmen und Filtertechniken*, 2005.
5	Manfred Bischoff, *Models and Finite Elements for Thin-walled Structures*, 2005.
6	Alexander Hörmann, *Ermittlung optimierter Stabwerkmodelle auf Basis des Kraftflusses als Anwendung plattformunabhängiger Prozesskopplung*, 2006.
7	Roland Wüchner, *Mechanik und Numerik der Formfindung und Fluid-Struktur-Interaktion von Membrantragwerken*, 2006.
8	Florian Jurecka, *Robust Design Optimization Based on Metamodeling Techniques*, 2007.
9	Johannes Linhard, *Numerisch-mechanische Betrachtung des Entwurfsprozesses von Membrantragwerken*, 2009.
10	Alexander Kupzok, *Modeling the Interaction of Wind and Membrane Structures by Numerical Simulation*, 2009.
11	Bin Yang, *Modified Particle Swarm Optimizers and their Application to Robust Design and Structural Optimization*, 2009.

Band Titel

12 Michael Fleischer, *Absicherung der virtuellen Prozesskette für Folgeoperationen in der Umformtechnik*, 2009.

13 Amphon Jrusjrungkiat, *Nonlinear Analysis of Pneumatic Membranes - From Subgrid to Interface*, 2009.

14 Alexander Michalski, *Simulation leichter Flächentragwerke in einer numerisch generierten atmosphärischen Grenzschicht*, 2010.

15 Matthias Firl, *Optimal Shape Design of Shell Structures*, 2010.

16 Thomas Gallinger, *Effiziente Algorithmen zur partitionierten Lösung stark gekoppelter Probleme der Fluid-Struktur-Wechselwirkung*, 2011.

17 Josef Kiendl, *Isogeometric Analysis and Shape Optimal Design of Shell Structures*, 2011.

18 Joseph Jordan, *Effiziente Simulation großer Mauerwerksstrukturen mit diskreten Rissmodellen*, 2011.

19 Albrecht von Boetticher, *Flexible Hangmurenbarrieren: Eine numerische Modellierung des Tragwerks, der Hangmure und der Fluid-Struktur-Interaktion*, 2012.

20 Robert Schmidt, *Trimming, Mapping, and Optimization in Isogeometric Analysis of Shell Structures*, 2013.

21 Michael Fischer, *Finite Element Based Simulation, Design and Control of Piezoelectric and Lightweight Smart Structures*, 2013.

22 Falko Hartmut Dieringer, *Numerical Methods for the Design and Analysis for Tensile Structures*, 2014.

23 Rupert Fisch, *Code Verification of Partitioned FSI Environments for Lightweight Structures*, 2014.

24 Stefan Sicklinger, *Stabilized Co-Simulation of Coupled Problems Including Fields and Signals*, 2014.

Band **Titel**

25 Madjid Hojjat, *Node-based parametrization for shape optimal design*, 2015.

26 Ute Israel, *Optimierung in der Fluid-Struktur-Interaktion - Sensitivitätsanalyse für die Formoptimierung auf Grundlage des partitionierten Verfahrens*, 2015.

27 Electra Stavropoulou, *Sensitivity analysis and regularization for shape optimization of coupled problems*, 2015.

28 Daniel Markus, *Numerical and Experimental Modeling for Shape Optimization of Offshore Structures*, 2015.

29 Pablo Suárez, *Design Process for the Shape Optimization of Pressurized Bulkheads as Components of Aircraft Structures*, 2015.

30 Armin Widhammer, *Variation of Reference Strategy - Generation of Optimized Cutting Patterns for Textile Fabrics*, 2015.

31 Helmut Masching, *Parameter Free Optimization of Shape Adaptive Shell Structures*, 2016.

32 Hao Zhang, *A General Approach for Solving Inverse Problems in Geophysical Systems by Applying Finite Element Method and Metamodel Techniques*, 2016.

33 Tianyang Wang, *Development of Co-Simulation Environment and Mapping Algorithms*, 2016.

34 Michael Breitenberger, *CAD-integrated Design and Analysis of Shell Structures*, 2016.

35 Önay Can, *Functional Adaptation with Hyperkinematics using Natural Element Method: Application for Articular Cartilage*, 2016.

36 Benedikt Philipp, *Methodological Treatment of Non-linear Structural Behavior in the Design, Analysis and Verification of Lightweight Structures*, 2017.

37 Michael Andre, *Aeroelastic Modeling and Simulation for the Assessment of Wind Effects on a Parabolic Trough Solar Collector*, 2018.

Band	Titel
38	Andreas Apostolatos, *Isogeometric Analysis of Thin-Walled Structures on Multipatch Surfaces in Fluid-Structure Interaction*, 2018.
39	Altuğ Emiroğlu, *Multiphysics Simulation and CAD-Integrated Shape Optimization in Fluid-Structure Interaction*, 2019.
40	Mehran Saeedi, *Multi-Fidelity Aeroelastic Analysis of Flexible Membrane Wind Turbine Blades*, 2017.
41	Reza Najian Asl, *Shape Optimization and Sensitivity Analysis of Fluids, Structures, and their Interaction using Vertex Morphing Parametrization*, 2019.
42	Ahmed Abodonya, *Verification Methodology for Computational Wind Engineering Prediction of Wind Loads on Structures*, 2020.
43	Anna Maria Bauer, *CAD-integrated Isogeometric Analysis and Design of Lightweight Structures*, 2020.
44	Andreas Winterstein, *Modeling and Simulation of Wind-Structure Interaction of Slender Civil Engineering Structures Including Vibration Systems*, 2020.
45	Franz-Josef Ertl, *Vertex Morphing for Constrained Shape Optimization of Three-dimensional Solid Structures*, 2020.
46	Daniel Baumgärtner, *On the Grid-based Shape Optimization of Structures with Internal Flow and the Feedback of Shape Changes into a CAD Model*, 2020.
47	Mohamed Khalil, *Combining Physics-based models and machine learning for an Enhanced Structural Health Monitoring*, 2021.
48	Long Chen, *Gradient Descent Akin Method*, 2021.
49	Aditya Ghantasala, *Coupling Procedures for Fluid-Fluid and Fluid-Structure Interaction Problems Based on Domain Decomposition Methods*, 2021.
50	Ann-Kathrin Goldbach, *The CAD-integrated Design Cycle for Structural Membranes*, 2021.